INAUGURAL - DISSERTATION

submitted to the
Combined Faculties for Natural Sciences and Mathematics
of the Ruperto-Carlo University of
Heidelberg
for the degree of
Doctor of Natural Sciences

Put forward by:	Diplom-Geograph Moritz Langer
born in:	Schweinfurt
Oral examination:	2 December 2010

The Spatial and Temporal Variability of the Energy Balance at an Arctic Polygonal Tundra Site

Referees: Dr. Julia Boike
Prof. Dr. Lucas Menzel

Zusammenfassung

Permafrostböden bedecken bei weitem das größte Gebiet der arktischen Landoberfläche und werden von der Klimaerwärmung besonders betroffen sein. Das Auftauen der Dauerfrostböden wird häufig mit klimatischen Rückkopplungsprozesssen in Verbindung gebracht, wie dem zusätzlichem Ausstoß von Treibhausgasen und der Veränderung der hydrologischen Kreisläufe. Diese Mechanismen werden zukünftige klimatische Entwicklungen entscheidend beeinflussen und die aktuelle Klimaerwärmung weiter verstärken. Für Klimaprognosen ist es deshalb entscheidend, die momentane und die zukünftige Ausdehnung der Permafrostgebiete zu erfassen und die klimarelevanten Prozesse zu verstehen. Dazu müssen verlässliche Monitoringprogramme und Modelle entwickelt werden, die den Zustand der Permafrostböden charakterisieren können. Untersuchungen der Energiebilanz der Landoberfläche sind ein wichtiger Beitrag für die Entwicklung von Klimamodellen. Nur so können die Austauschprozesse in der atmosphärischen Grenzschicht verstanden werden, welche in den Klimamodellen abgebildet werden.

Die vorliegende Arbeit untersucht anhand von einer Reihe intensiver Messkampagnen die Energiebilanzen der Oberfläche von polygonaler Tundra im Lena-Delta im Nordosten Sibiriens. Die Energiebilanz wird von drei wesentlichen Faktoren gesteuert: der Schneedecke, der Wolkenbedeckung und des Bodenwärmehaushalts. Die Schneedecke und die Wolkenbedeckung beeinflussen im Wesentlichen die Strahlungsbilanz der Oberfläche. Die Schneedecke reflektiert im Frühling einen beachtlichen Teil der einfallenden kurzwelligen Strahlung. Das Gleiche gilt für eine Wolkendecke, die allerdings gleichzeitig die am Boden einfallende langwellige Thermalstrahlung erhöht. Während des polaren Winters hat insbesondere der Bodenwärmestrom einen bemerkenswert hohen Anteil an der Strahlungsbilanz. Durch das Rückfrieren der sommerlichen Auftauschicht wird ein großer Teil der gespeicherten Energie wieder frei gesetzt. Zusätzlich wird der Bodenwärmestrom von einem sehr hohen Bodentemperaturgradienten gestützt, hervorgerufen durch die extrem kontinentalen klimatischen

Bedingungen am Untersuchungsstandort.
In den Sommermonaten nehmen die fühlbaren und latenten Wärmeflüsse den größten Anteil ein. Mehr als die Hälfte der zur Verfügung stehenden Nettostrahlung geht in den latenten Wärmestrom. Temperaturunterschiede werden im Wesentlichen durch die stark strukturierte Geländeoberfläche bestimmt. Innerhalb weniger Meter finden Wechsel von trockenen und feuchten Bereichen statt, die Temperaturdifferenzen zwischen 5 und 10 Kelvin aufweisen können. Diese Unterschiede in der Oberflächentemperatur verschwinden allerdings, sobald die Durchschnittstemperaturen über Zeiträume länger als einen Tagesgang betrachtet werden. Dieses Ergebnis stellt eine wertvolle Erkenntniss für Permafrostmonitoring dar, welches auf Fernerkundungsdaten zur Abschätzung der Oberflächentemperatur zurückgreift. Da in der Tundra im Sommer über längere Mittlungszeiträume nur geringe Temperaturunterschiede auftreten, sinken die Anforderungen an die räumliche Auflösung satellitenbasierter Temperaturmessungen. Die Studie unterstreicht daher das Potential von Fernerkennungsdaten zur Erforschung und Überwachung des Permafrostzustands.

Abstract

Permafrost soils, which occupy by far the largest fraction of the arctic land area, are expected to be substantially affected by climate warming. The degradation of permafrost is potentially associated with climate feedback mechanisms such as greenhouse emissions and changes in the hydrological cycle, which could magnify future climate warming. The determination of the recent and future permafrost distribution and its thermal condition is therefore an essential issue for the prediction of future climate change. This requires the development of reliable monitoring and modeling schemes, which allow both the future predictions and the validation of the permafrost conditions.

Studies of the surface energy balance can significantly contribute to the development of modeling schemes, since they directly measure the processes at the ground-atmosphere interface as they are represented in climate models. This thesis investigates the surface energy balance in a polygonal tundra landscape of the Lena River Delta, Siberia, in a series of extensive field measurements. The controlling factors of the surface energy balance are in particular the snow cover, the presence of a cloud cover and the ground thermal regime. The first two factors mainly influence the radiation budget by reflecting the largest part of the incoming short-wave radiation in spring, and by increasing the incoming long-wave radiation, respectively. The ground heat flux is found to be of remarkable importance for the surface energy balance, especially during the polar winter, when the refreezing active layer provides a strong supply of energy. In addition, the large annual temperature amplitude at the study site contributes to the strong ground heat fluxes. Turbulent heat fluxes are of great importance particularly during summer, when latent heat fluxes consume about half of the net radiation. However, spatially distributed measurements of the turbulent heat fluxes suggest distinctly different surface energy balances over scales of ten meters due to the regular pattern of dry and wet areas of the polygonal tundra. This is also confirmed by spatially resolved measurements of the surface temperature with a thermal imaging system

during the summer season. Due to different partitioning of energy at dry and wet surfaces remarkable temperature differences on the order of 5 to 10 K can occur. These spatial differences in the surface temperature are found to vanish in temporal averages longer than the diurnal cycle. While this suggests that the summer radiation budget of dry and wet areas is not too different, it also has important implications for permafrost monitoring schemes based on remotely sensed land surface temperatures. The diminished surface temperature variability for temporal averages reduces the requirements on the spatial resolution of satellite-based surface temperature products. The study is a clear indication of the potential of satellite-based monitoring of permafrost landscapes.

Contents

List of Tables

List of Figures

Chapter 1

Background and Outline of the Thesis

1.1 Introduction

Permafrost is defined as soil or rock that feature temperatures continuously below the freezing point for at least two consecutive years (Harris et al. 1988). Thus, permafrost is associated with specific climate conditions typically occurring in the Arctic or in high mountain regions. About 25% of the landmass of northern Hemisphere is occupied by permafrost, most of which is located in Siberia and on the North-American continent (Canada, Alaska) (Brown et al. 1997, Zhang et al. 2008). A commonly used classification of permafrost distinguishes four zones based on the fraction of the surface that is underlain by permafrost (Fig. 1.1). The largest part of the permafrost area is in the zone of continuous permafrost, where at least to 90% of the area is underlain by permanently frozen ground. The zones of discontinuous (50 to 90% fraction of permafrost area), sporadic (10 to 50% fraction of permafrost area) and isolated (occasional patches) permafrost correspond to the gradual transition from a periglacial to a non-periglacial landscape. The current permafrost distribution results from both current and past climate conditions. The geological past of some existing permafrost structures reaches back into the Pleistocene, about 1.5 million years ago (Velichko and Nechayev 1984, Astakhov et al. 1996). Such ancient permafrost is typically found in the zone of continuous permafrost and can reach depths of up to 1.5 km (French 2007). However, most permafrost occurrences feature depths of less than 400 m (French 2007). Due to the thermal inertia of the ground, which can be significantly amplified by an isolating organic soil layer or a vegetation cover, permafrost is often found to be in disequilibrium with recent climate conditions (Yershov and Williams 2004). This is especially true during periods of fast climatic changes (Fig. 1.2).

There is convincing evidence from both observations and modeling that the Arctic has experienced a significant warming in the last decades (e.g. Overpeck et al. 1997, Comiso 2003, Hinzman et al. 2005, Tape et al. 2006, Turner et al. 2007, Overland et al. 2008), which can be attributed to sustained changes in the global atmospheric circulation pattern affecting the arctic climate system (Thompson and Wallace 1998, Fyfe et al. 1999, Moritz et al. 2002). This warming trend is also reflected in the thermal conditions of the permafrost. Over the past decades, a warming of permafrost temperatures has been reported

Figure 1.1: The permafrost distribution in the Arctic classified according to its spatial occurrence (UNEP/GRID-Arendal 2005b).

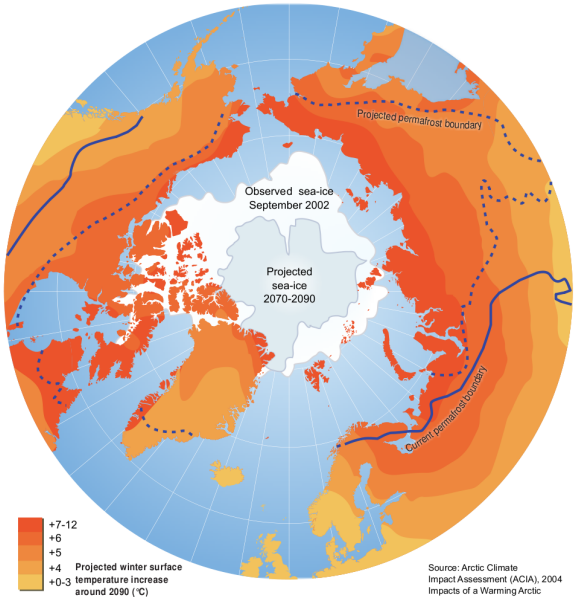

Figure 1.2: The impact of climate change on the Arctic. The map shows the projected near surface air temperature according to the Arctic Climate Impact Assessment (ACIA) (UNEP/GRID-Arendal 2005a).

in the entire Arctic (Osterkamp 2005, Brown and Romanovsky 2008). The magnitude of the warming strongly varies according to the local conditions, but is generally in the range of 0.5 to 2.0 °C a^{-1} at the depth of zero annual amplitude. The most pronounced effect on permafrost is observed during spring and the long-lasting arctic winter season, which is mainly related to changes in precipitation (snow fall) and cloud cover (Serreze et al. 2000, Hinzman et al. 2005; 2006). The warming trend is predicted to continue and even accelerate in the future by General Circulation Models (GCM's). The warming rate in the Arctic is expected to be by a factor of two to three larger than the global average, with a projected increase of the average near-surface air temperature of about 10 °C within the next 100 years. This accelerated warming is related to strong positive climate feedback mechanisms, induced by the shrinking sea-ice cover and increased wintertime cloudiness (e.g. Holland and Bitz 2003, Kaplan et al. 2003, Vavrus 2004).

Permafrost has received much attention as a potential source of a positive feedback mechanism on the climate, as large amounts of carbon are stored in permafrost soils (Christensen and Cox 1995, Callaghan et al. 2004). Until now, it is unclear whether permafrost regions will turn into massive sources of greenhouse gases, such as methane and carbon dioxide, when the frozen soils begin to thaw (Hobbie et al. 2000, Davidson and Janssens 2006). The transformation of permafrost soils from net carbon sinks to sources depends on the amount of carbon that is made available for microbial decomposition. Zimov et al. (2006) estimated that about 970 Gt of carbon are stored in permafrost soils, mostly in wet tundra landscapes of Siberia, northern Canada and Alaska, which is about twice the amount of carbon currently contained in the atmosphere (Schuur et al. 2008). To realistically assess the emission potential of greenhouse gases of these regions, it is crucial to know how the thermal state of the permafrost will change under a warming climate. In particular, this concerns the evolution of the annual thaw depth and the active layer thickness, as they determine the timespan, during which the uppermost soil layers remain unfrozen. Moreover, increasing active layer depths are considered to lower the stability of permafrost soils towards erosion, which in turn could lead to the expansion of thaw lakes and ponds (Hinkel et al. 2003). The expansion of lakes is associated with the reallocation of organic soil material into the water body, where the conditions are favorable for anaerobic decomposition. Walter et al. (2006) demonstrated that permafrost degradation and thaw (thermokarst)-lake expansion has an effect on the atmospheric methane budget. These processes do not require permafrost to vanish completely, but only a change in the annual freeze and thaw dynamics and thus of the heat budget of the uppermost soil layers. These can react on short timescales to external forcing, such as rising air temperatures, compared to the entire permafrost body. Further climate feedback mechanisms associated with permafrost degradation might be induced by changes in the vegetation cover, such as shrub expansion and the northward shift of the tree line (McGuire et al. 2006). Such prominent changes of the surface characteristics might in turn affect important parameters in the land-atmosphere interactions, such as the surface albedo, the snow cover, the thermal soil characteristics and the hydrological cycle. For many of these factors, it is yet unclear whether they will enhance or attenuate the recent warming trend in the Arctic.

It is highly desirable to gain a better understanding of permafrost processes and possible feedback mechanisms on the climate system, which could eventually facilitate to develop reliable permafrost monitoring and modeling schemes. Furthermore, it should be carefully evaluated whether the representation of permafrost processes in current climate models requires enhancement in order to improve predictions on the future climatic changes in the Arctic.

1.2 State of the art and scientific goals

The studies presented in this thesis contribute to (i) satellite-based Land Surface Temperature (LST) detection and (ii) the understanding of the processes of surface energy exchange in typical permafrost landscapes in northern Siberia. Both topics are motivated by the requirement of future permafrost monitoring and modeling schemes.

1.2.1 Permafrost monitoring

To evaluate the impact of climate change on permafrost landscapes, one must (i) determine permafrost areas that are vulnerable to climate change and (ii) evaluate the magnitude of the changes, such as the increase of active layer depths.
These key issues are addressed in the international monitoring projects 'Thermal State of Permafrost' (TSP) and the 'Circumpolar Active Layer Monitoring' (CALM) program, which have been initiated by the International Permafrost Association (IPA). Despite the fact that these programs comprise more than 120 sites for active layer observations and about 800 boreholes for temperature measurements, the largest part of the arctic permafrost areas is not covered, as it is considered to be inaccessible under reasonable effort.
Satellite-based monitoring of permafrost offers a cost-efficient alternative to cover the vast and remote arctic landscapes. However, since permafrost is a subsurface phenomenon, it is not directly detectable with remote sensing applications. Therefore, two different concepts are followed in satellite-based permafrost monitoring schemes. The first concept is based on the detection of changes of landscape elements, such as the vegetation cover or landscape structures (e.g. thaw lakes) that are associated with the occurrence of certain permafrost conditions (e.g. Leverington and Duguay 1998, Stow et al. 2004, Grosse et al. 2005, Duguay et al. 2005). A more direct scheme uses time series of satellite-derived Land Surface Temperature (LST) measurements in combination with a soil heat transfer model to calculate the evolution of subsurface temperatures. First applications of LST-based permafrost detection have been demonstrated by Hachem et al. (2008) and Marchenko et al. (2009), who use a surface temperature product provided by the Moderate Resolution Imaging Spectroradiometer (MODIS).
There are a number of satellite LST products available (e.g. ASTER, Landsat, MODIS, AVHRR, MVIRI, ATSR), which all have specific limitations concerning the spatial and temporal resolution. The resolution in space and time is a crucial factor for the suitability of a product for LST-based permafrost monitoring schemes, since the scales must be sufficiently

captured, at which variations of the surface temperature occur that are relevant for permafrost. Spatial differences of the surface temperature become relevant for the permafrost heat budget when they persist over a longer period, which then might cause differences in thaw depth and permafrost temperatures. This in turn could be an important indicator of relevant processes such as initial thermokarst erosion, which is often triggered by spatial heterogeneities (French 2007). The temporal resolution of satellite measurements could be even more critical, since adequate time series of surface temperatures are required as upper boundary condition in the heat transfer models. The required resolution essentially depends on the investigated process. The correct representation of the active layer dynamics, for example, requires a temporal resolution of several days or less, since temperature fluctuations on shorter time scales are largely damped in the soil after a few centimeters. With regard to satellite-based permafrost monitoring schemes, it should be checked whether satellite-based LST measurements can deliver adequate spatial and temporal averages, which is especially important in heterogeneous landscapes, such as the wet polygonal tundra. For this purpose, the following goals are set:

- The evaluation of the spatial and temporal variability of the summer surface temperatures of a typical wet tundra landscape by using a high resolution thermal imaging system. This involves the development of a retrieval algorithm for radiometric and geometric corrections, to infer the "true" skin surface temperature from these measurements.
- The assessment of the performance of the MODIS L2 LST product at the study site in comparison with upscaled measurements of the thermal imaging system. With this, the possibilities and limitations of MODIS LST for permafrost monitoring in the heterogeneous landscapes of the wet polygonal tundra can be clarified.

1.2.2 Permafrost modeling

Due to the potential climatic feedback mechanisms triggered by permafrost degradation (such as the release of stored organic carbon or the change of vegetation cover), efforts have been initiated to include permafrost and the annual dynamics of freezing and thawing into global climate models (e.g. Stendel and Christensen 2002, Lawrence and Slater 2005, Nicolsky et al. 2007, Lawrence et al. 2008). The interactions of land and atmosphere in GCM's are based on the surface energy balance equation, which is solved using parameterizations for typical parameters, such as the albedo, the surface roughness (roughness length), the surface resistance to evapotranspiration and the soil heat conductivity, just to mention a few. The ground heat flux determining the permafrost heat budget depends on the calculated energy partitioning at the surface and hence on the used parameterizations. However, in reality, the surface-atmosphere interactions are very complex and the thermal state of permafrost essentially depends on local soil and surface characteristics. It is therefore questionable, whether large-scale parameterizations as they are used in global climate models are applicable in heterogeneous landscapes, such as the polygonal tundra. To answer this question it is necessary to determine the crucial factors governing the permafrost processes

which must be accounted for in model schemes. This can only be evaluated by field experiments directly measuring the surface energy balance under different synoptic and seasonal conditions. Studies of the surface energy balance constitute an important tool to assign and assess the controlling factors of the land-atmosphere interactions, which can be used to develop and improve model schemes. Such studies are especially required in the Arctic, where meteorological measurements and detailed studies of the surface energy balance are very rare. The present study aims to achieve:

- A comprehensive compilation of the surface energy balance at a typical wet tundra landscape covering the entire annual cycle.
- The identification of spatial and temporal variabilities of the surface energy budget in order to obtain information about the controlling factors of the energy exchange processes, especially for the permafrost heat budget.
- The assignment of processes and factors, which must be represented in large-scale permafrost model schemes.

Furthermore, the performed energy balance study aims to evaluate the role of the ground heat flux for processes of the boundary layer of the lower atmosphere. It is known from several studies that the ground heat flux can have a distinct impact on the atmospheric conditions, such as the near-surface air temperatures and the evolution of stable atmospheric stratifications. It has been demonstrated by Viterbo et al. (1999) that stable atmospheric conditions, which are related to extreme surface cooling, are largely prevented by the release of latent heat from freezing soils. The implementation of soil freezing essentially improves the performance of weather forecast models, which otherwise deliver unrealistically stable atmospheric conditions during winter. Similar effects are reported for climate models (Cox et al. 1999). However, the parametrization of the soil characteristics in climate models is optimized for the mid-latitudes and is therefore not necessarily applicable in permafrost regions. Hence, the study of the surface energy balance aims to achieve a better understanding of (i) how the thermal state of permafrost is determined by processes above the surface and (ii) how these processes are in turn affected by the thermal conditions of the soil.

1.3 Study site

This study is performed in northeast Siberia on Samoylov Island situated in the southern part of the Lena River Delta (72° 22' N; 126° 30' E). The Lena River Delta is the largest delta in the Arctic. It covers an area of about $32,000\,\mathrm{km}^2$ and stretches about 230 km in east-west and about 150 km in north-south direction. With a catchment area of about $2,490,000\,\mathrm{km}^2$, the Lena River constitutes the main drainage channel of Siberia with a total annual discharge of about $520\,\mathrm{km}^3$ (Rachold et al. 2007). The highest stream flow through the braided network of the Delta channels is measured in June, when approximately 35% of the annual discharge is released (Yang et al. 2002). The timing of this event is closely related

to the ice run and snow melt in the Delta. According to its geological and geomorphological structure, the Lena River Delta can be divided into three main terraces. The first and the second terrace are mainly characterized by wet tundra featuring the typical polygonal surface structures. Whereas the third terrace consists of the so-called ice complex, which is a massive ground ice body overlain by a shallow organic soil layer. The first Holocene terrace and a recent floodplain basically occupy the eastern part of the River Delta. The western part of the Lena Delta has been inactive recently and consists of deposits of at least Pleistocene age, which constitute the second and third terrace (Schwamborn et al. 2002). Samoylov Island is located at the fork of the two main channels of the Lena River (Bykovskaya & Trofirmovskaya) close to the Kharaulakh Ridge, the prolongation of the Verkhoyansk Range. The island has a surface of about 4.5 km^2, of which the eastern part belongs to the first terrace and is about 10 m elevated above the water level. The western part of the island is a recent floodplain regularly flooded in June.
On Samoylov Island, a periodically manned Russian-German research station has been operated since 1998. Continuous climatological measurements have been carried out since then. The station belongs to the Lena Delta Reserve that comprises about 61,000 km^2, including the New Siberian Islands and thus being the largest nature reserve of Russia.

1.3.1 The polygonal tundra

The polygonal tundra is certainly one of the most eye-catching types of landscape in permafrost regions. It constitutes a comb-like surface with regular polygonal structures that feature elevated rims and lowered centers (Fig. 1.3). At occasional locations, the low-center structure is inverted, so that the center is elevated compared to the rims (high center polygon). The diameter of a polygon is typically 15 to 40 m and the elevation difference between center and rim ranges from 0.1 to 0.5 m. According to the most common explanation, these structures originate from thermal contraction cracking during the winter and ice-wedge growth due to subsequent water and sediment infiltration into the crack (Lachenbruch 1962; 1966). Recent studies suggest that soil cracking typically occurs when the soil temperature approaches about -15 °C or below (Allard and Kasper 1998, Fortier and Allard 2005). However, the mean soil temperature is less important for the formation of frost-cracks and hence the polygonal tundra, than is the magnitude and the duration of the soil cooling rate. Mackay (1993) showed that ice-wedge cracking favorably occurs when soil cooling rates larger than 1.8 °C d^{-1} persist for more than 4 days. Such temperature evolutions are often reached under arctic-continental climate conditions. However, a direct correlation between the occurrence of polygonal tundra and climate conditions is difficult since the frost-cracking depends on a wide range of factors, e.g. the local soil conditions (French 2007).
The micro-relief of the polygonal tundra is associated with a strong heterogeneity in surface wetness and vegetation cover, which is facilitated by shallow active layer depths and a high soil water content (French 2007, Minke et al. 2009). The water level relative to the surface essentially depends on the dynamics of the active layer and the rates of precipitation. Observations at the study site have shown that the water level during the summer period is always

Figure 1.3: Typical surface structure of the polygonal tundra landscape.

close to the surface of the polygonal centers, which are consequently saturated with water (Kutzbach et al. 2004). The elevated rims are significantly drier, which is also reflected in the vegetation cover. The lowered centers are dominated by hydrophytic peat mosses and sedges, while the elevated rims are mainly occupied by mesophytic sedges, mosses and dwarf shrubs (Kutzbach et al. 2004). Moreover, the polygonal tundra is typically characterized by frequent open water areas, ranging from small ponds to large thermokarst lakes. The water bodies at the study site range from a few to several hundred square meters in size with depths between 0.5 and 5 m.
The soils at the study site are water-saturated, featuring a high organic content with a considerable fraction of silt and fine sand. The soils can be roughly classified as *gelic gleysols* at the rims and *gelic histosols* at the centers (Mueller 2007). Due to ice-wedge growth, the soils at the rims are significantly affected by cryoturbation, whereas the peat soils at the centers are only marginally disturbed (Kutzbach et al. 2004). The maximum thaw depth ranges from 0.4 to 0.6 m and is found to be almost similar at the rims and the centers.

1.3.2 Climate and weather conditions

The climate at the study site is characterized by arctic-continental conditions featuring a strong seasonality in temperature and generally low precipitation rates (Fig. 1.4). At the Stolb-Station close to the study site, where routine measurements of meteorological variables are conducted, the mean annual air temperature (MAAT) is about $-13\,^{\circ}\mathrm{C}$ and the annual precipitation is between 200 and 300 mm (Fig. 1.4). The snow-free season lasts from June until August and the frost free period is limited to about 70 days (Laing et al. 1999). During the summer months, the air temperature frequently exceeds $20\,^{\circ}\mathrm{C}$, especially during the polar day period, which lasts from the beginning of June until mid of August. The synoptic conditions during the summer are characterized by frequent high pressure conditions, which can be disturbed by the influx of cyclones that predominately originate in the

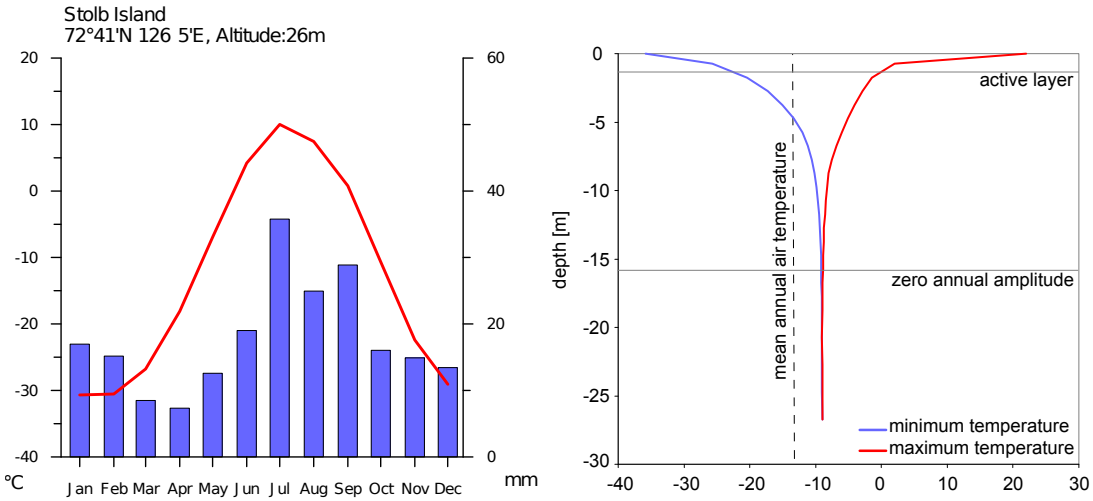

Figure 1.4: Left: Climate diagram of Stolb station (1996-2006) in the vicinity of the study site. Right: Annual minimum and maximum permafrost temperatures measured in a 26 m borehole at the study site; active layer depth and depth of zero annual amplitude are marked.

west (Zhang et al. 2004). The cyclone activity is associated with a dense cloud cover and rain. Air mass thunderstorms are observed occasionally, which can be locally very heavy featuring high wind speeds and strong rain events.
The climate conditions during winter are mainly characterized by the polar night (beginning of December until end of January) and the presence of the Siberian High, which cause the air temperature to fall frequently below −45 °C. The influence of the Siberian High affects the monthly precipitation (snow fall) rates, which are significantly reduced compared to the summer period (Fig. 1.4). However, cyclones also frequently occur during the winter period, but feature a high intensity and short life times (Zhang et al. 2004). The cyclone activity is usually associated with strong snow storms. About half of the entire annual precipitation (≈ 100 mm) occurs as snow fall from October to May (Fig. 1.4). The very low winter time temperatures are also reflected in the ground, which is characterized by very low annual average temperature of about −9.5 °C. The high annual temperature amplitude of the continental climate is also reflected in the annual soil temperature variations, which are observed at depths of about 16 m (Fig. 1.4).

1.4 Applied methods

The energy partitioning at the ground-atmosphere interface is the main driving force in the global climate system. The amount of energy that is delivered to or from the ground surface is largely determined by the earth radiation budget, which consists of a short- and a long-wave part. While the short-wave part originates from direct solar and diffuse sky radiation, the long-wave part is thermal radiation originating from the ground surface or the

atmosphere, respectively. In this thesis, all incoming radiation components, that transport energy towards the ground surface, are defined positive. The net radiation Q_{net}, which is the sum of incoming and outgoing short-and long-wave radiation, is balanced by energy fluxes in the ground and in the atmosphere. In the atmosphere, turbulent transfer of energy gives rise to the sensible heat flux Q_H and the latent heat flux Q_E. In contrast, the ground heat flux Q_G is mainly determined by conductive heat transfer. A more detailed description of all components of the energy balance is given in Chapter 3. The surface energy balance equation is therefore written as

$$Q_{\mathrm{net}} = Q_H + Q_E + Q_G. \tag{1.1}$$

During the snow melt season, the surface energy balance equation must be complemented by an additional term, that represents the energy consumed by the melting snow.
In this thesis, the results of several months of intensive field work on Samoylov Island are presented. The measurements were conducted within four expeditions in early spring 2008 and 2009 and in summer and fall 2007 and 2008. The following sections give a brief overview of the applied measurements that are used to derive the surface energy balance and related climate parameters. The measurement plot on Samoylov Island and the locations of the instrumentation are depicted in Fig. 1.5. A detailed overview of the station equipment and the employed sensors is given in Figs. 1.6 to 1.11. Ancillary field measurements are listed in Fig 1.12.

1.4.1 Thermal imaging system and the radiation balance

During the summer field campaign in 2008, a high resolution thermal camera is used for the detection of surface temperature variabilities at the polygonal tundra (Fig. 1.10). The imaging system is mounted on a 11 m tower and features a 12 mm wide-angle lens. The field of view of the measurement system comprises a 100 m^2 tundra section, featuring wet and dry surfaces elements, as well as a polygonal pond. The VARIOCAM thermal imaging system consists of an uncooled microbolometer detector with a resolution of 384 x 288 pixels. The spectral sensitivity ranges from 7.5 to 14 µm. The thermal camera delivers brightness temperatures of the tundra surface, measured under an off-nadir angle of 55°. With the measurement rate set to 10 min, a data set of more than 7000 thermograms could be generated during the observation period from the end of July until the end of September. In order to obtain spatially distributed measurements of the surface temperature, the entire dataset must be processed with a geometric and radiometric correction algorithm. A detailed description of the used procedure is given in the concerning article (Chapter 2). The radiometric corrections require measurements of the downwelling thermal sky radiation, which is measured by a four component radiation sensor in the vicinity of the thermal camera (Fig. 1.9).

Further radiation measurements are conducted in the context of the surface energy balance study. Besides the already mentioned four component sensor, additional net radiation sensors are applied. The net radiation sensors are located at the standard climate tower (Fig. 1.6) and at the Lake Station (Fig. 1.7). At the standard climate tower, the outgoing

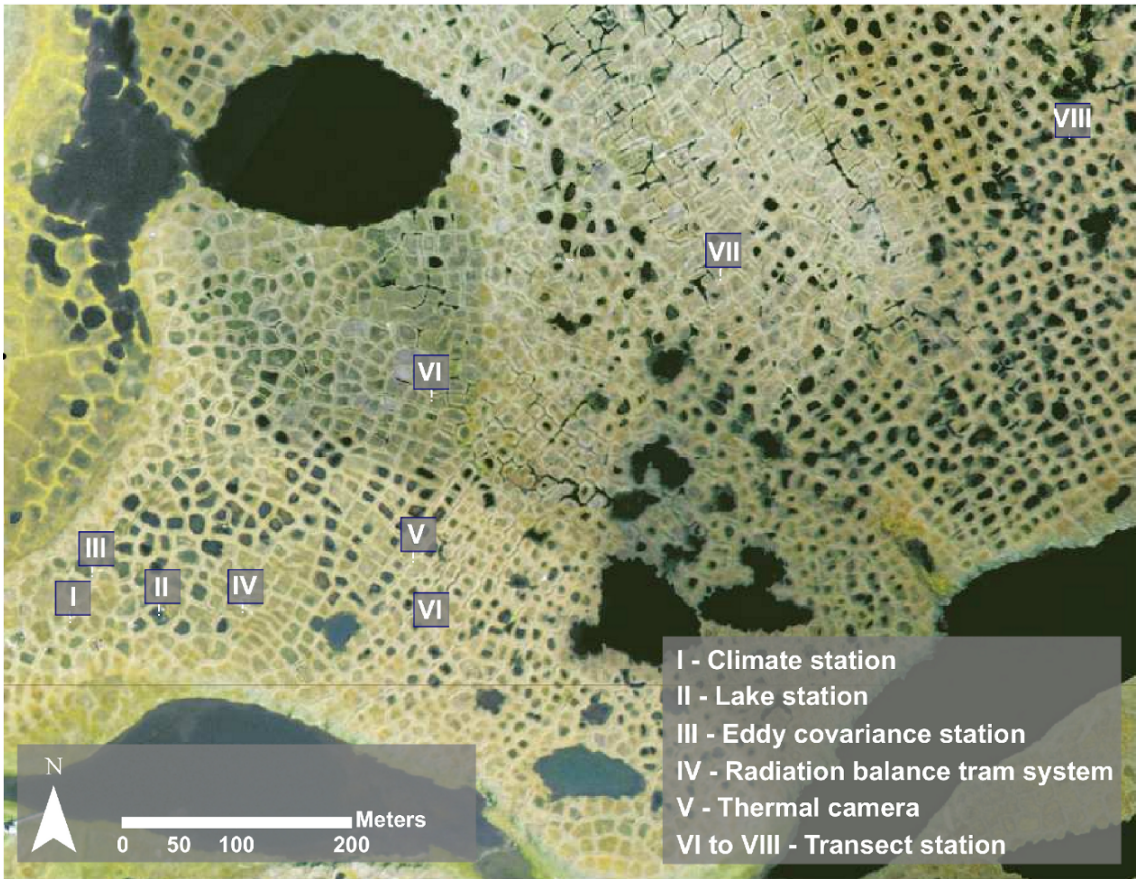

Figure 1.5: The study site and locations of the used measurement systems. The realized field experiments are based on 8 measurement location distributed along a east-west transect across Samoylov Island.

Climate station (*Station I*)

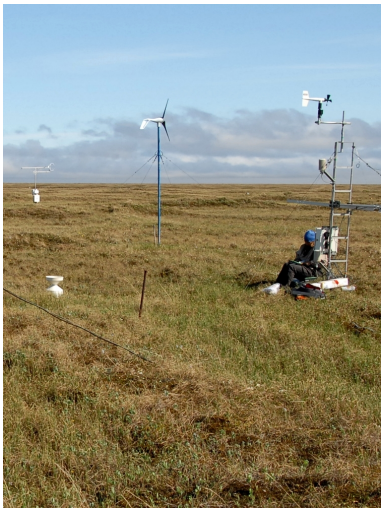

Instrument	*Manufacturer*	*Measured parameter*	*Quantity*
MP100	Rotronic	air temperature and humidity	2
Nrlite	Kipp&Zonen	net radiation	1
CG1	Kipp&Zonen	outgoing longwave radiation	1
05103-5	RM Young	wind speed and direction	1
ARG 100	RM Young	precipitation	1
SR50	Campbell Scientific	snowheight	1
CC640	Campbell Scientific	surface image	1
107-L	Campbell Scientific	soil temperature in profiles	32
CS610-L	Campbell Scientific	soil moisture in profiles	20
XR-420	RBR	soil temperature profile (27 m)	1

Figure 1.6: The climate station and the employed sensors. The system is operational since 1998 and delivers continuous meteorological and soil physical measurements.

Lake station (*Station II*)

Instrument	*Manufacturer*	*Measured parameter*	*Quantity*
Nrlite	Kipp&Zonen	net radiation	2
SR50	Campbell Scientific	water depth	1
PT100	Campbell Scientific	air/soil/water temperature in profiles	16
CS616	Campbell Scientific	soil moisture in profiles	5

Figure 1.7: Technical details of the lake station, the system was in installed in summer 2006. The small lake features a diameter of about 20 m and is about 0.8 m deep.

Eddy covariance Station
(Station III)

Instrument	*Manufacturer*	*Measured parameter*
CSAT-3	Campbell Scientific	wind speed, sonic temperature
LI-7500	LI-COR	concentration of H_2O/CO_2

Figure 1.8: The applied eddy covariance station at the field site on Samoylov Island. The system was installed in Spring 2007. A second eddy station featuring a similar setup was applied as mobile station in summer 2008.

Radiation balance tram system
(Station IV)

Instrument	*Manufacturer*	*Measured parameter*
NR01	Kipp&Zonen	4-component radiation
RPT410	Druck Limited	pressure
MP100	Rotronic	air temperature and humidity
SP1110	Skye Instruments	global radiation

Figure 1.9: The radiation balance is measured by a four component sensor. The four component sensor was operated during summer 2007 and from spring 2008 until winter 2009.

Thermal camera
(Station V)

Instrument	*Manufacturer*	*Measured parameter*
VARIOCAM HR	Infratec	spatially resolved surface temperature

Figure 1.10: The thermal imaging system mounted on the 11 m tower at the field site on Samoylov Island. The thermal imaging system was applied during the summer expedition in 2008.

long-wave radiation is continuously measured using a single-component long-wave radiation sensor (CG1, Kipp & Zonen, Netherlands). In order to obtain spatially distributed measurements of the outgoing long-wave radiation, six infrared surface temperature sensors (IRTS-P, Apogee Instruments, USA) are placed along the Transect Stations (Fig. 1.11).

1.4.2 Turbulent heat fluxes

Turbulent fluxes of sensible and latent heat are measured using an eddy covariance system (Fig. 1.8). The method is based on high-frequency measurements of wind speed, air temperature and specific humidity. Due to the high-frequency measurements, it is possible to correlate up- and downwind fluctuations to fluctuations of air temperature and humidity. As sensible and latent heat fluxes are facilitated by up- and downward moving air parcels of different size and different temperature and moisture content, the sensible and latent heat fluxes can be calculated from the covariances between the fluctuations of the vertical wind speed and the air temperature, and the vertical wind speed and the specific humidity, respectively.
The employed eddy covariance system consists of a Campbell C-SAT 3D sonic anemometer and a LiCOR LI-7500 CO_2 and H_2O open-path gas analyzer unit. The sensors are mounted on a 2.4 m mast. The data are sampled at a rate of 20 Hz using a Campbell CR3000 data logger. The gas analyzer is only operational during field campaigns due to the required system maintenance and the high power demand, which could not be guaranteed during

Transect station
(Station VI-VII)

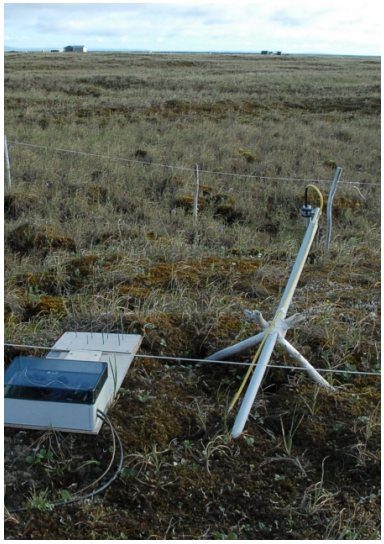

Instrument	*Manufacturer*	*Measured parameter*	*Quantity*
CS616	Campbell Scientific	soil moisture in profiles	5
Thermocouple	Omega	soil and snow temperature in profiles	20
IRTS-P	Apogee	surface temperature	2
CSAT-3 (temporarily)	Campbell Scientific	wind speed, sonic temperature	1
LI-7500 (temporarily)	LI-COR	concentration of H_2O/CO_2	1

Figure 1.11: Three transect stations were installed in summer 2008. The stations provide continuous measurements of soil temperature, soil moisture and surface temperature at the polygonal rim and the center. Moreover, the stations were temporarily used for the mobile eddy covariance measurements.







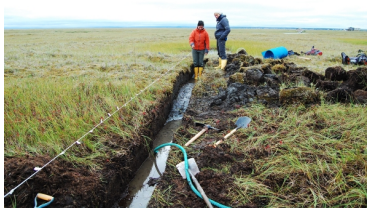

Snow	***Soil***	***Mapping***	***Instrument***
snow water equivalent	soil composition	Aerial Imaging	Nikon D200 (VIS/NIR)
snow density	soil density	Albedo	SP1110, Skye Instruments
heat capacity	heat capacity	Surface moisture	
heat conductivity	heat conductivity	Surface topography	
thermal diffusivity	thermal diffusivity	Vegetation	
depth in transects	thaw depth		
distribution	soil moisture		
	organic content		

Figure 1.12: Ancillary field measurements are conducted during the campaigns in 2007 and 2008.

the harsh winter period. During the field campaign in summer 2008, a second eddy covariance system of similar design was applied as a mobile station to obtain measurements about the spatial variability of the turbulent heat fluxes (Fig. 1.11). The data processing is carried out with the standardized 'QA/QC' software package 'TK2', which contains all state-of-the-art corrections and quality tests (Mauder and Foken 2004, Mauder et al. 2007). A detailed description of the data analysis is given in Chapter 3.

1.4.3 Soil heat fluxes

For the calculation of the soil heat heat flux, two different methods are applied. The first method is based on soil temperature and moisture measurements and calculates the average ground heat flux from changes in the sensible and latent heat content of the soil column. This so-called calorimetric method requires measurements to a depth, where the temperature do not change in the considered time interval. For this purpose, soil temperatures are measured with a thermistor chain in a borehole down to a depth of 26 m (Fig. 1.6). The temperature and liquid water content changes in the active layer zone are measured in a 0.4 m profile using 5 thermistors and 5 Time-Domain-Reflectometry (TDR) soil moisture probes (Fig. 1.6). The liquid soil water content is inferred from the TDR measurements similar to Boike and Roth (1998) and the soil heat capacity, which is required to calculate the sensible heat content of the soil column, is evaluated from soil component analyses (Boike et al. 1998). The calorimetric approach has the advantage that it accounts for the latent heat of freezing, which makes it applicable during the entire annual cycle. The accuracy of this method is limited by the spatial resolution of the temperature and soil moisture profiles and the accuracy of the used sensors. The best results are obtained for large changes in temperature and water content, which makes the calorimetric method most suitable for long-term averages. Details on the method are provided in Chapter 3.
The second method uses shallow temperature profiles close to the surface to evaluate the ground heat flux by solving the equation of one-dimensional heat conduction. The ground heat fluxes determined by this method are mainly based on the near-surface temperature profiles at the Transect stations (Fig. 1.11), which consists of thermocouples. The very small sensors (5 mm) facilitate the placement in thin soil horizons, since the method requires at least three temperature sensors placed in a homogeneous soil layer. The temperature records obtained by the first and the last sensor are used as upper and lower boundary condition for the solution of the differential equation, whereas the middle sensor is used to evaluate the thermal diffusivity. A detailed description of this method is given by Westermann et al. (2009) who successfully applied the method in permafrost soils. This method does not account for the phase change of water and is therefore only applicable, as long as neither freezing nor thawing occurs within the measured temperature profile. The advantage of the conductive method is the high temporal resolution of the obtained ground heat fluxes, whereas on longer time scales, the applicability is limited due to the exclusion of freezing and thawing periods (see details in Chapter 3).

1.5 Main results

The following sections briefly summarize the most essential results of the performed studies, which in detail are documented in the appended articles.

1.5.1 The surface temperature variability

The surface heterogeneity of the polygonal tundra is highest during the summer months, when the landscape is snow-free and the thawed tundra is characterized by dry and wet surface patches. The summertime surface heterogeneity is also reflected in the land surface temperature, which features a high spatial and temporal variability. Spatial temperature differences on the order of 5 °C are frequently observed between dry and wet tundra surfaces, and can exceed differences of 10 °C between dry tundra and water bodies. The magnitude of the surface temperature differences is essentially controlled by the net radiation. The most pronounced differences in the surface temperature are observed during clear-sky conditions at noon, when the incoming solar radiation is highest and the dry surfaces heat up strongly. During clear nights, when the net radiation becomes negative, the surface temperature differences still exist, but are inverted so that the warmest temperatures are now measured at the water surface. The highest temporal variability is measured at the dry tundra surfaces, where the diurnal temperature amplitude can be on the order of 20 °C. In temporal averages of the surface temperature on time scales longer than the diurnal cycle, the spatial differences of the surface temperature are found to be significantly reduced. For weekly averages, maximum spatial temperature differences of about 2 °C are observed between wet and dry surfaces, but the differences are significantly smaller than 1 °C most of the time. Sustained differences of the surface temperature in weekly averages are only observed between the tundra and a small pond, which can be as large as 3.5 °C, but are usually in the range of 1 °C.
The surface temperatures obtained by the high-resolution thermal imaging system are compared with the MODIS L2 LST product. The field measurements are upscaled to the satellite scale ($\approx$ 1 km) by fractional upscaling based on a surface classification of the study site. The direct comparison reveals that most of the satellite data are in good agreement with the ground measurements. However, large data gaps in the satellite dataset, as well as occasional erroneous measurements are noticed. Both findings are most likely related to clouds, which prevent satellite surface temperature detection and, if wrongly classified and not excluded, cause erroneous measurements of the surface temperature. Furthermore, the performance of the satellite product was checked for temporal averages. High accuracies with temperature deviations of less than 1 °C between the averages from field observations and satellite measurements are obtained during periods of predominately clear-sky conditions, whereas the satellite-derived averages can be biased up to 4 °C during overcast conditions.

1.5.2 The surface energy balance during spring, summer and fall

During the period from April to September, the surface energy balance is naturally dominated by the incoming short-wave radiation, which is especially true during the polar day season (Fig. 1.13). About 50% of the available net radiation is balanced by the latent heat flux, whereas the remaining sensible and ground heat fluxes are approximately of similar magnitude (Fig. 1.13). The summertime surface energy balance at the polygonal tundra is therefore essentially characterized by evapotranspiration, with an average Bowen ration close to 0.5.
The most pronounced seasonal changes in the surface energy balance are related to the fast snow melt at the beginning of June, when the surface heat budget experiences a sudden change from winter to summer conditions. The snow melt itself is partly driven by high values of incoming short-wave radiation and the sensible heat flux. After the snow melt, the net radiation increases by a factor of three, which affects all energy balance components. A more gradual transition of the energy balance characteristics is observed after the end of the polar day at the beginning of August. The decreasing surface radiation budget is accompanied by steadily decreasing sensible and ground heat fluxes, whereas the latent heat flux remains relatively high.
Inter-annual variations in the energy balance are observed in spring, before the onset of the snow melt, when the soil temperature evolution is affected by inter-annual differences in the near-surface air temperatures. The most significant variability in the annual surface energy budget occurs in the radiation balance, which is most likely caused by differences in cloudiness. The differences in the radiation budget develop their greatest impact on the ground heat budget during fall, when the timing of refreezing is affected by the slight variations of the net radiation.
The spatial variability of the energy balance is investigated by distributed energy balance measurements. The investigations focus on the most prominent surface types of the wet tundra landscape, which in particular are wet and dry peat tundra surfaces, as well as small water bodies such as polygonal ponds. Radiation balance measurements reveal spatial differences on the order of 5 to 10% between wet and dry tundra surfaces, while larger differences on the order of 20 to 30% are measured between water surfaces and the wet tundra. During the summer months, these spatial differences in the radiation budget are found to be related to variations in the surface albedo, since spatial surface temperature differences are almost non-existent for long-term averages. However, pronounced surface temperature differences between wet and dry tundra surfaces are observed within the diurnal cycle to be on the order of 5 to 10° C. These short-term surface temperature differences indicate micro-scale variations of sensible and latent heat fluxes. Hence, the polygonal surface elements, such as the elevated rims and the lowered centers, constitute different sources for the atmospheric heat fluxes on the landscape scale. The size of the polygonal surface structures therefore determine the larger-scale ratio between sensible and latent heat fluxes (Bowen ratio). These differences are observed with spatially distributed eddy covariance measurements. The most significant differences are observed during situations of high radiative forcing. The measurements reveal that differences of about 20% in the ratio of wet

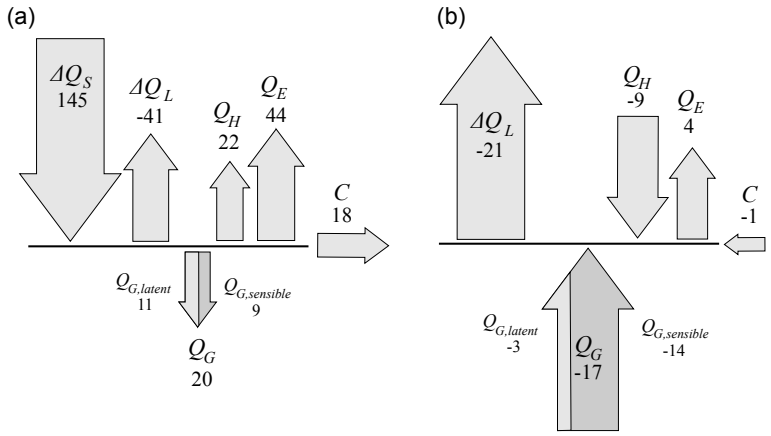

Figure 1.13: The average surface energy balance exemplified (a) for the summer period from July to August 2008 and (b) for the winter period from December 2007 to January 2008. ΔQ_S: net shortwave radiation; ΔQ_L: net long wave radiation; Q_H: sensible heat flux; Q_E: latent heat flux; Q_G: ground heat flux, separated in a sensible and a latent component according to the partitioning of the heat storage in the soil; C: residual of the surface energy balance.

and dry surfaces cause differences on the same order of magnitude in the Bowen ratio.

1.5.3 The winter surface energy balance

During the winter half year (October-April), the net radiation is largely negative (Fig. 1.13). The short-wave radiation budget is either strongly reduced by the high reflectance of the snow cover, or not present during the polar night period. The negative radiation budget is mainly balanced by the ground heat flux, which makes up 50 to 60% of the net radiation (Fig. 1.13). With the beginning of spring, the ground heat flux looses its dominant role in favor of the sensible heat flux. Except for the first weeks of October, the latent heat flux is very small and mainly positive, which indicates that only minor sublimation occurs at the snow cover.

The most pronounced inter-annual differences in the surface energy balance are revealed in the ground heat fluxes during the early winter period, which are related to differences in the snow cover evolution. The refreezing process, which is already delayed by differences in the radiation budget during fall is further delayed by about 14 days owing to a fast snow cover build-up. This difference in the surface energy balance is even more pronounced in the refreezing process of the small ponds, which is about one month delayed compared to a year with lower snow depth.

Hence, it is not surprising to find significant spatial energy balance differences between the freezing tundra soils and the shallow ponds. During the entire winter period, the heat flux released at the investigated pond is about a factor of two higher than the ground heat flux measured for the tundra soils. This agrees well with the radiation budget of the water bodies, which is more negative according to higher surface temperatures.

1.6 Conclusions

In this thesis comprehensive field measurements are conducted, which mainly focus on the soil-atmosphere energy exchange processes. The presented studies aim to achieve a better understanding of the controlling factors of permafrost processes and the different temporal and spatial scales over which they vary. The factors range from the regional synoptic framework to the micro-scale surface characteristics and cover diurnal variations, as well as inter-annual differences. The obtained field measurements have important implications for both permafrost monitoring and modeling, which are summarized in the following sections.

1.6.1 Permafrost monitoring

The surface temperature measurements clearly show that the landscape heterogeneity of the polygonal tundra largely vanishes for averaging periods longer than the diurnal cycle. This has important implications for the resolution requirements of LST-based permafrost monitoring schemes, since micro-scale surface temperature differences are basically negligible for long-term averages. Hence, the spatial resolution of satellite products, as they are provided by the Moderate Resolution Imaging Spectroradiometer (MODIS) appear to be well suited for monitoring application in wet tundra regions. However, this is only valid for temperature differences between wet and dry tundra surfaces, but not for water bodies like lakes and ponds. The results reveal that water bodies feature sustained surface temperature differences compared to tundra soils, even on longer time scales. If water surfaces are frequent, the spatial average could be biased, which consequently limits the validity of coarse-scale LST measurements for permafrost monitoring. It is therefore crucial to control the validity of large-scale LST measurements by high-resolution water masks. Further requirements for LST-based permafrost monitoring are compiled by investigating the performance of MODIS LST at the study site:

- The temporal resolution of the satellite time series is strongly limited by clouds, which leads to a highly clustered temperature record. The unequally spaced time series is problematic for averaging procedures, since clear-sky conditions can be overrepresented in long-term averages. Therefore, it might be necessary to develop gap filling methods. Such procedures could be based on reanalysis products of weather models, from which at least near-surface air temperatures could by inferred during overcast conditions.

- The presence of several erroneous measurements, most likely caused by incorrect cloud detection, indicate that the reliability of the cloud cover mask, as used in the current MODIS LST (version 5) product, must be improved. These measurement errors are largely unidentifiable, if no reference measurements are available. The erroneous surface temperatures lead to strongly biased average values, especially when the data density is low. In the present state, this problem constitutes a major obstacle for the development of reliable gap filling methods.

1.6.2 Permafrost modeling

Long-term energy balance measurements give an insight into the relevance and variability of factors, such as cloudiness, thermal soil properties, or snow cover, for the thermal state of permafrost. Depending on their importance, these controlling factors must be accounted for in the development of permafrost models. The following points give an overview about the factors that are found to significantly affect the permafrost energy budget at the study site.

- The surface heat budget and thus the thermal state of the permafrost is mainly controlled by the radiation balance. The snow-free period is dominated by incoming short-wave radiation, whereas the snow covered period is mainly controlled by the long-wave radiation budget. Both periods are significantly influenced by clouds, which induce strong short-term fluctuations in the radiation budget. On longer time scales, clouds generally lower the net radiation during summer, while they decrease the radiative losses during the winter period. Hence, the average cloud coverage constitutes an important factor for the surface heat budget, which naturally affects the thermal state of the permafrost. The correct representation of the surface radiation budget and thus the average cloud coverage are fundamental prerequisites for the implementation of permafrost into climate models.

- As mentioned above, the surface radiation budget is essentially determined by the presence or absence of snow owing to its high albedo. The impact of the snow cover is largest during spring, when the incoming short-wave radiation is high, but the largest fraction of the incoming short-wave radiation is reflected. Hence, the timing of the snow melt constitutes an important controlling factor of the entire surface energy budget. The measurements reveal that the snow melt event is at least partly triggered by sensible heat fluxes, which are possibly related to the influx of warm air masses and thus to the larger-scale atmospheric circulation. Due to the outstanding impact of the spring time snow cover on the surface energy balance, the timing of snow melt should be represented in model approaches. However, the triggering factors of snow melt are not clear yet and further field work on this issue is required to clarify this important interaction between larger-scale atmospheric conditions and the local surface characteristics.

- The snow cover not only affects the surface radiation, but also the thermal regime of the soil during winter. Inter-annual variations of only a few centimeters of snow substantially affect the ground heat flux and the duration of refreezing. Hence, the snow depth and therefore the wintertime precipitation is a further important controlling factor. It must be emphasized, that variations in the refreezing process can be of importance for the microbial decomposition of organic matter, which essentially depends on temperature and availability of liquid water.

Moreover, the ground heat flux, which is strongly determined by permafrost processes, constitutes a significant component of the surface energy balance. This is especially true

during the winter period, when the largest fraction of the surface heat budget is provided by the ground heat flux. The ratio between sensible and ground heat flux at the study site suggests that an even stronger cooling of the near-surface atmosphere is largely prevented by the strong ground heat flux. This is especially true during the refreezing period, when large amounts of latent heat are released from the uppermost soil layers. It must be emphasized that the ground heat flux dominates the surface energy balance over a period of at least four months and that similar permafrost conditions occur in vast areas of the Arctic. Hence, it is highly desirable to check whether the ground heat flux and the freeze and thaw dynamics are represented realistically in the current climate models. The implementation of permafrost into climate models might help to improve the representation of the soil-atmosphere interactions over vast arctic regions.
Another aspect in permafrost modeling concerns the spatial heterogeneity of the surface energy balance. The largest spatial differences are observed between the tundra surface and shallow water bodies, which feature significant differences during the entire annual cycle. Primarily, these differences become manifest in significantly longer freezing periods of the shallow ponds. This might be important for permafrost modeling, if the freeze and thaw dynamics are evaluated for large tundra areas, where small water bodies are frequent. This is especially true, if such models are used to evaluate the potential microbial activity and carbon decomposition rates.

1.7 Outlook

This study contributes to a better understanding of the energy exchange processes at the arctic tundra, particularly of the spatial and temporal variabilities of the energy flux components and the identification of controlling factors. Based on the results, several implications for both permafrost monitoring and modeling have been explored. In future studies, the following aspects should be further investigated: (i) the timing of snow melt (ii) the impact of small water bodies on the thermal conditions of the permafrost and (iii) the impact of the wintertime ground heat flux on the larger-scale atmospheric conditions. These processes are related to the arctic winter season, which in the opinion of the author deserves much more attention in studies of energy balance processes in the Arctic.

(i) During the snow melt period, pronounced sensible heat fluxes are observed. This suggests that influx of warm air masses could be a triggering factor for the onset of snow melt. Therefore, it is desirable to investigate the timing of snow melt in relation to larger-scale atmospheric circulation patterns. Such analyses could make use of active microwave remote sensing to detect the onset of the snow melt (Bartsch et al. 2007), which are available for more the 10 years. The larger-scale atmospheric conditions could be obtained from e.g. the ERA re-analysis products of the European Centre for Medium-Range Weather Forecasts" (ECMWF).

(ii) Small variations in snow depth lead to distinctly different timing in the refreezing of small water bodies. This suggests that microbial decomposition of organic matter,

which largely depends on temperature and availability of liquid water, can feature a high inter-annual variability. This could significantly affect the emission of greenhouse gases from the northern wetlands. Therefore, it is necessary to further investigate shallow ponds and their potential importance as sources of methane and carbon dioxide. Such investigations could be based on field measurements of gas emissions during the freezing period and satellite-based detection of shallow water bodies.

(iii) The contribution of the ground heat flux to the surface energy balance during the winter period is remarkable. Further investigation might focus on the larger-scale implications of the ground heat flux in permafrost regions during winter. This especially concerns the impact of the ground heat flux on the atmospheric stratification, which may affect larger-scale circulation patterns. Such investigations would require the application of climate models.

1.8 Overview of publications

1.8.1 Spatial and temporal variations of summer surface temperatures of wet polygonal tundra in Siberia - implications for MODIS LST based permafrost monitoring

Authors: M. Langer, S. Westermann and J. Boike
Status of publication: published
Journal: Remote Sensing of Environment 114 (9), 2059-2069, 2010

Authors contributions: The author arranged the experimental setup and conducted the field work. The development of the radiometric and geometric correction algorithms were done in collaboration with the second author Sebastian Westermann. The data analysis and interpretation were performed by the author with contribution of the coauthors. The text is composed by the author, supported by the coauthors.

Julia Boike Sebastian Westermann

1.8.2 Permafrost and surface energy balance of a polygonal tundra site in northern Siberia - Part I: Spring to fall

Authors: M. Langer, S. Westermann, S. Muster, K. Piel and J. Boike
Status of publication: submitted
Journal: The Cryosphere, 2010

Authors contributions: The field work and measurements were mostly carried out by the author. The data processing, analysis and interpretation were performed by the author with support of the coauthors. The text is composed by the author with contributions from the coauthors.

Julia Boike Konstanze Piel

1.8.3 Permafrost and surface energy balance of a polygonal tundra site in northern Siberia - Part II: Winter

Authors: M. Langer, S. Westermann, S. Muster, K. Piel and J. Boike
Status of publication: draft

Author contribution: The author conducted the the largest part of the field work and measurements. The data processing, analyses and interpretation were performed by the author with contributions of the coauthors. The text is composed by the author with contributions from the coauthors.

Julia Boike Konstanze Piel

1.8.4 Further publications

The author of this thesis furthermore contributed to the following publications, which are not presented in this thesis:

Westermann, S., Lüers, J., Langer, M., Piel, K., Boike, J. (2009). The annual surface energy budget of a high-arctic permafrost site on Svalbard, Norway, The Cryosphere, 3, 245-263., http://www.the-cryosphere.net/3/245/2009/tc-3-245-2009.html.

Westermann, S., Langer, M., Boike, J. (2010). Spatial and temporal variations of summer surface temperatures at a high-arctic site on Svalbard - implications for MODIS LST based permafrost monitoring, Remote Sensing of Environment (in review).

Chapter 2

Paper I
Spatial and temporal variations of summer surface temperatures of wet polygonal tundra in Siberia - implications for MODIS LST based permafrost monitoring

2.1 Abstract

The surface temperature of permafrost soils in remote arctic areas is accessible by satellite land surface temperature (LST) detection. However, the spatial resolution of satellite measurements such as the MODIS LST products is limited and does not detect the heterogeneities of the wet polygonal tundra landscape where surface wetness varies over distances of several meters. This paper examines the spatial and temporal variability of summer surface temperatures of a polygonal tundra site in northern Siberia using a ground based high resolution thermal imaging system. Thermal infrared images were taken of a 1000 m^2 polygonal tundra area in 10 min intervals from July to September 2008. Under clear sky conditions, the individual measurements indicate temperature differences of up to 6 K between dry and wet tundra surfaces and which can exceed 12 K when dry tundra and water surfaces are compared. These differences disappear when temperature averages are considered for intervals longer than the diurnal cycle; for weekly averages the spatial temperature variability decreases below 1 K. The exception is the free water surface of a shallow polygonal pond where weekly averaged temperature differences of 2.5 K are sustained compared to the tundra surface.

The ground based thermal infrared images are upscaled to MODIS sized pixels and compared to available MODIS LST data for individual measurements and weekly averages. The comparisons show generally good agreement for the individual measurements under clear sky conditions, which exist during 20% of the studied time period. However, several erroneous measurements and large data gaps occur in the MODIS LST data during cloudy conditions, leading to biased weekly temperature averages inferred from the satellite observations. Based on these results the following recommendations are given for future permafrost temperature monitoring based on MODIS LST products: (i) high resolution surface water masks for the quality assessment in landscapes where lakes and ponds are

frequent and (ii) reliable cloud cover detection in conjunction with a gap filling procedure for accurate temporal averages.

2.2 Introduction

The land surface temperature (LST) is related to all components of the energy balance and is therefore a crucial parameter for the energy budget of permafrost environments. The sensitivity of permafrost towards degradation and the potential activation of a massive carbon source is directly associated with the energy exchange processes occurring at the soil-atmosphere interface. Especially wet tundra landscapes, where large quantities of carbon are stored in frozen organic soils, may become a massive source of green house gases under a warmer climate (Davidson and Janssens 2006). A number of studies revealed a sustained large scale warming of the Arctic during the last decades (e.g. Rothrock et al. 1999, Comiso 2002, Serreze et al. 2003, Stroeve et al. 2005), which is also reported by Comiso (2003) and Comiso (2006) using long term satellite LST measurements. The satellite observations indicate strong warming trends of LST during summer over the entire Arctic, which is essential for the summer thaw depth of permafrost soils. Hence, the monitoring of LST in permafrost environments monitoring of LST can be an important tool to assess the effects of climate change in the usually remote and inaccessible permafrost envirmoments. Land surface temperatures are currently accessible by various remote sensing platforms e.g. Terra/Aqua-MODIS, Terra-ASTER, NOAA-AVHRR, Meteosat-MVIRI, ERS-ATSR and Landsat. Since they are available on a global scale with high overpass frequencies, these products have a great potential for two major applications in permafrost regions.

1. The LST provides access to atmospheric boundary layer processes in regions where climate data are sparse. Efforts have been initiated to synthesize surface-based meteorological data with satellite observations and numerical models in arctic regions (Martin and Munoz 1997, Rigor et al. 2000). In addition, several projects in non-arctic regions, such as FIFE (Sellers et al. 1992), BOREAS (Sellers et al. 1995) and SEBAL (Bastiaanssen et al. 1998), examined surface energy balance models based on satellite products. A detailed overview of LST derived energy balance models is given by Friedl (2002).

2. Land surface temperatures can serve as upper boundary condition in permafrost models, calculating the annual thaw depths and the thermal stability of permafrost soils. Hachem et al. (2008) introduce satellite derived land surface temperatures for permafrost detection, while essential issues such as data gaps due to cloud cover and the decoupling of soil and surface temperatures due to snow cover are addressed. A proposed scheme of satellite based permafrost modeling is given in Marchenko et al. (2009), which makes use of a MODIS LST product in combination with the analytical permafrost model GIPL-1.1. to calculate permafrost active layer dynamics for the entire Arctic.

The spatial resolution of satellite LST products typically ranges from 60 meters (Landsat) to one kilometer (MODIS). Temperature differences on smaller scales are therefore not resolved, but are nevertheless critical when they occur systematically over long time periods. In such cases, they result from sustained differences in the surface energy balance and might indicate differences in the thermal state of the subjacent permafrost, potentially triggering processes such as initial thermo karst erosion. Previous studies in non-arctic regions have outlined the effect of surface heterogeneity on satellite based energy balance detection (Humes et al. 1994, Hall et al. 1992, Friedl 1996, Brunsell and Gillies 2003). In particular, sub-resolution LST variations are expected to occur in highly fractionated landscapes. This is especially true for permafrost environments, such as the wet polygonal tundra, where a sharp contrast between wet and dry surface patches occurs on scales of several meters. Hence, it is desirable to elucidate the sub-resolution surface temperature variability and its impact on the accuracy of satellite permafrost monitoring schemes.

In this paper, we present summer surface temperature observations using a tower-mounted high resolution thermal imaging system at a Siberian polygonal tundra site. This surface type is characteristic for a large area of circumpolar wet tundra landscapes. At first, the spatial and temporal variability of surface temperatures obtained with the thermal camera is analyzed for the snow free period. Secondly, the MODIS L2 LST product (Wan 2008) is compared to up-scaled LST data from the thermal camera and evaluated with respect to its applicability for the monitoring of permafrost active layer dynamics in wet polygonal tundra landscapes.

2.3 Site characteristics

The study was performed on Samoylov Island (72° 22' N; 126° 30' E), which represents a typical Siberian wet tundra landscape in the zone of continuous permafrost (Fig. 2.1a). Samoylov Island is located in the upper plain of the Lena River Delta, close to one of the main river channels (Fig. 2.1b). The region is characterized by an arctic continental climate. The mean annual air temperature (MAAT) at Samoylov Island is -14.7 °C and the total annual precipitation is around 250 mm, showing high inter-annual variations (Boike et al. 2008). Snowmelt and Lena ice drift typically start in the beginning of June and the snow free season lasts from mid-June to mid-September. The regional permafrost in the region reaches depths of $500 - 600$ m (Grigoriev 1960) and is characterized by a very low temperature of -9.2 °C at the depth of zero annual amplitude approximately 10 m beneath the surface. Samoylov Island covers an area of 4.3 km^2. While the western part of the island is characterized by a recent flood plain, the eastern part consists of an elevated terrace $10 - 16$ m a.s.l. (Fig. 2.1c). This terrace is characterized by wet tundra showing the typical polygonal micro-relief, which features elevation differences of 0.2 to 1.0 m. The size of the polygons typically ranges from 5 to 10 m. The depressed polygonal centers consist of water saturated peat soils or they constitute shallow ponds. The vegetation at these wet locations is dominated by hydrophilic sedges and mosses (Kutzbach et al. 2004). The lowered centers are surrounded by elevated dry polygonal rims, which are dominated by

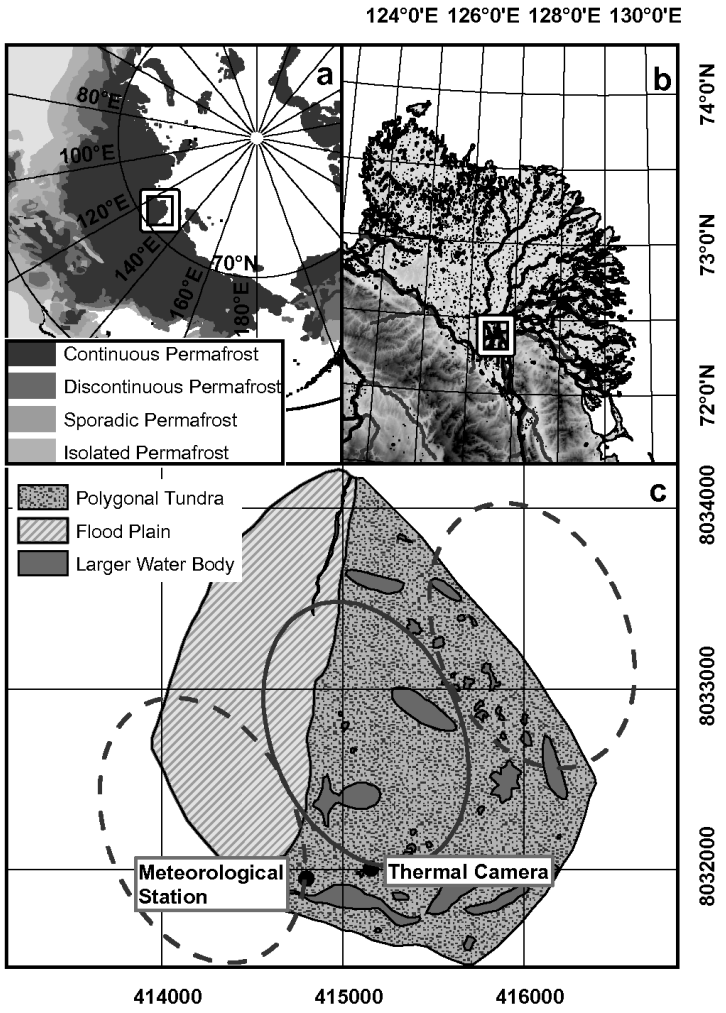

Figure 2.1: (a) Location of the Lena River Delta in northern Siberia, the map shows the permafrost boundaries (Brown et al. 1997). (b) Location of Samoylov Island in the upper plain of the Lena River Delta close to one of the main river channels. (c) Measurement site on Samoylov, the ellipses show typical footprint areas of the MODIS scanner swath; the dashed ellipses indicate footprint areas which do not fit the 80% overlap criterion with the island (see Sec. 2.4.6).

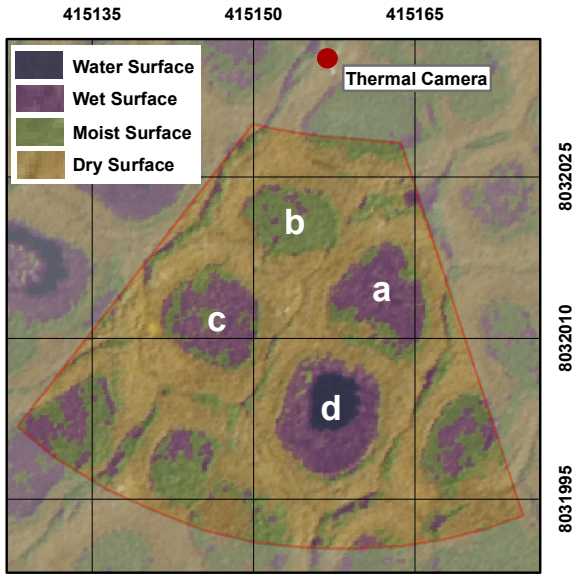

Figure 2.2: Field of view of the thermal imaging system (about 1000 m^2). Surface classification based on aerial images taken on 08/15/2008 (projection: UTM 52N WGS84). The considered polygonal structures (a) and (c) are typical low center wet polygons with moss dominated centers, while polygon (b) is dominated by sedges and polygon (d) is filled by a shallow pond with a free water surface.

mesophytic dwarf shrubs, forbs and mosses (Kutzbach et al. 2004, Sachs et al. 2008).

The experimental plot is located on the elevated terrace. It consists of three low center polygons and one polygonal pond surrounded by elevated dry rims (Fig. 2.2). Polygon (a) (Fig. 2.2) is characterized by a wet peaty center, which is dominated by hydrophilic mosses such as *Limprichtia revolvens*. Vascular plans are only sparsely distributed, while some mosses (pillows of *Aulacomium turgidum*) occur at the transition of the dry rim and the wet center. The vegetation of polygon (b) (Fig. 2.2) is characterized by sedges (*Carex aquatilis*) with a growth height of 20 cm. The sedge canopy is underlain by hydrophilic mosses. Polygon (c) (Fig. 2.2) is comparable in shape to polygon (a). It shows a similar vegetation cover, but is characterized by an increased number of isolated moss pillows (*Aulacomium turgidum*) occurring in the transition zone and in the polygon center. Polygon (d) (Fig. 2.2) contains a shallow pond, about 1.5 m deep. The edge of the pond is covered by sedges. The dry polygon rims are generally dominated by mesophilic mosses, such as *Hylocomium splendens*. Considerably more vascular plants occur at the dry locations. The elevation differences of the investigated polygons vary between 0.2 to 0.5 m. The water level is mostly located directly underneath the surface of the wet polygonal centers, resulting in a patchy structure of puddles and moss agglomerations. During the observation period the water level decreased about 5 cm, while occasional rain events temporarily raised the water

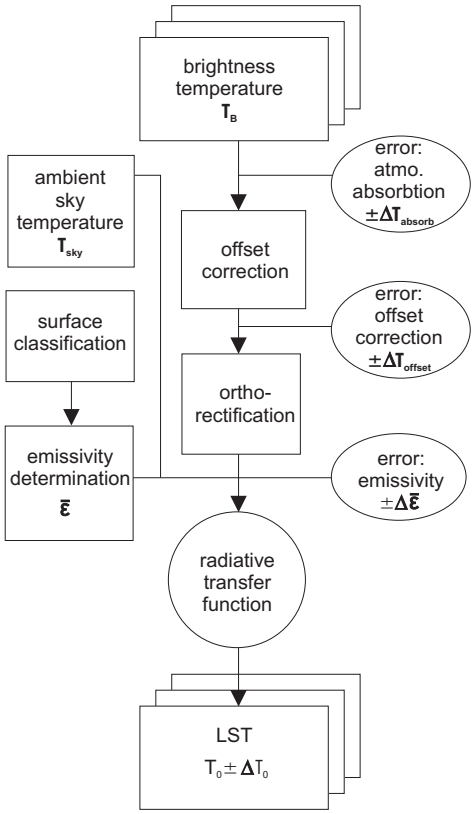

Figure 2.3: Work flow of the thermal camera data processing from brightness to land surface temperatures (LST) including error margins. Total errors ΔT_0 are based on gaussian error propagation.

table.

2.4 Methods

2.4.1 Experimental setup

The surface temperature measurements were conducted using a tower mounted high resolution thermal camera (VARIOCAM HR, Infratec GmbH, Dresden, Germany). The VARIOCAM thermal imaging system consists of an uncooled microbolometer detector with a resolution of 384 x 288 pixels. The spectral sensitivity ranges from 7.5 to 14 µm and the imaging system is equipped with a 12 mm wide angle lens. The camera is mounted on an 11 m tower and is oriented south with an off-nadir angle of 55°. This inclination is consistent with the recommended angles for radiative temperature measurements of vegetated surfaces (Huband and Monteith 1986, Vining and Blad 1992). The setup facilitates continuous surface temperature measurements of an area of about 1000 m^2 (Fig. 2.2). The measurements

were conducted from end of July until end of September 2008. With a measurement interval of 10 minutes, a database of more than 7000 thermograms could be obtained.
Ancillary meteorological data such as radiation, precipitation and soil temperatures are obtained in the immediate vicinity of the measurement plot (Fig. 2.1). Soil temperatures are detected by three thermistor profiles (T107, Campbell Scientific Incorporated, Logan, Utah, USA) and the precipitation is measured by an automatic rain gauge (ARG100, Ingenieursbureau Wittich & Visser, Netherlands). The radiation balance is detected by a four component radiation sensor (CNR1, Kipp & Zonen, Delft, Netherlands), calibrated according to WMO standards. In this study, the radiation directed towards the surface is defined as positive. During the measurement period high resolution visible (VIS) and near infrared (NIR) orthorectified aerial images of Samoylov Island were obtained (cp. Scheritz et al. 2008). To obtain a land cover classification, the aerial photographs are further processed by a supervised maximum likelihood classification. We distinguish water bodies, wet, moist and dry surfaces (Fig. 2.2). The entire area of the island consits of 15% free water surfaces, 26% wet areas, 32% dry surfaces and 27% moist areas.

2.4.2 Theory

According to Planck's law the emitted spectral intensity of a black body $B(T, \lambda)$ is related to its temperature T,

$$B(T, \lambda) = \frac{2hc^2}{\lambda^5} \frac{1}{e^{\frac{hc}{\lambda kT}} - 1}, \tag{2.1}$$

where λ is the wavelength, h the Planck constant, k the Boltzmann constant and c the speed of light. Following the terminology of Norman and Becker (1995), surface temperatures obtained from radiance measurements under the black body assumption are called brightness temperatures T_B. The thermal camera is calibrated to deliver brightness temperatures, from which we can evaluate the corresponding radiation $R_s(T_B)$ received at the thermal imaging system in the 7.5 to 14 µm spectral window

$$R_s(T_B) = \int_{7.5\mu m}^{14\mu m} B(T_B, \lambda)\, d\lambda\,. \tag{2.2}$$

Natural surfaces usually do not feature black body characteristics. The spectral intensity of thermal radiation B_n leaving a natural surface is modified due to the spectral emission characteristics of the surface. Using Kirchhoff's law we obtain:

$$\begin{aligned} B_n(T_0, \theta, \phi, \lambda) &= \epsilon(\theta, \phi, \lambda)\, B(T_0, \lambda) + \\ &+ [1 - \epsilon(\theta, \phi, \lambda)]\, B_{sky}(\theta', \phi', \lambda)\,, \end{aligned} \tag{2.3}$$

where T_0 denotes the surface temperature, ϵ the spectral directional emissivity and B_{sky} the

spectral intensity of the sky radiation. Note that the emissivity and sky radiation induce an angular dependence from the zenith angle θ and azimuth angle ϕ with the corresponding opposite angles (θ', ϕ'). The thermal radiation leaving the surface is affected by absorption and emitted thermal radiation originating from the traversed air column, which can be accounted for by a transmission coefficient τ, depending on the path length s and an additional radiation source B_{air}, respectively. Using Eq. 2.3 we obtain

$$\begin{aligned} R_s(T_0,\theta,\phi,s) &= \int_{7.5\mu m}^{14\mu m} \tau(s,\lambda)\,[\epsilon(\theta,\phi,\lambda)\,B(T_0,\lambda) + \\ &+ [1-\epsilon(\theta,\phi,\lambda)]\,B_{sky}(\theta',\phi',\lambda)] + \\ &+ B_{air}(s,\lambda)\,d\lambda\,. \end{aligned} \tag{2.4}$$

For our analysis, the following assumptions are used:

1. The absorption and emission of thermal radiation in the traversed air column is mostly due to water vapor. In our case, the maximum path length through the air column is 35 meters, and the maximum absolute air-water content measured during the study period is 14 gm^{-3} (LI-7500 gas analyzer located 300 m from the study site). The combined effect of absorption and emission of radiation in the air is evaluated for the measured temperature and humidity range using the 'libRadtran' software package based on the 'uvspec' radiative transfer model (Mayer and Kylling 2005). The results indicate a maximum modification of 0.4% of the thermal radiation received at the thermal camera. This results in a maximum error ΔT_{absorb} of about 0.3 K in surface temperature, which we include in our error analysis (Fig. 2.3).

2. We assume an emissivity $\bar{\epsilon}$, which is independent of wavelength and view angle. The resulting error ranges from 0 to 1.5 K and is included in the error calculation (see Sec. 2.4.3 and Fig. 2.3).

3. The thermal sky radiation is assumed to be isotropic. The downwelling sky radiation measured by the pyrgeometer R_{sky} (spectral range from 5 to 42 µm) is used to estimate the thermal radiation emitted by the sky over the entire spectral range. The ambient sky temperature T_{sky} is calculated assuming black-body behaviour using Stefan-Boltzman's law:

$$R_{sky} = \sigma\, T_{sky}^4\,, \tag{2.5}$$

where σ denotes the Stephan-Boltzmann constant. With T_{sky}, we can evaluate $B_{sky}(\lambda)$ similar to Eq. 2.1

The black body assumption is a good approximation for overcast conditions, which prevail during a large part of the study period (see Sec. 2.5.1). An additional error

may occur for clear sky conditions, where the spectral distribution of the sky radiation is different from a black body.

As a result of these assumtions, Eq. 2.4 can be simplified to:

$$\begin{aligned} R_s(T_0, T_{sky}, \bar{\epsilon}) &= \bar{\epsilon} \int_{7.5\mu m}^{14\mu m} B(T_0, \lambda)\, d\lambda + \\ &+ (1 - \bar{\epsilon}) \int_{7.5\mu m}^{14\mu m} B(T_{sky}, \lambda)\, d\lambda\,, \end{aligned} \tag{2.6}$$

where $\bar{\epsilon}$ is the effective emissivity as described in Eq. 2.7 in the following section. Using Eq. 2.2 and Eq. 2.6, the surface temperature T_0 can be evaluated via a numerical equation solver (MATLAB). Note that the solution is unambiguous, since the integral over Planck's function from 7.5 to 14 µm is monotonous with respect to temperature in the relevant temperature range.

2.4.3 Land surface emissivity determination

The land surface emissivity (LSE) is a crucial parameter for radiative measurement of surface temperatures (see Sec. 2.4.2). We determine emissivities using the land cover classification based on aerial images (Fig. 2.2). We distinguish water and dry vegetation as two basic classes, for which we use spectrally resolved emissivities provided by the MODIS USCB emissivity library (Wan and Zhang 1999). The corresponding effective emissivity values $\bar{\epsilon}$ in the 7.5 to 14 µm window are then calculated as:

$$\bar{\epsilon} = \frac{\int_{7.5\mu m}^{14\mu m} \epsilon(\lambda) B(T_0, \lambda)\, d\lambda}{\int_{7.5\mu m}^{14\mu m} B(T_0, \lambda)\, d\lambda} \tag{2.7}$$

This yields emissivities of 0.985 for water and 0.964 for dry vegetation. Note that the temperature dependence of $\bar{\epsilon}$ is negligible in the considered temperature range from −10 °C to 40 °C (around 0.0005). The emissivities of the wet and moist tundra classes are set by estimating the fractions of water and dry vegetation in each class from field observations, with 50% water and 50% dry vegetation for wet tundra and 25% water and 75% dry vegetation for moist tundra, respectively. This results in emissivity values of 0.975 for wet tundra and 0.969 for moist tundra. Our values are in good agreement with published emissivity values for similar surfaces, which range from 0.96 for dry vegetation to 0.99 for water (Salisbury and D'Aria 1992, Rees 1993, Snyder et al. 1998).

A potential view angle dependence of the emissivity, which may become substantial under extreme off-nadir angles, induces uncertainty in the obtained surface temperature T_0 (Becker

et al. 1985, Labed and Stoll 1991, Snyder et al. 1997; 1998). Norman and Becker (1995) report a slight decrease of the emissivity of about 0.01 for forest canopies at off-nadir angles of 75°. Snyder and Wan (1998) compare modeled and measured directional emissivity values. They report a maximum emissivity decreases of 0.046 for savanna, 0.042 for dry soils and 0.01 for water. Following these reported angular emissivity variations, we assume a maximum error $\Delta\bar{\epsilon}$ of 0.04 for all used emissivities. For the emissivity values calculated above, this error margin also accounts for possible wrongly classified points. Furthermore, all measurements under off-nadir angels of more than 75° are excluded from our analysis. The induced error on temperature due to the uncertainty of the emissivities is included in the error calculation (Fig. 2.3). This temperature error is small when the ambient sky temperature approaches the surface temperature (see Eq. 2.6), which is the case for overcast conditions, which frequently occur at the study site.

2.4.4 Offset correction

The thermal imaging system shows a vignetting-like decrease in the measured temperatures from the center towards the edges, which becomes obvious during overcast conditions, where surface temperatures show almost no spatial variations. The temperature offset is circular, with a maximum value of 0.8 K at the corners of the image. Due to the shape and the consistent occurrence in thermograms with little temperature variation, we can assume the temperature offset to be a systematic error present within the entire data set. To correct for the offset on the edges of the thermograms, a two-dimensional second-order polynomial with rotational symmetry is fitted to more than 400 scenes with approximately homogeneous surface temperatures. From this, an average correction matrix is extracted, which is used for correction of the entire data set. The variability within the 95% confidence limits of the fitted polynomial coefficients is used to provide an error estimate on the temperatures due to the correction procedure. The maximum errors occurring at the edges of the thermograms are on the order of 0.2 K, which we assume to be an additional temperature uncertainty ΔT_{offset} induced by the offset correction procedure. The temperature uncertainty is included in the error analysis (Fig. 2.3).

2.4.5 Geometrical correction

To obtain spatially resolved surface temperature measurements with equal pixel sizes it is necessary to orthorectify the thermograms. This geometrical correction is accomplished by a transfer function, which accounts for the internal camera geometry and the external orientation parameters (Slama et al. 1980). The internal camera parameters include the sensor and pixel size, the focal length and two radial lens distortion parameters. The external camera orientation is defined by the position and the view angles of the imaging system. While the sensor and pixel size are provided by the manufacturer of the thermal imaging system, the remaining parameters can be calculated from a sufficiently large set of image and corresponding ground control points (Slama et al. 1980). This set of points is obtained by relating distinct features in the thermograms to structures of an orthorectified

aerial image where the coordinates are known. Hereby, the small elevation differences of the micro-relief are neglected and the images are projected on a plane. The resulting horizontal displacement error is smaller than 1.0 m.

2.4.6 Satellite dataset

We evaluate the performance of the MODIS L2 LST products (MOD11L2.5 and MYD11L2.5) obtained by the satellites Terra and Aqua at the study site. The satellite data are obtained from the National Aeronautics and Space Administration Land Processes Distributed Active Archive Center (Wan 2008). These products contain processed surface temperatures using the generalized split window approach (Wan and Dozier 1996). The L2 product provides the unprojected swath data format (Wan 2009), from which the footprint area of the MODIS pixels and the exact acquisition time can be calculated. In the case of Samoylov Island, which only covers an area of about 4.3 km^2, it is crucial to control the footprint area to avoid influences of the surrounding Lena River. For the footprint analysis, the field of view of each sensor pixel is assumed to be circular (Nishihama et al. 1997). Based on internal sensor parameters such as focal length and sensor size, the measurement spot is projected on the earth surface, resulting in an elliptically shaped footprint of a sensor pixel. Depending on view angle and distance, the measurement spot varies in shape and size (see Fig. 2.1c for example). The region of interest within the satellite scene is selected to represent the surface of the entire island (compare Sec. 2.3). Mixed pixels containing fractions of the Lena River of more than 20% are discarded (see Fig. 2.1c). Due to the polar orbits of the satellites Terra and Aqua, a high overpass frequency is obtained in polar regions. Hence, up to 18 satellite scenes are potentially available per day at the investigation site. During the observation period from end of July until end of September 2008, a total of 1077 MODIS granules is used.

2.5 Results

2.5.1 General synoptic conditions

The measurement period extends from the end of the polar day season until equinox in fall (08/01 - 09/17) (Fig. 2.4). It can be divided into three distinct periods, each characterized by different weather conditions (Fig. 2.4a). The first period (08/01 - 08/19) is characterized by large positive values of net radiation, high surface temperatures and a warming of the subjacent soil. The second period (08/20 - 09/02) is dominated by cloudy conditions with frequent rain events and low values of net radiation. This results in generally low surface temperatures, which are associated with decreasing soil temperatures. Due to lower sun angles and increased night hours, the third period (09/03 - 09/17) is characterized by steadily decreasing surface and soil temperatures. However, clear sky conditions frequently occur especially in the middle of period (3), but are interrupted by sporadic rain events. Towards the end of the third period the surface temperatures sometimes fall below the freezing point, which results in occasional ice layer formation at the polygonal pond.

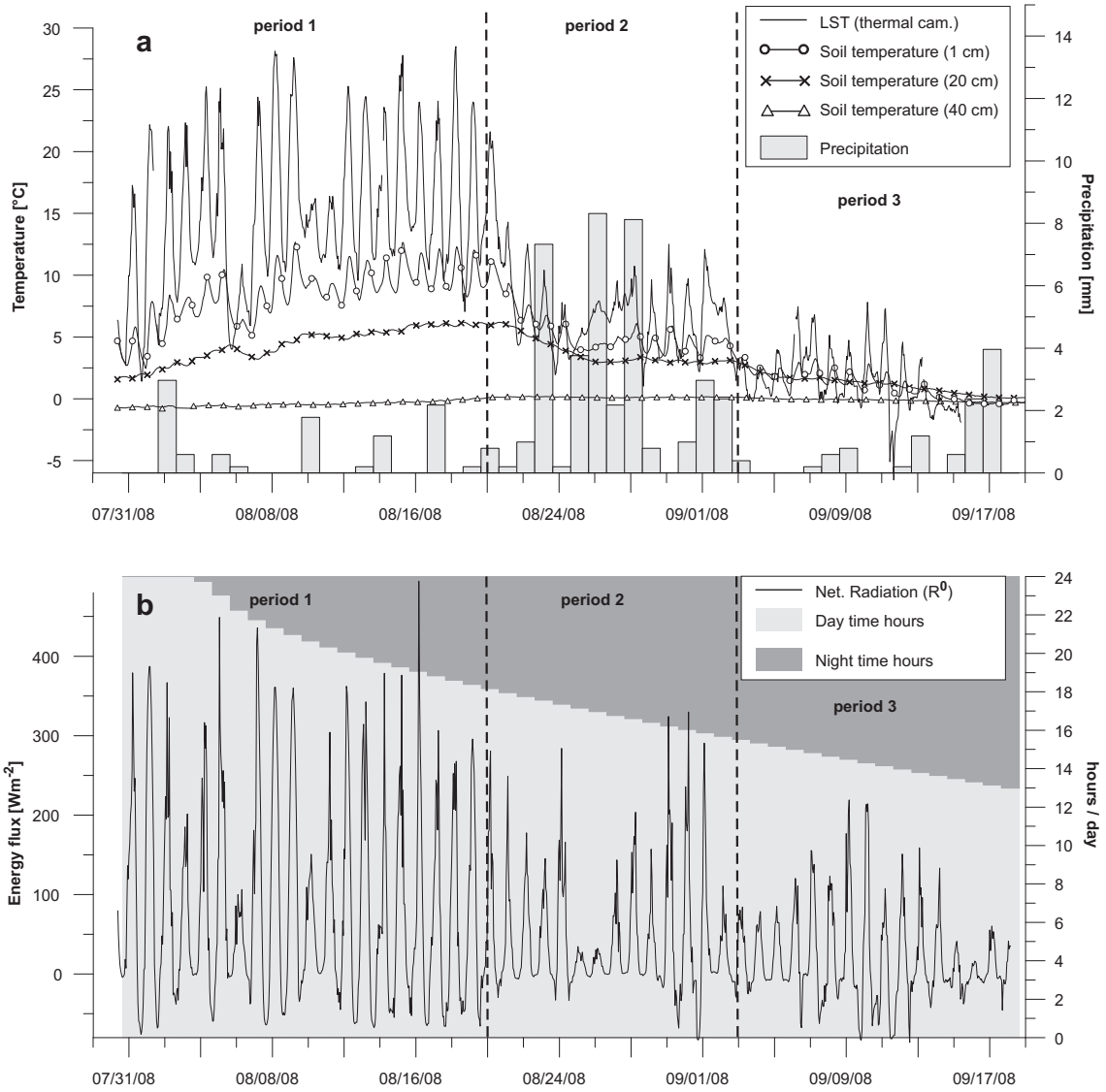

Figure 2.4: (a) Seasonal variations of surface temperature, precipitation and soil temperatures in 1 cm, 20 cm and 40 cm depth during the observation period in 2008. (b) Seasonal variations of net radiation and day time hours during the observation period. The observation period is divided in three distinct intervals of synoptic conditions.

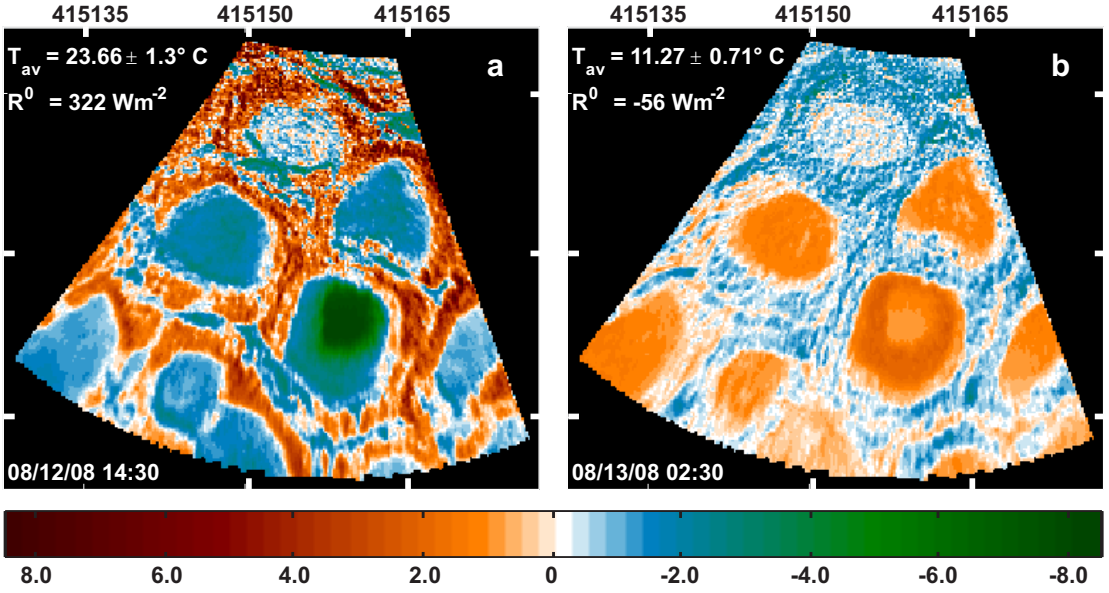

Figure 2.5: Surface temperature differences in Kelvin from the average scene temperature T_{av} for (a) day and (b) night time situation under clear sky conditions. The examples illustrate the highest sun position at 08/12/08 (a) and the lowest sun position at 08/13/08 (b) reached 2.5 hours after local noon and midnight (times in the diagrams are local times). The average scene temperature T_{av} is defined as the average over the entire thermogram with the average error margines $\pm\Delta T_{av}$. R^0 denotes the net radiation.

2.5.2 Short term spatial variability

A typical day and night time surface temperature situation under clear sky conditions during period (1) is displayed Fig. 2.5. These examples, in which the net radiation R^0 amounts to 330 W m^{-2} during the day and -50 W m^{-2} during the night, illustrate the surface temperature variations as they occur under strong radiative forcing. The orthorectified thermograms show the difference of each pixel from the average temperature over the entire field of view, which we define as the average scene temperature T_{av}. During day time a sharp temperature contrast exists between the dry polygonal rims and the wet centers (Fig. 2.5a). The observed deviations from the average scene temperature are 4 to 6 K for the dry rims, -2 to -1 K for the wet centers, and about -6 K for the pond. These spatial surface temperature differences are clearly outside the total error margins ΔT_0, which are 1.0 K for the scene average. The largest error is found at the dry rims, which could be as large as 1.7 K, while the lowest temperature uncertainty of 0.6 K occurs at the free water surface. Compared to the other wet locations, polygon (b) shows a higher surface temperature with no difference to the scene average. The increased temperature of polygon (b) is probably explained by the high fraction of vertically oriented dry vegetation elements seen by the inclined imaging system, since polygon (b) is dominated by sedges (compare Sec. 2.3). During night time the temperature situation reverses (Fig. 2.5b) and the temperature differences between the wet and dry surfaces are less pronounced. Now the dry locations are about 1 K colder than the scene average, including the sedge dominated center, which again is in contrast to the other wet locations. The other wet locations remain 1.0 to 1.5 K warmer than the average scene temperature, which reflects the large heat storage capacity of the water saturated soils. During the night the polygonal pond remains the warmest surface, with a temperature of 2 K above the scene average. Even so, the spatial temperature differences are less pronounced, they are still larger than the found maximum temperature error of 0.7 K found at the dry rims. The different temporal temperature behavior of wet and dry surfaces is mostly a result of distinctly different diurnal temperature amplitudes. For the given example, the diurnal temperature amplitude of the dry rims is twice as large as at the one of the wet polygonal centers.

Under cloudy conditions or low sun angles as typical for periods (2) and (3), the temperature contrast between wet and dry locations is less pronounced. This is illustrated in Fig. 2.6, which shows the relationship between the net radiation R^0 and the temperature differences between the scene averages T_{av} and the single surface classes T_0, such as wet, moist, dry and water surfaces (compare Sec. 2.4.1). For high values of net radiation, significant differences between surface temperatures are observed, while these differences vanish for zero net radiation. The net radiation can hence be identified as the main factor for the formation of spatial temperature variations. A significant spread remains (see Fig. 2.6), which can be explained by the influence of other components of the surface energy budget, such as sensible, latent and ground heat fluxes. For positive values of net radiation, the temperatures of dry surfaces are increased compared to the wet and moist surfaces. The most pronounced temperature difference to the average scene temperature is found for the free water surface of the polygonal pond. This behavior reverses for a negative net radiation

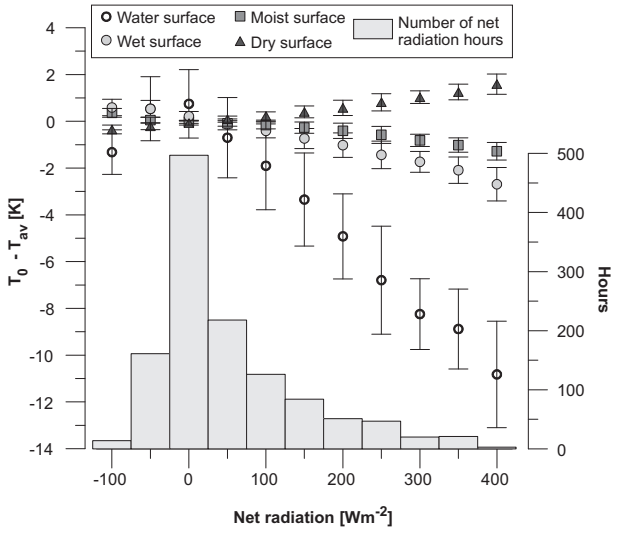

Figure 2.6: Surface temperature differences from the scene average ($T_0 - T_{av}$) versus net radiation, as found for hourly averages of the different surface classes. The binning of the net radiation is set to 50 W m^{-2}, the standard deviations within the radiation classes are indicated by error bars. The histogram shows the distribution of net radiation hours as they occur during the observation period.

budget, with exception of the free water surfaces. The very low surface temperatures of the water body during the periods of highly negative net radiation (-100 W m^{-2}) lead to significant negative temperature difference to the scene average. This behaviour could be associated with occasional ice cover formation during these times. As shown in Fig. 2.6, the measurement period is dominated by net radiation values between -50 and 50 W m^{-2}, while conditions of high radiative forcing are comparatively rare. Hence, the temperature distribution is rather homogeneous for a large part of the study period. Situations with pronounced surface temperature differences, as shown in Fig. 2.5, are not characteristic for the observation period.

2.5.3 Long term spatial variability

Since the diurnal temperature cycle is damped rapidly in deeper soil layers, only the average surface temperature trend is reflected in the development of the ground temperatures. Fig. 2.4a displays surface temperatures and corresponding soil temperatures at depths of 1, 20 and 40 cm, which show that the diurnal temperature cycle is damped out below 20 cm depth. In contrast to the short term diurnal temperature variations, the long term surface temperature signal determined by the three synoptic periods propagates down to the freezing front. Since significant temperature changes usually occur on time scales longer than one week, weekly averages of LST are appropriate time intervals to resolve the general soil thermal dynamics during the observation period. The spatial variability of the surface

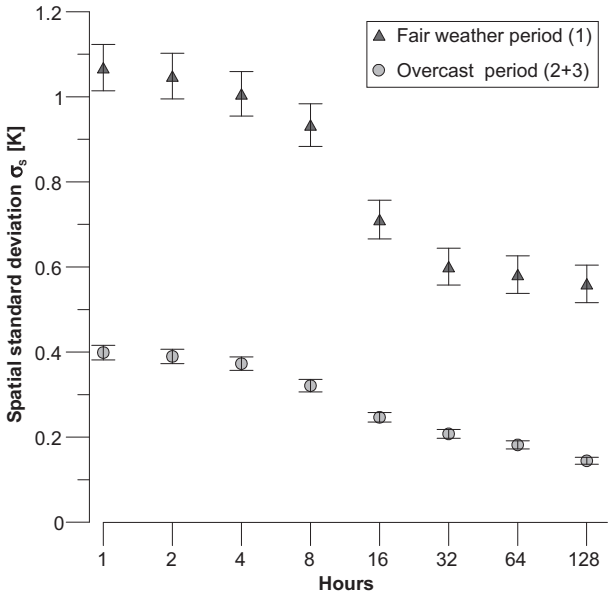

Figure 2.7: Reduction of the mean spatial standard deviation due to increasing temporal averaging intervals for periods dominated by fair weather and overcast conditions. The standard deviations over the scenes are a good approximation for the spatial surface temperature variability. In both cases, the initial variability is reduced by a factor of two after averaging over more than 128 hours. Note that the time scale is logarithmic.

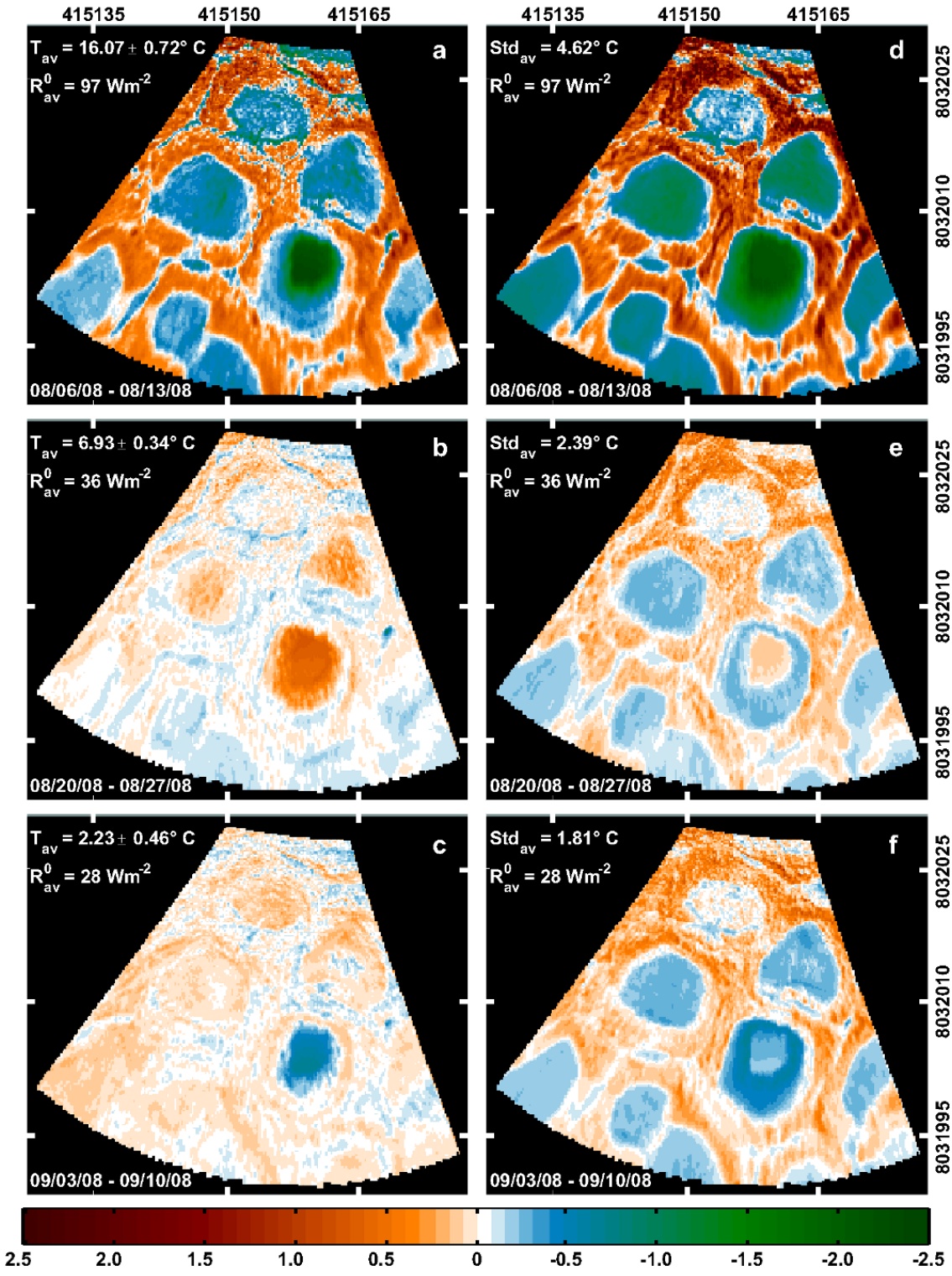

Figure 2.8: Weekly averages of surface temperature variations in Kelvin in the periods 1 (a), 2 (b), and 3 (c) (similar to Fig. 2.5). Surface temperature differences steadily decrease over the course of the observation period. The same is found for the corresponding standard deviations Std_{av} (d, e, f), but they show a higher spatial contrast. R^0_{av} denotes the average net radiation. Note that the colorbar is valid for all thermograms.

temperatures can only lead to temperature differences in deeper soil layers, if the surface temperature differences are persistent in averages over such longer periods.

To investigate the general effect of temporal averaging on the spatial temperature variability, the spatial surface temperature variability is evaluated for a number of different averaging intervals (Fig. 2.7). We only illustrate averaging intervals up to 128 hours, since no significant changes occur for longer intervals. We divide the entire measurement period in predominately fair weather (period 1) and overcast (period 2 + 3) conditions. Averaged time series of thermograms are constructed from these subperiods, featuring averaging intervals between 0 and 128 hours. From the obtained aggregated time series we evaluate the average spatial standard deviations (σ_s), which give us a measure of the spatial surface temperature variabilty during the subperiods. It can be seen in Fig. 2.7, that the averaging procedure significantly reduces the spatial variability in surface temperature. The spatial standard deviations of the fair weather condition decrease from about 1.1 K to 0.6 K for averaging intervals of 1 and 128 hours. Compared to the fair weather conditions, the spatial temperature variability is generally lower for the overcast periods, which is a result of decreased radiative forcing under cloudy conditions (see Sec. 2.5.2). During the overcast periods, the average spatial standard deviation is 0.4 K for 1 hour averages, which again decreases by a factor of two for intervals of 128 hours. The most effective reduction of temperature variability occurs when the averaging interval covers the time span from solar noon to solar midnight, so that the diurnal amplitude averages out. Since the displayed standard deviations are based on averaging intervals starting at solar noon, the most pronounced reduction of spatial temperature variability occurs at the 12 hour interval for both synoptic situations (see Fig. 2.7).

In any case, the spatial variability of surface temperature is strongly reduced for averaging periods of one week, which determine the general temperature development of the subjacent soil column. Three examples of weekly averaged thermograms, each representative for one period as shown in Fig. 2.4, are displayed in Fig. 2.8a-c. The temporal variations within the weekly averages are indicated as images of standard deviation (Fig. 2.8d-f). Sustained differences in average surface temperatures are only observed during period (1). With a total temperature difference of about /unit1K between dry and wet surfaces, they are small and in the range of the error ΔT_0, which amounts to 0.8 K for the dry rims and to 0.6 K for the scene average. The only considerable temperature difference to scene average of -2.2 K is generated at the free water surface of the pond, where the temperature uncertainty is found to be 0.5 K (see Fig. 2.8a). The pronounced diurnal cycle, as described in Sec. 2.5.2, results in high values of the standard deviation (Fig. 2.8d). A sharp contrast exists between the standard deviations of the wet and dry surfaces, which reflects their differences in the diurnal temperature amplitude. The average values of the period (2) show only insignificant spatial differences in surface temperature (Fig. 2.8b). The pond is now warmer than the other surfaces, which is probably due to the large heat storage of the water body. The predominately cloudy conditions with low values of net radiation during period (2) lead to reduced standard deviations (Fig. 2.8e), which indicate the reduced diurnal temperature amplitude compared to period (1). Furthermore, strong temperature differences occur relatively rarely in period (2), which is reflected in the reduced spatial contrast of the

standard deviation. During the third period (Fig. 2.8c), almost no temperature differences are observed between the wet polygonal centers and the dry rims. The average surface temperature is close to the freezing point and occasional ice cover formation on the pond has been observed towards the end of period (3). This ice cover possibly explains the pond surface temperatures well below the freezing point, but the effect is not fully understood since only few data are available at the very end of the observation period. Compared to the previous period, the standard deviation does not show significant differences (Fig. 2.8f). With exception of the free water surface, the observed spatial temperature differences during period (1) and period (2) are not significant because they fall within the margin of error, which is in the order of 0.4 K for both periods.
In the weekly averages only the pond shows a surface temperature, which is distinctly different from the other surfaces. The temperature differences between wet and dry tundra surfaces are reduced to an insignificant level within the weekly averages. These results demonstrate that almost no long-term spatial temperature differences occur at the polygonal tundra surface. Hence, sustained surface temperature differences due to the heterogenic surface characteristics of the polygonal tundra can be excluded as a potential source of spatial variability soil temperatures in deeper layers.

2.5.4 MODIS surface temperature observations

We compare the MODIS MOD11L2.5 and MYD11L2.5 LST products with the surface temperature measurements of the terrestrial thermal imaging system (Fig. 2.9). The local surface temperature measurements of the thermal camera are upscaled by weighting the fractions of 26% wet, 27% moist, 32% dry and 15% water areas, as obtained by the land cover classification over the entire island (see Sec. 2.4.1). The surface classes are uniformly distributed over the island, so that all valid MODIS footprint areas represent the surface composition of the island. The average measurement density during the entire observation period is two measurements per day. The strong reduction of the potential 18 overpasses per day not only originates from cloud cover, but also from footprint areas, which do not match the 80% overlap criterion (see Sec. 2.4.6 and Fig. 2.1). Especially satellite measurements under oblique angles produce footprint areas, which are much larger than the optimum footprint area of 1 km^2 and can exceed the total surface area of the island. In general, the satellite data are in good agreement with the measurements of the thermal camera (Fig. 2.9). Nevertheless, on few occasions the satellite measurements deviate strongly from the terrestrial observations, most likely caused by incorrect cloud cover evaluation. These measurements are found to be 5 to 15 K colder than the temperatures inferred from the thermal camera, which indicates that cloud top temperatures are measured rather than land surface temperatures. For this reason, these data values are classified as erroneous measurements (Fig. 2.9). In addition to the cloud cover mask, the MODIS product provides quality flags, which might help to exclude cloud affected data values. The flags indicate that almost the entire data set is affected by nearby clouds. A general exclusion of these data would result in a 90% reduction of the data set over the entire period, which would be an unnecessary limitation, since most data values are found to be reasonable compared

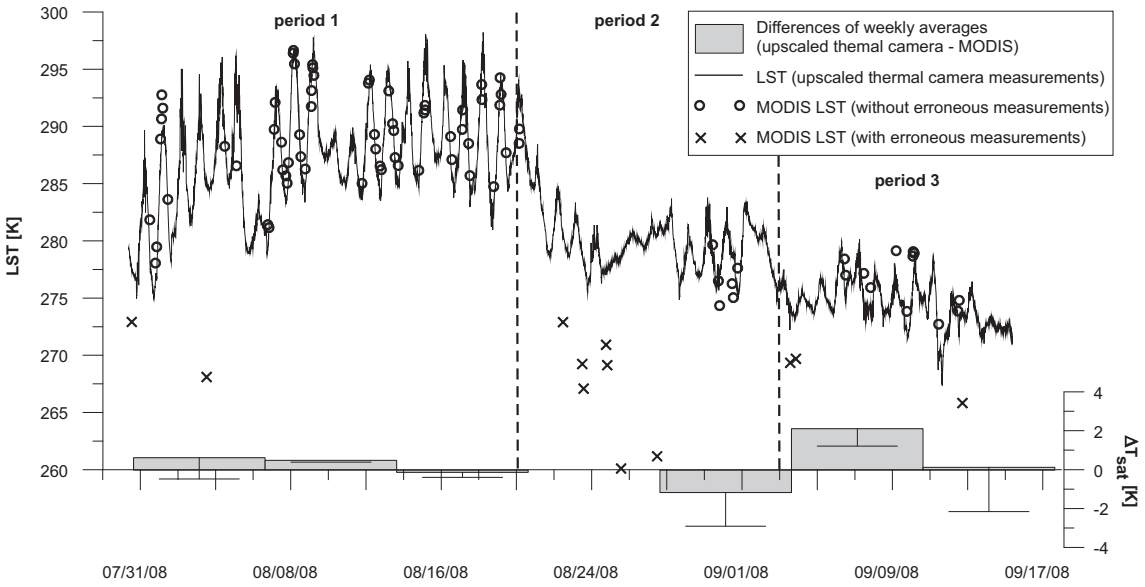

Figure 2.9: Land surface temperature (LST), as observed by the thermal camera and MODIS sensor (erroneous data are marked). The differences between the weekly averages of the thermal camera and the satellite data ΔT_{sat} are low for the first weeks, where the data density is high. The satellite LST averages are strongly bias, where the data density is sparse and the erroneous measurements induce additional temperature offsets (error bars).

to terrestrial observations (Fig. 2.9). In period (1) the average measurement density of three successful satellite observations per day is high due to prevailing clear sky conditions. Only two erroneous measurements are observed at the beginning of the period. During period (2), which is dominated by overcast conditions, few successful satellite observations are obtained, exclusively during short periods of clear sky conditions. The achieved average measurement density is 0.6 per day. Most of the data received during this period must be considered as erroneous. Period (3) is characterized by frequent clear sky conditions, resulting in a number of successful satellite measurements without erroneous data. The average measurement density during period (3) is one per day.

We now compare the weekly averages of the available satellite data with the true averages obtained by the thermal camera. The weekly surface temperature values are based on step wise averaging, using previous averages with hourly and daily intervals, in order to avoid the overrepresentation of clumped satellite data. The differences between the weekly averages of the upscaled thermal camera data and the MODIS product with and without erroneous data are illustrated in Fig. 2.9. The erroneous measurements of the satellite data set lead to a strong additional bias of the average values, especially when the data density is sparse. The following evaluation is conducted under the assumption that a reliable cloud cover mask is provided in order to separate the effect of erroneous data from the effect of the unequally spaced satellite time series on the average temperature values. In period (1), the satellite

averages are in very good agreement with the terrestrial observations due to the high data density. During the beginning of period (2) average values can not be calculated, since no measurements other than erroneous observations are available. At the end of period (2) satellite data are predominately available during the night and the late afternoon, which results in an underestimated average surface temperature. During period (3) satellite data are frequently obtained near local noontime, which leads to an overestimated average value. Hence, the averaging procedure fails under conditions with low measurement density and a systematic overrepresentation of certain daytimes.

2.6 Discussion

On time scales longer than the diurnal cycle, the results of this study show that the surface temperature variations, except for free water surfaces, average out. Hence, our results imply that permafrost temperatures in the polygonal tundra are not affected by spatial surface temperature differences due to heterogeneities of surface soil moisture. Sustained differences in surface temperature occur at free water bodies, such as the examined polygonal pond, which shows a surface temperature offset of 2.5 K in the weekly average during period (1). The observed surface temperature differences between the pond and the tundra surface are most likely the result of a distinctly different energy partition at free water bodies induced by efficient energy storage due to convective heat transport and absorption of solar radiation in the water column or at the ground. The effect of energy balance differences of lakes on regional arctic climates has been shown in measurements by Rouse et al. (2005) and simulations by Krinner (2003), Gutowski Jr et al. (2007) and **?**, who demonstrate the significantly different energy exchange processes at high latitude lakes compared to the surrounding soil surface. It can be expected that larger fractions of water bodies within the spatial averaging area induce significant temperature offsets.

Assuming that the results of this study can be transferred to other arctic wet tundra regions, unresolved spatial surface temperature heterogeneities are not a limitation for permafrost monitoring schemes based on remote sensing LST measurements. Temporal averages of satellite LST measurements are valid for the covered surface area, even so landscape heterogeneities are not resolved by the sensor, as long as the fraction of free water surfaces is small. This has been implicitely assumed in the permafrost monitoring schemes by Hachem et al. (2008) and Marchenko et al. (2009). Hence, LST products such as MODIS L2 with a spatial resolution of about 1 km^2 are applicable for permafrost monitoring schemes. However, such schemes require accurate temporal LST averages, which are necessarily based upon accurate measurements in appropriate temporal density. Due to these requirements three major problems are identified for the development of satellite based permafrost monitoring schemes:

1. The temporal resolution of the satellite time series is strongly affected by cloud cover, which leads to clustered time series, where averaging is problematic. Hence, reliable

gap filling methods must be developed. Possible gap filling procedures are demonstrated by Hachem et al. (2008), other approaches might be based on reanalysis products.

2. The existing cloud cover detection of satellite products such as MODIS must be improved, since unidentifiable measurement errors result in strongly biased average temperatures, especially when data are sparse. In the present state, this problem would make reliable gap filling methods more difficult or even impossible.

3. For satellite pixels with a high fraction of free water surfaces, a biased temperature record for the land area is likely. Further work on the effect of water bodies, such as polygonal ponds and thermokarst lakes, on the larger-scale surface temperature and energy balance is desirable for the implementation of LST products in future schemes of permafrost monitoring in wet tundra landscapes.

Although the results show that spatial temperature differences vanish on longer time scales, they are important for atmospheric energy exchange processes acting on much shorter time scales. The observed short term spatial surface temperature differences are mainly controlled by the by net radiation. Under clear sky conditions and strong radiative forcing, the temperature differences between wet and dry locations can be on the order of 4 to 6 K and exceed 12 K between open water bodies and dry surfaces. The temperature variations indicate distinctly different surface energy budgets, which can be caused by differences in albedo, energy storage in the ground, aerodynamic resistance or resistance to evapotranspiration. The surface temperature differences at wet and dry locations lead to distinctly different sources of sensible heat fluxes in immediate vicinity of each other. Furthermore, the differences in surface soil moisture most likely result in different evapotranspiration rates and thus latent heat fluxes. Due to the small distance between the sensible and latent heat flux sources, energy reallocation processes are possible, which could affect the energy balance on a larger scale (e.g. Guo and Schuepp 1994, Mahrt et al. 1994, Neumann and Marsh 1998). A better understanding of the relation between these small-scale processes and the larger-scale boundary layer dynamics, which are the result of accumulated local energy exchange processes, would enhance the process knowledge of the landscape specific climate dynamics in wet tundra regions.

2.7 Summary and Conclusion

The spatial and temporal characteristics of summer surface temperatures of a heterogeneous polygonal tundra landscape are investigated using ground based high resolution thermal infrared measurements. The measurements are used for ground-truthing a MODIS LST product. The following conclusions are drawn with respect to future satellite permafrost monitoring schemes:

- The spatial surface temperature variations at the wet polygonal tundra greatly reduce for averaging periods longer than the diurnal cycle. This has strong implications for

satellite based permafrost monitoring schemes, since the validity of surface temperature averages is not affected by unresolved landscape heterogeneities, except for free water bodies.

- Free water bodies show sustained differences in surface temperature to the remaining tundra surface. Hence, high resolution land-water masks are essential for the interpretation of satellite LST products, since unresolved water bodies can bias the satellite observations, if a high fraction occurs in the satellite footprint area.
- The success rate of MODIS LST data acquisition is limited due a frequent cloud cover, which is typical for arctic regions. Reliable surface temperature averages therefore require the development of gap filling procedures. Furthermore, the satellite data are biased by occasional erroneous measurements, which are caused by an incorrect cloud cover mask. This limitation should be overcome to enhance the data quality of the LST product.

Satellite based LST measurements bear great potential as a basic input parameter for a monitoring scheme of the thermal state of permafrost soils. However, continued effort will be required to overcome the mentioned limitations, if such monitoring schemes are intended to be applied on large scales.

2.8 Acknowledgements

We thank the following for their assistance in the field, technical support and for discussion: Niko Bornemann, Maren Grüber, Sina Muster and Konstanze Piel. Thanks to the logistical support of the Russian-German research station on Samoylov that made this study possible. We gratefully acknowledge the financial support by the Helmholtz Association (HGF) through a grant (VH-NG 203) awarded to Julia Boike.

Chapter 3

Paper II
Permafrost and surface energy balance of a polygonal tundra site in northern Siberia - Part I: Spring to fall

3.1 Abstract

Permafrost thawing is essentially determined by the surface energy balance, which potentially triggers the activation of a massive carbon source, if previously frozen organic soils are exposed to microbial decomposition. In this article, we present the first part of a comprehensive annual surface energy balance study performed at a polygonal tundra landscape in northeast Siberia, realized between spring 2007 and winter 2009. This part of the study focuses on the half year period from April to September 2007-2008, during which the surface energy balance is obtained from independent measurements of the radiation budget, the turbulent heat fluxes and the ground heat flux at several sites. The short-wave radiation is the dominant factor in the surface energy balance during the entire observation period. About 50% of the available net radiation is consumed by latent heat flux, while the sensible and the ground heat flux are both on the order of 20 to 30%. The ground heat flux is mainly consumed by active layer thawing, where 60% of soil energy storage are attributed to. The remainder is used for soil warming down to a depth of 15 m. The controlling factors for the surface energy partitioning are in particular the snow cover, the cloud cover and the soil temperature gradient. Significant surface temperature differences of the heterogeneous landscape indicate spatial variabilities of sensible and latent heat fluxes, which are verified by measurements at different locations. However, differences in the partition between sensible and latent heat flux for the different sites only exist during conditions of high radiative forcing, which only occur occasionally.

3.2 Introduction

The thermal state of permafrost and its susceptibility towards degradation is fundamentally determined by the surface energy balance. Recent studies revealed that essential climate changes take place in the Arctic and are expected to proceed in the future (Overpeck

et al. 1997, Hansen et al. 2001, Comiso 2006, Overland et al. 2008). There is observational evidence that energy and water exchange processes in the arctic landscapes are already substantially affected, which also involves the thermal state of permafrost (Serreze et al. 2000, Hinzman et al. 2005). Permafrost, which occupies about 25% of the land area of the Northern Hemisphere (Brown et al. 1997), is considered an important factor in the complex feedback mechanisms of the climate system due to its massive carbon storage capabilities (Christensen and Cox 1995, Callaghan et al. 2004, McGuire et al. 2006). Zimov et al. (2006) estimated that about 970 Gt of carbon are stored in permafrost soils worldwide, which is about twice the amount of the actual atmospheric carbon concentration. Until now it is unclear whether permafrost regions will turn into massive sources of greenhouse gases, such as methane and carbon dioxide, as the frozen soils begin to thaw (Hobbie et al. 2000, Davidson and Janssens 2006). This raises the question about the amount of stored organic material that will be exposed to microbial decomposition as a result of permafrost degradation and progressing thaw depths under a warming climate. Recent measurements in wet tundra landscapes demonstrate the importance of the freeze and thaw dynamics for methane emission, which are related in a non-linear manner (Christensen et al. 2003, Sachs et al. 2008, Mastepanov et al. 2008). For this purpose, efforts have been initiated to incorporate permafrost and the annual freeze and thaw dynamics in global climate models (e.g. Stendel and Christensen 2002, Lawrence and Slater 2005, Nicolsky et al. 2007, Lawrence et al. 2008). However, the energy exchange processes at the soil-atmosphere interface strongly depend on the landscape characteristics, such as surface moisture, vegetation cover, snow cover and soil properties. These characteristics are incorporated in climate models as parameterizations of e.g. surface roughness, resistance to evaporation and thermal properties of soil or snow. The representation of permafrost in climate models therefore essentially depends on the parameterization that is used to describe the surface energy balance. To support and validate modeling, it is desirable to obtain process studies, which deliver important information about the landscape specific energy balance characteristics and their determining factors. Long-term energy balance studies are especially important in arctic regions, where the surface energy budget is characterized by an extreme seasonality and where meteorological measurements are sparse (Westermann et al. 2009).

This study presents the annual energy balance of a wet tundra landscape in northern Siberia from spring 2007 until winter 2009. The study has been performed at a site dominated by polygonal tundra, which constitutes a typical permafrost landscape (Zhang et al. 2008). Based on standard meteorological measurements Boike et al. (2008) contrasts the energy and water balances of a wet and a dry summer at the study site. In this study, we extend this previous work over the entire annual cycle by using independent measurements of all components of the surface energy balance. Furthermore, we investigate the impact of the considerable surface heterogeneity of the wet tundra landscape on the regional energy balance. The results of this study are presented in two parts: Part I comprises the period from April to September, which is characterized by increasing soil temperatures at the study site. Part II focuses on the winter period from October to March, which represents the period of soil cooling (Langer et al. 2010b).

The aim of the study is (i) to evaluate the annual surface energy balance at the study site,

(ii) to determine the controlling and limiting factors in the energy partitioning and the transport processes, (iii) to evaluate the seasonal and inter-annual variability and (iv) to elucidate the impact of surface heterogeneities on the energy balance at the landscape scale.

3.3 Study site

The study site is located on Samoylov Island (72° 22' N; 126° 30' E) at the upper part of the Lena River Delta (Fig. 3.1). It is characterized by a wet tundra landscape typical of northern Siberia. Samoylov Island covers an area of about 4.5 km^2 with an elevated eastern terrace and a lower western flood plain. The region features a typical arctic-continental climate with a mean annual air temperature (MAAT) of about −13 °C and a total annual precipitation around 250 mm (Boike et al. 2008). The ice break-up of the Lena River and the snow melt usually start at beginning of June. The snow-free period lasts until the end of September, during which maximum air temperatures of about 20 °C are reached. The regional climate and the synoptic conditions are influenced by both the Siberian High and the Polar Low pressure system. During the summer period, intermediate cyclone activity with low intensity are typically observed, while cyclones with high intensity, but short lifetime are more frequent in winter (Zhang et al. 2004). However, the strong Siberian High strongly affects the Lena Delta region during the winter months and causes air temperatures to fall frequently below −45 °C. The study site is in the zone of continuous permafrost, with permafrost depths reaching 500 to 600 m in the wider area around the study site (Grigoriev 1960). The soil temperatures are very low: in the depth of the zero annual amplitude (approximately 15 m), the soil temperatures are about −10 °C. The maximum thaw depths during summer range from 0.40 to 0.50 m. The permafrost landscape features characteristic polygonal surface structures, which are typical for the wet tundra landscapes. These patterns are 50 to 100 m^2 large and usually consist of dry elevated rims and depressed centers, which are filled with water-saturated peat soils or shallow ponds. The vegetation at the wet centers is dominated by hydrophilic sedges and mosses, while the elevated dry rims are dominated by mesophytic dwarf shrubs, forbs and mosses. For a more detailed description of the vegetation and landscape characteristics, refer to Are and Reimnitz (2000), Kutzbach et al. (2004), Kutzbach et al. (2007), Boike et al. (2008) and Sachs et al. (2008).

3.4 Methods

The energy balance equation is written as

$$Q_{\text{net}} = Q_H + Q_E + Q_G + [Q_{\text{melt}}] + C, \tag{3.1}$$

where Q_{net} denotes the net radiation, Q_H the atmospheric sensible heat flux, Q_E the atmospheric latent heat flux, Q_G the ground heat flux, Q_{melt} is the energy flux consumed by the snow melt, which can be inferred from to the energy required to thaw the snow pack, E_{melt}, and the duration of the melt period. As independent field measurements of the components are subject to errors, a residual of the energy balance or closure term C can

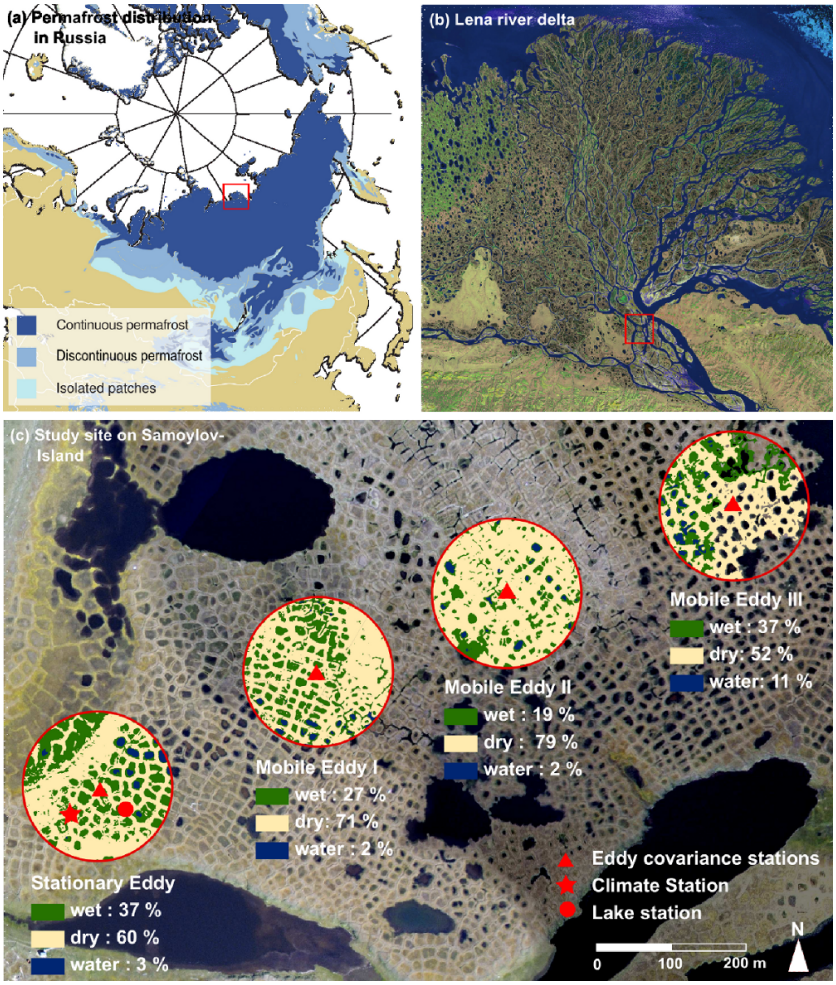

Figure 3.1: (a) Permafrost distribution in Siberia (Brown et al. 1997); the location of the Lena River delta is marked in red. (b) Satellite image of the Lena River delta obtained from the Landsat Thematic Mapper (USGS 2000); the location of Samoylov Island is marked in red. (c) High-resolution aerial image of the study site on Samoylov Island, where the considerable small-scale heterogeneity of the surface cover is visible. The locations of all installations are marked, the approximate footprint areas of the eddy covariance systems are indicated in red. The fractions of wet, dry and water surfaces in the concerning foot print areas are calculated using the foot print model of Schmid (1994).

remain. The measurement setup and the expected margins of error are described in detail in the following paragraphs.

3.4.1 The Radiation balance

The net radiation budget is the most essential term in the surface energy balance and can be written as

$$Q_{\text{net}} = Q_{S\downarrow} - Q_{S\uparrow} + Q_{L\downarrow} - Q_{L\uparrow}\,, \tag{3.2}$$

where $Q_{S\downarrow}$ and $Q_{S\uparrow}$ are the incoming and outgoing short-wave components and $Q_{L\downarrow}$ and $Q_{L\uparrow}$ the incoming and outgoing long-wave components, respectively. Using the surface albedo α and Stefan-Boltzmann law, the radiation balance can also be rewritten as

$$Q_{\text{net}} = Q_{S\downarrow}(1-\alpha) + \epsilon Q_{L\downarrow} - \epsilon\sigma T_{\text{surf}}^4, \tag{3.3}$$

where ϵ is the surface emissivity, T_{surf} the surface temperature and σ is the Stefan-Boltzmann constant. In the present study, a variety of sensors is used to determine the radiation components. The net radiation Q_{net} is measured with the NR-Lite (Kipp & Zonen, Netherlands) net radiation sensors mounted in 1.5 m height. Additional net radiation measurements (CNR1, Kipp & Zonen, Netherlands) with higher accuracy are available during mid summer 2007 and for the entire observation period of 2008. The CNR1 four component sensor separately measures all radiation balance components. The sensor is located in the vicinity of the eddy-covariance station and is mounted on a 2 m mast (Fig. 3.1). Further net radiation measurements with an NR-Lite sensor are conducted at a thermokarst pond, which is approximately 0.8 m deep. These additional measurements are performed to investigate differences in the radiation balance between the tundra surface and shallow water bodies, which are a frequent landscape element (Fig.3.1). The evaluation of the accuracy of the employed net radiation sensors is difficult, since World Meteorological Organization (WMO) quality standards are not available for net radiation sensors. Studies comparing the employed sensors with high-accuracy single component sensors (Brotzge and Duchon 2000, Kohsiek et al. 2007) suggest a relative measurement accuracy of about 20% for the NR-Lite and about 10% for the CNR1 sensor. A sensor comparison under field conditions shows that daily averages of the NR-Lite sensor are about 5 to 10 W m^{-2} lower compared to the values obtained by the four component sensor. This bias is in most cases within the assumed error margins, but becomes significant under conditions of low net radiation. In addition to the net radiation sensors, measurements of the upwelling thermal radiation (CG1, Kipp & Zonen, Netherlands) are available at the standard climate tower (Fig. 3.1), while spatial differences are measured with distributed infrared surface temperature sensors (IRTS-P, Apogee Instruments, USA). The infrared sensors are mounted on small tripods about 0.8 m above the surface and are placed above different tundra soils. According to instrument specifications, the IRTS-P sensors deliver surface temperatures with an accuracy of about 0.5 °C, from which we infer the upwelling thermal radiation following Stefan-Boltzmann law (compare Eq. 3.3). We assume emissivities ϵ of 0.98 for wet and 0.96 for dry tundra surfaces

(Langer et al. 2010c). In order to obtain a more differentiated picture of the short-wave radiation balance, spatially distributed albedo measurements are conducted with a mobile short-wave radiation sensor. The albedo measurements are conduced during solar noon under clear-sky conditions to obtain a maximum accuracy.

3.4.2 Turbulent heat fluxes

The turbulent fluxes of momentum, u_*^2, sensible heat, Q_H and latent heat, Q_E, are determined with the eddy covariance method. The applied eddy covariance system consists of a Campbell C-SAT 3D sonic anemometer and open path LICOR LI-7500 CO_2 and H_2O gas analyzer mounted on a 2.4 m mast. The data are sampled at a rate of 20 Hz using a Campbell CR3000 data logger. Sonic anemometer measurements are conducted during the entire observation period, while the gas analyzer is operated only during the field campaigns, when a reliable power supply and regular maintenance can be accomplished. The eddy-covariance method is based on high-frequency measurements of the sonic temperature T_s, the specific humidity q, the horizontal and vertical wind speed components u and w. Using Reynolds decomposition, the turbulent flux components can be evaluated from the covariances $\overline{u'w'}$, $\overline{T_s'w'}$ and $\overline{q'w'}$ of the fluctuations u', w', T_s' and q' around the average values of the above quantities as

$$u_*^2 = \overline{u'w'}, \tag{3.4}$$

$$Q_{HB} = \rho_{\text{air}}\, c_p\, \overline{T_s'w'}, \tag{3.5}$$

$$Q_H = \rho_{\text{air}}\, c_p\, \overline{T'w'} = \rho_{\text{air}}\, c_p\, (\overline{T_s'w'} - 0.51\, \overline{T}\, \overline{q'w'}), \tag{3.6}$$

$$Q_E = \rho_{\text{air}}\, L_{lg}\, \overline{q'w'}, \tag{3.7}$$

where Q_{HB} denotes the buoyancy flux, c_p the specific heat capacity of air at constant pressure and L_{lg} the specific latent heat of vaporization of water. Note that in the case of measurements over a frozen (snow) surface, L_{lg} must be replaced by the latent heat of sublimation L_{sg}. The buoyancy flux Q_{HB} differs from the true sensible heat flux Q_H due to the difference between the measured sonic and the real air temperature $T_s = T\,(1 + 0.51q)$. Hence, the covariance $\overline{T'w'}$ must be corrected according to Eq. 3.6, if measurements of the specific humidity q are available (Schotanus et al. 1983). As the LICOR gas analyzer is not operated continuously (see above), this correction cannot be applied during parts of the spring and summer period in 2007. The error induced by interpreting the buoyancy flux as sensible heat flux can be estimated using the Bowen ratio, Q_H/Q_E. For Bowen ratios of approximately 0.5 and average air temperatures of $\overline{T} \approx 300$ K, the offset is on the order of 15%, which constitutes an additional error during the respective periods. The turbulent fluxes are calculated for 30 minute intervals with the internationally standardized

'QA/QC' software package 'TK2' (Mauder and Foken 2004, Mauder et al. 2007), which includes all 'state-of-the-art' corrections and tests. The quality assessment follows the scheme of Foken et al. (2004), which is based on tests for stationarity of the turbulence and the integral turbulence characteristic (ITC). In this study, the latter is not applied, since the quality criterion of the integral turbulence characteristic is not well defined in arctic region, where stable atmospheric stratification and intermittent turbulence are common (Lüers and Bareiss 2009). The stationarity criterion is considered to be sufficiently fulfilled (quality flags 1 and 2), if the average covariance inferred from 5 minute subintervals do not deviate more than 30% from the covariance value over the entire 30 minute interval (Foken et al. 2004). A graduation of the deviation is used as a quality measure, expressed with quality flags between 1 and 9. In this study, we accept sensible heat fluxes, if both the quality flags of $\overline{u'w'}$ and $\overline{T_s'w'}$ feature quality values of 6 or better. For the latent heat fluxes Q_E, we use the quality flags of $\overline{u'w'}$ and $\overline{q'w'}$, respectively. This quality standard is recommended for long-term observations (Foken and Wichura 1996). In other field experiments, this quality level is found to be associated with a relative measurement accuracy of about 15% (Mauder et al. 2006), which we assume as the general accuracy of the obtained turbulent heat fluxes. The quality assessment causes a data reduction of about 3% for the sensible and about 4% for the latent heat fluxes. A further data reduction of about 14% originates from the exclusion of the wind sector between 263°to 277°, which is considered to be the lee area of the measurement setup. In order to obtain the magnitude of the latent heat fluxes, when measurements of the LICOR gas analyzer are not available, we use a model approach based on the parametrization of turbulent fluxes introduced by Høgstrøm (1988). The required parameters, such as roughness lengths and surface resistance to evaporation, are determined by model optimization to available measurements. A detailed description of the used model is given in Appendix 3.8.3. An overview of the available dataset is given in Tab. 3.2, where the modeled latent heat fluxes are marked.

Large-scale differences in the distribution of wet and dry tundra patches as well as shallow ponds potentially create differences in the turbulent heat fluxes on the landscape scale. It is therefore unclear whether the turbulent heat fluxes obtained at a single location are representative on the landscape scale. The impact of such surface heterogeneities on the turbulent heat flux characteristics is evaluated by a second eddy covariance system during the summer of 2008. The second system is identical to the first one and is used as a mobile station, which is moved in a weekly interval along a 1 km east-west transect across the study site (Fig. 3.1) while the first system provides simultaneous measurements at the reference location. The flux source area of each half-hour value is determined with the footprint model of Schmid (1994). For the footprint calculations, we assume a constant roughness length $z_0 = 10^{-3}$ m, which we directly infer from the turbulence measurements under neutral atmospheric stratification (Foken 2008). This value is consistent with typical roughness lengths reported for short grassland (Oke 1987, Foken 2008). The fractions of wet and dry tundra areas as well as polygonal ponds for eddy footprint areas are derived from aerial photographs using supervised classification based on field mapping. The locations of the stationary and the mobile eddy system feature differences in average surface soil moisture according to differences in the polygonal structures. The blending height l_b

Table 3.1: Used soil and snow parameters for ground heat flux calculations. Values of porosity P_{dry} and water content θ_w are inferred from soil sample analysis and in situ soil water content measurements. The heat capacities are calculated by weighting $C_{h,w}$ and $C_{h,s}$ according to water content and porosity. The thermal diffusivities D_h are determined with the conductive method (see Sect. 3.4.3), from which we obtain the thermal conductivities K_h in conjunction with the assumed heat capacity. Errors are calculated using Gaussian error propagation.

Substrate	P_{dry}	θ_w	C_h [MJ m^{-3}K^{-1}]	D_h [m^2 s^{-1}]	K_h [W m^{-1} K^{-1}]
dry peat	0.8 ± 0.1	0.1 ± 0.1	0.9 ± 0.5	0.16 ± 0.01	0.14 ± 0.08
wet peat	0.8 ± 0.1	0.7 ± 0.1	3.4 ± 0.5	0.19 ± 0.04	0.6 ± 0.17
saturated peat	0.8 ± 0.1	0.8 ± 0.1	3.8 ± 0.2	0.19 ± 0.02	0.72 ± 0.08
snow	$\rho_{\mathrm{snow}} = 190 \pm 10\,\mathrm{kg\,m^{-3}}$		0.40 ± 0.04	0.54 ± 0.04	0.22 ± 0.03

can be approximated by $l_b \approx L_x/200$ (Garratt 1994), where L_x is the horizontal scale of heterogeneity. With an approximate size of 20 m of the polygonal surface elements, the measurement height of 2.4 m is well above the blending height, so that the obtained flux values can be considered a spatial average of the footprint areas.

3.4.3 Ground heat flux

The ground heat flux is essential for permafrost, since it determines the annual active layer dynamics as well as the long-term thermal stability of the permanently frozen ground. In this study we apply two different methods to determine the ground heat flux on different time scales.

Calorimetric method

The calorimetric method is used to evaluate the average ground heat flux over longer periods (Appendix 3.8.1). The method is based on soil temperature and moisture measurements and calculates the average ground heat flux from changes in the sensible and latent heat content of a soil column. The method has been successfully applied in several permafrost regions and is described e.g. by Boike et al. (1998) and Westermann et al. (2009). We use a measurement setup consisting of an active layer temperature and moisture profile to a depth of 0.5 m, which features 5 thermistors (107-L, Campbell Scientific, USA) and 5 Time-Domain-Reflectometry (TDR) soil moisture probes (CS610-L, Campbell Scientific, USA). The calorimetric methods requires temperature measurements to a depth, where no temperature changes occur in the considered time interval (Appendix 3.8.1). The temperature profile to the depth of zero annual amplitude (15 m) are measured in a 26 m bore-hole with a temperature chain featuring 24 thermistors (XR-420, RBR Ltd., Canada).

Conductive method

The conductive method is primarily used to evaluated the diurnal course of the ground heat flux through the upper most ground surface Westermann et al. (2009). Depending on the surface conditions, the ground surface is either defined as the soil or the snow surface. This

method directly calculates the heat flux through the soil surface by solving the differential equation of conductive heat transport (Appendix 3.8.2), which involves the determination of the thermal conductivity of the soil using shallow temperature profile measurements. As the conductive method is not feasible during periods, when a phase change of water occurs, we exclude the transition periods in spring and fall from such calculations. The employed temperature profiles are installed between the surface and about 30 cm depth in different soil substrates, and consist of at least three thermocouples or thermistors with accuracies better than 0.2 K. The instrumented soil substrates are classified as dry, wet and saturated peat soils (Tab. 3.1). The sensors of each profile are placed in soil layers considered to be homogeneous in composition according to visual examination. Furthermore, we assume constant thermal properties over the considered time intervals (Appendix 3.8.2), which is a good assumption for saturated and super-saturated soils.
During early spring, the heat flux through the snow cover can be calculated using a similar approach. The determination of the snow thermal properties is based in measurements of the snow density and of temperature profiles in the snow conducted in spring 2008. The boundary conditions for the heat flux calculations are obtained from a infrared surface temperature sensor and a thermistor located at the soil-snow interface. Snow heat fluxes are calculated for periods of constant snow depth, which is measured with a ultrasonic ranging sensor (SR50, Campbell Scientific, USA) located next to the measurement setup. The obtained snow heat fluxes must be considered a rough approximation, since the assumption of constant thermal snow properties may be violated in reality (e.g. Sturm et al. 1997, Zhang 2005).

Soil and snow parameters

Both methods of ground heat flux calculations require knowledge about the thermal properties of soil or snow (compare Appendix 3.8.1, 3.8.2). The heat capacity is an essential parameter, which we infer from soil component analyses of soil samples taken during the field campaigns and in situ water content measurements. We assume an error of 10% on each soil fraction, such as water content, ice content and solid soil matrix. A bulk heat capacity of 2.3 ± 0.3 $\mathrm{MJm^{-3}K^{-1}}$ is used for the solid soil fraction. The obtained soil properties and the associated heat capacities are depicted in Tab. 3.1. It is evident, that large uncertainties in heat capacity occur at the dry peat soils, since already small variations in the soil composition induce errors of about 60%. As a consequence, we do not evaluate soil heat fluxes at dry locations. The conductive method allows to determine further soil properties, such as the thermal diffusivity and the heat conductivity (Appendix 3.8.2), which are displayed in Tab. 3.1. For wet tundra soils, the obtained diffusivity values show variations in the range of 20%, which results in a combined error of about 30% for the heat conductivity. A similar error range is calculated for the snow heat conductivity, which we infer from snow density and snow temperature profile measurements using the conductive method (see Appendix 3.8.2). For simplicity, we assume an error of 30% as appropriate for all ground heat flux calculations, which is about 10% larger than the errors assumed for the other energy balance components.

3.4.4 Ancillary measurements

Measurements of air temperature and relative humidity (MP-100, Rotronic, Switzerland) are performed at the standard climate tower in the vicinity of the eddy covariance system (Fig. 3.1). The snow melt during spring is evaluated based on ultrasonic ranging sensors (SR50, Campbell Scientific, USA) located at the standard climate station and the polygonal pond. In addition, we approximate the evolution of snow free areas during the ablation period by automatic daily photographs of the measurement site. The latent heat content of the snow cover E_{melt} is inferred from spatially distributed measurements of the snow-water equivalent immediately before the onset of snow melt in 2008. With an almost identical snow depth, a similar snow-water equivalent is assumed for 2007.

3.5 Results

3.5.1 Seasonal energy balance characteristics

The time span considered in this study ranges from April until September of the years 2007 and 2008. For the description of the seasonal energy balance characteristics, we separate the observation period into three subsections according to the specific seasonal climate conditions. The segmentation of the observation period follows broad synoptic changes, such as the presence of snow, the general air temperature evolution and the occurrence of frost events. While the resulting segmentation is unequally spaced, we provide an equally spaced overview over the seasonal energy balance in Fig. 3.5. In the following paragraphs, we also examine inter-annual differences in the surface energy balance.

Spring (1 April - 31 Mai)

During the spring period, the daily average air temperatures increase strongly from $-16\,^{\circ}\mathrm{C}$ to $6\,^{\circ}\mathrm{C}$ in 2007 and from $-25\,^{\circ}\mathrm{C}$ to $2\,^{\circ}\mathrm{C}$ in 2008, with notable differences between both years. The increasing temperatures are accompanied by steadily increasing short-wave radiation after the end of the polar night and the shrinking snow cover towards the end of the period. According to the ultrasonic snow depth sensor, the early spring snow depths are in the range from 0.30 and 0.35 m in both years. These point values are confirmed by spatially distributed snow water equivalent measurements in 2008, which yield an average snow depth of about 0.30 m with an average snow density of 190 $\mathrm{kg\,m^{-3}}$. The onset and course of the snow melt are almost identical for both years. While the snow melt starts in the mid of May shortly after the beginning of the polar day, it typically does not occur in a single event, but is interrupted by declining air temperatures and subsequent snowfall. The first snow melt event last only a few days (10-19 May 2007 / 10-14 May 2008), during which the elevated polygonal rims become partly snow-free (Fig. 3.2). The subsequent snow fall delivers only a few centimeters of additional snow cover, which disappear quickly in the second and final melt event (22-30 May 2007 / 21-29 May 2008). In the following, we refer to the period before the onset of melting as the pre-melt period, while the subsequent time is denoted the snow melt period. The average radiation budget is positive

Table 3.2: Average heat fluxes and essential climate parameters. Values are in W m^{-2} , if not indicated differently. Turbulent heat flux values marked in bold are affected by minor data gaps, due to quality or lee sector data exclusion. Radiation values measured with the NR-Lite sensor are marked with $^{\ominus}$, and values obtained with the four component sensor (CNR1) are indicated with $^{\oplus}$. Modeled values of latent heat flux are indicated with ‡. The springtime precipitation is replaced by the snow water equivalent (SWE).

	Spring		**Summer**		**Fall**	
	2007	2008	2007	2008	2007	2008
	04/28-05/31	04/22-05/31	07/12-08/23	06/07-07/08 07/29-08/30	09/01-09/30	09/01-09/30
Q_{net}	$44^{\ominus}$	$27^{\oplus}$	$81^{\oplus}$	$104^{\oplus}$	$7^{\ominus}$	$11^{\oplus}$ $5^{\ominus}$
ΔQ_S	-	61	119	145	-	-
ΔQ_L	-	-34	-38	-41	-	-
Q_H	**8.7**	**1.3**	14	22	-1.5	-4.4
Q_E	**12**‡	**9.7**	40	44	**15**‡	**19**
$Q_{G,\text{net}}$	18	14	15	22	6	0.5
$Q_{G,\text{sensible}}$	17	13	5	9	6	4
$Q_{G,\text{latent}}$	1	1	10	11	0	-3.5
E_{melt} [MJm^{-2}]	19	19	-	-	-	-
C	**-1.7**	**-3**	12	18	**-12.5**	**-10.1**
T_{surf} [°C]	-3.8	-6.9	10.5	9.2	3	1.2
T_{air} [°C]	-4.7	-6.9	9.2	8.2	2.6	1.6
R_H [%]	84	84	84	84	88	87
P [mm]	SWE: 60	SWE: 57	58	100	49	21

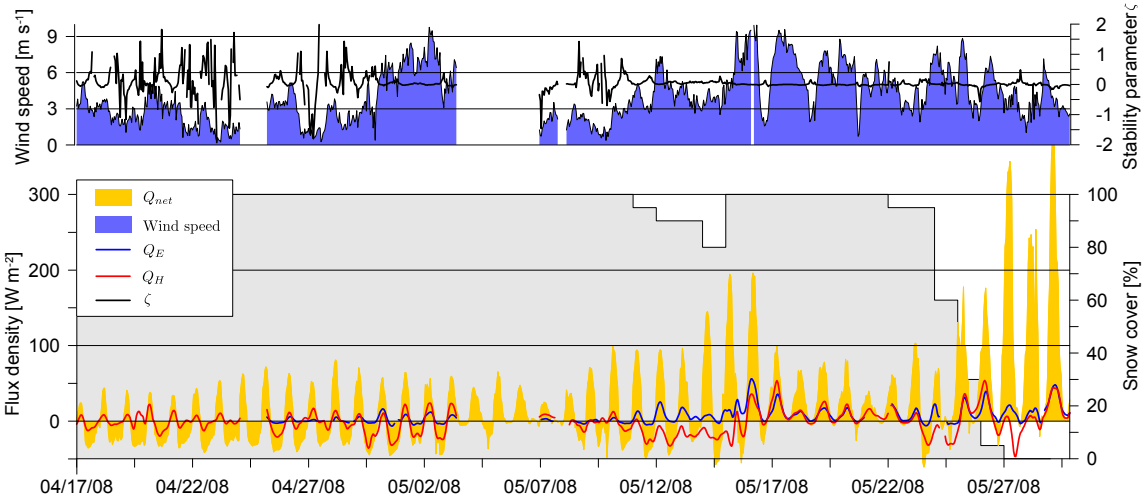

Figure 3.2: Net radiation, sensible heat flux, latent heat flux, wind speed, atmospheric stability parameter $\zeta = z/L_*$ and approximate fraction of the snow-covered area (in gray) during spring 2008. The energy balance is strongly related to the evolution of the snow melt. The wind speed is significantly increased during the melt period and the atmospheric stratification is essentially neutral. Varying atmospheric conditions are observed in the pre-melt period.

during the entire spring period and of similar magnitude in both years (Fig. 3.5). Before the onset of snow melt, the diurnal cycle of the net radiation ranges from -40 to 50 W m^{-2}, but increases significantly after the snow cover has disappeared. This rapid change in the radiation budget is related to the drastic change of the surface albedo, which is about 0.8 before and 0.2 after snow melt. This change in the surface characteristics is reflected in all energy balance components, which we depict in Fig. 3.2. The turbulent sensible heat flux ranges from -30 to 20 W m^{-2} during the pre-melt period and basically follows the course of the surface radiation budget. About two days before the onset of snow melt, persistent negative sensible heat fluxes are observed, which appear to be partly decoupled from the net radiation budget (Fig. 3.2). The snow surface temperature approaches 0 °C around noon. This relation indicates that both the turbulent sensible heat fluxes as well as the incoming short-wave radiation contribute to the snow melt. As soon as snow free areas are present, the sensible heat flux rapidly exceeds values of 40 W m^{-2}. After the snow cover has disappeared entirely at the end of May, the sensible heat flux reaches peak values of 90 W m^{-2}. A similar evolution is observed for the latent heat flux, which is between 0 and 10 W m^{-2} before the onset of snow melt and quickly increases to values of 50 W m^{-2} during the first snow melt event. After the final melt period, the latent heat flux exceeds values of 100 W m^{-2} and features an average value of 35 W m^{-2} during the last ten spring days of 2008. This average heat flux corresponds to 30 MJm^{-2} or to 12 mm of evaporated water, respectively. As the snow water equivalent of 2008 amounts to approximately 57 mm, about 20% of the snow cover sublimate or evaporate during the last spring days. Hence, the snow cover effectively supplies 45 mm to the summer time water budget, which constitutes about 20% of the precipitable water of the entire observation period. Considering similar snow heights and the identical course of the ablation process, a similar magnitude of snow cover contribution to the water balance can be assumed in 2007.
The atmospheric stratification is reflected in the stability parameter ζ, which is essentially zero during neutral conditions, larger than zero for stable and smaller than zero for unstable atmospheric stratifications. During the pre-melt period, the atmospheric stratification changes frequently between stable and unstable conditions (Fig. 3.2). At this time, neutral stratifications occur occasionally in conjunction with wind speeds larger than 2 ms^{-1}. With the onset of snow melt, the wind speed is generally high and the atmospheric stratification becomes essentially neutral (Fig. 3.2). The average ground heat flux during the spring period is remarkably positive and dominated by storage of sensible heat in both years (Tab. 3.2), which is associated with a steady warming of the deeply frozen soil. A closer look at the evolution of the ground heat storage (Fig. 3.3) reveals a faster soil warming in early spring 2007. This difference in the evolution of the ground heat budget compared to 2008 is related to significantly warmer air and snow surface temperatures, but relatively cold soil temperatures in early spring 2007 (Tab. 3.2). In both years, the amplitude of the ground heat flux through the snow cover typically ranges from -20 and 20 W m^{-2} during the pre-melt period and is thus in the range of the turbulent sensible heat fluxes.

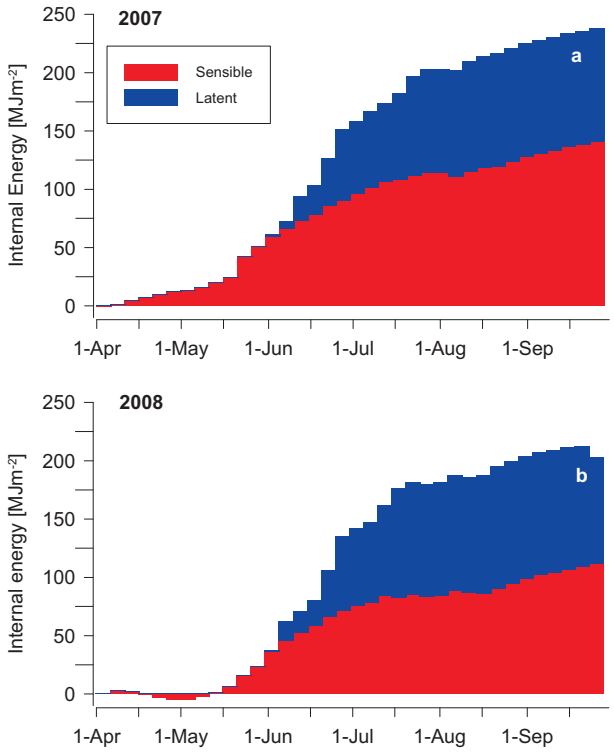

Figure 3.3: Internal energy of the soil over the entire observation period in a) 2007 and b) 2008. The soil temperatures of 2007 are colder in spring and the air temperatures are warmer, which explains the increased heat storage at the beginning of the period. Towards the end, the soil temperatures are almost equal.

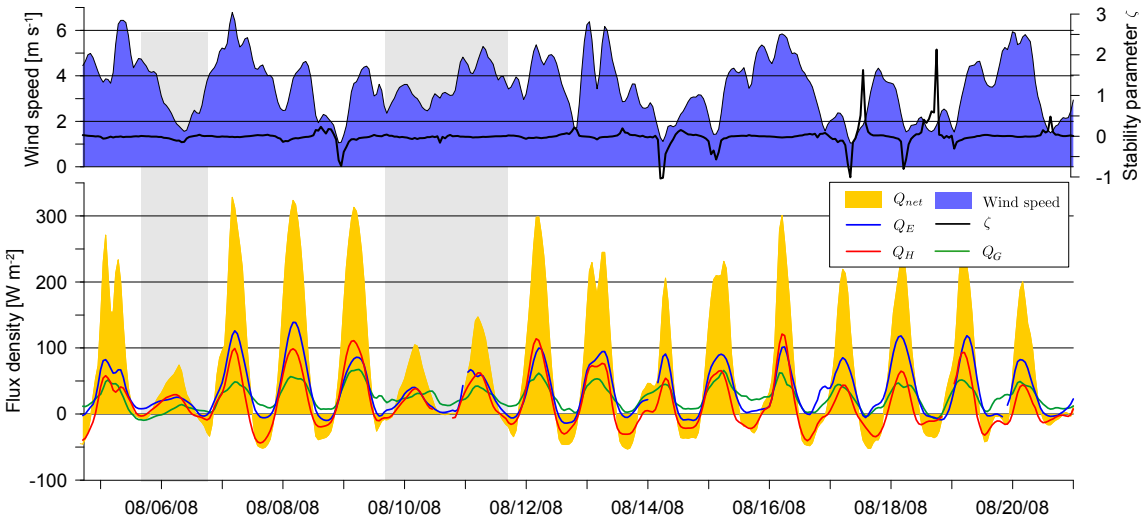

Figure 3.4: Exemplary heat fluxes, wind speed and stability parameter during late summer 2008, overcast periods are marked in gray.

Summer (01 June - 31 August)

The summer period is characterized by a strong short-wave radiative forcing, a snow-free surface, day time temperatures well above the freezing point and the thawing of the active layer (Fig. 3.5, Tab. 3.2). Polar day conditions last until August 7, featuring high values of incoming short-wave radiation. Daily averages of incoming short wave radiation frequently exceed values of 300 W m^{-2} under clear-sky conditions and can be as low as 20 W m^{-2} under overcast situations, which occur frequently. The reduced solar radiation during cloudy conditions is partly compensated by the thermal sky radiation, which is then significantly increased. The daily averages of incoming long-wave radiation typically ranges from 280 W m^{-2} for clear-sky and 380 W m^{-2} for cloudy situations. The daily averages of emitted long-wave radiation vary between 330 W m^{-2} and 420 W m^{-2}, which corresponds to average surface temperatures of 3 and 20 °C. Consequently, the net long-wave losses frequently exceed 100 W m^{-2} during clear-sky conditions, while they are almost zero during overcast situations. The average summer net radiation of 2007 is slightly higher compared to 2008 (Fig. 3.5), which is most likely caused by differences in cloudiness. This is also confirmed by the precipitation rates, which are doubled during the early summer period of 2008.

In both years, unstable stratifications ($\zeta < 0$) occur frequently during the day, but usually do not last longer than 12 hours. The nights are dominated by neutral stratifications ($\zeta \approx 0$), while stable atmospheric conditions ($\zeta > 0$) are only observed occasionally under calm conditions and highly negative values of the net radiation. The turbulent heat fluxes constitute dominant components in the summer time energy balance. About 20 to 30%

of the available radiative energy is consumed by turbulent sensible heat flux, while evapotranspiration amounts to about 40 to 50% (Fig. 3.5, Tab. 3.2). The turbulent heat fluxes show a strong diurnal cycle and frequently exceed values of 130 W m^{-2} for the sensible and 150 W m^{-2} for the latent heat flux during the day. During the night, significant negative sensible heat fluxes on the order of -20 W m^{-2} are observed, while negative latent heat fluxes (dew fall) occur only occasionally. Such events are then associated with a highly negative net radiation and low surfaces temperatures, as they occur at the end of the summer section. We depict an exemplary period during late summer 2008 in Fig. 3.4, which illustrates the typical diurnal cycle of the heat flux components forced by the incoming solar radiation. The wind speed appears to be associated with a diurnal pattern (Fig. 3.4), which indicates enhanced turbulent heat exchange during the day and lowered turbulence during the night. A dependence of the wind direction on the day time is not detected. For both years, the average Bowen ratio Q_H/Q_E is essentially below zero and indicates high rates of evapotranspiration. The amount of evaporated water is about 70 mm in 2007 and about 100 mm in 2008, which is about the same as the precipitation measured in the concerned sub-periods (Tab. 3.2).
When comparing the turbulent heat fluxes for the two years, it must be emphasized that the average flux values depicted in Tab. 3.2 are based on different sub-periods and are not directly comparable. For the inter-annual comparison, we make use of modeled latent heat flux values. The gap-filled energy balance with equally spaced averaging intervals is illustrated in Fig. 3.5. Inter-annual differences in the turbulent heat fluxes occur during the early and mid summer period, when the net radiation budget of 2008 is also affected by clouds. The reduced radiation budget results in generally decreased sensible heat fluxes, while the latent heat fluxes appear to be slightly increased during early summer 2008. In both years, the ground heat flux denotes a remarkable term in the summertime energy balance, which consumes about 20 to 25% of the available radiation budget. The ground heat flux is characterized by active layer thawing, which makes up 60% of the entire ground heat flux (Fig. 3.3). The remaining fraction is stored as sensible heat in the deeper soil. With a high soil water content of about 70%, a maximum thaw depth of only 0.40 m is reached during the summer period. The shallow thaw depth causes strong soil temperature gradients in the active layer, which enhance the ground heat flux. The ground heat flux shows a strong diurnal cycle and frequently exceeds values of 50 W m^{-2} during the day (Fig. 3.4), while negative ground heat fluxes are observed only occasionally during clear-sky nights.

Fall (1 September - 30 September)

We denote a short transition period as fall segment, which in both years is characterized by steadily decreasing air and surface temperatures, the onset of freezing and occasional snow fall, while a continuous snow cover does not form yet. In both years, the fall period starts with air and surface temperatures well above the freezing point and ends with temperatures around 0 °C. Only occasional freezing events are observed during the fall period 2007, while sustained freezing already occurs in 2008. The inter-annual difference in the temperature

evolution is reflected in the average air and surface temperatures, as well as in the ground heat fluxes (Tab. 3.2). In 2008, the entire active layer already approaches temperatures of 0 °C at September 17, but warms again for one week, before the soil temperatures finally reach the zero-curtain around September 25. In contrast, the soil temperature in 2007 never enters the zero-curtain during the fall period. Hence, the average ground heat flux in 2007 only indicates positive sensible heat storage (Tab. 3.2), which is caused by the delayed warming of soil in a depth of 1 to 10 m, which in 2008 is almost equal to the released latent heat from the initial freezing (Tab. 3.2). The average radiation budget is significantly reduced, but still positive in both years and features a distinct diurnal cycle with daytime values on the order of 100 W m^{-2}. A negative net radiation on the order of -50 W m^{-2} is frequently observed during the nights in 2008, which occurs only sporadically in 2007. Contrary to the summer segment, the reduced radiative losses during the nights and the significantly higher amount of precipitation indicate an increased cloudiness in fall 2007 (Tab. 3.2). The average atmospheric sensible heat flux is directed towards the surface in both years, but is more negative in 2008. This corresponds to the pronounced negative night time temperature gradients ($T_{\mathrm{surf}} - T_{\mathrm{air}}$) in 2008. Despite the reduced net radiation, the latent heat fluxes still play a dominant role in the surface energy balance (Fig. 3.5). Almost 50% of the net short-wave radiation is consumed by evapotranspiration, which corresponds to the amount of precipitation during the fall section. The atmospheric stratification in both years is dominated by neutral conditions, corresponding to high wind speeds. However, occasional events of stable stratification occur during calm nights, when the radiation budget becomes highly negative and strong temperature gradients in the atmospheric boundary layer arise. In accordance with the described inter-annual differences in the energy balance evolution, such events are observed more frequently in 2008. In both years, the energy balance closure term C is relatively high (Tab. 3.2). This high closure term can be partly explained by an underestimation of the net radiation: a comparison of the NR-Lite and the four component sensor during fall 2008 reveals an offset of 6 Wm^{-2}, which is substantial considering the generally low radiation budget.

3.5.2 Spatial energy balance variability

The polygonal tundra features pronounced micro-scale heterogeneity, regarding the surface moisture and vegetation cover. The elevated polygonal rims are typically covered with dry mosses, while the lowered centers are filled with wet peat soils or constitute shallow ponds. Considering these surface heterogeneities, spatial differences in the energy balance are likely to occur. Spatially distributed albedo measurements yield typical values in the range of 0.2 for dry and 0.15 for wet tundra surfaces. The latter value is consistent with the average albedo of 0.14 obtained from measurements of the four component radiation sensor, which is directed towards a wet tundra spot. During local noon and clear-sky conditions, the typical surface temperature differences between dry and wet locations are on the order of 5 to 10 °C, which indicates increased radiative losses at the dry and warm surfaces. During the nights and during overcast periods, the spatial differences in the surface temperature and thus the radiation budget largely vanish. However, sustained differences in the net

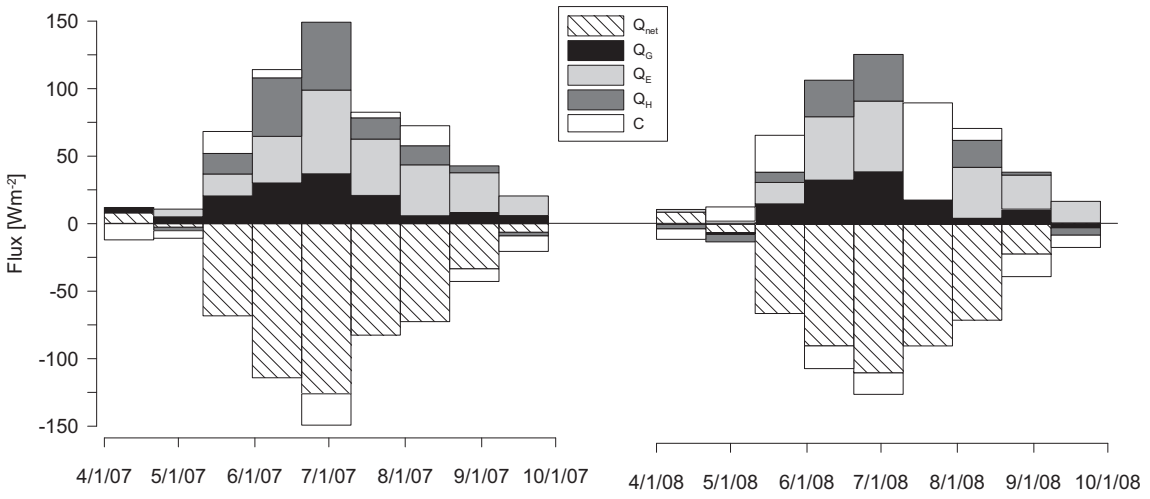

Figure 3.5: The energy balance of 2007 and 2008. Heat fluxes are averaged over 20 days and data gaps in the latent heat fluxes are filled by modeled values. Averages are discarded if the data density is less than 60%. Note that the net radiation is depicted with opposite sign.

radiation budget exist between the tundra soil and the polygonal pond (Fig. 3.6). During the pre-melt period, the net radiation at the polygonal pond is constantly 5 to 10 W m^{-2} lower compared to the tundra surface. After the melt period, the measurements show a significantly higher net radiation at the water body on the order of 20 to 30 W m^{-2}, which gradually diminish in the course of the summer season (Fig. 3.6).
Spatial differences in the turbulent heat fluxes are examined for an exemplary situation at the second location of the mobile eddy system. According to the footprint analysis, the second mobile eddy station features a 20% higher fraction of dry surface area than the reference location (Fig. 3.1). The simultaneous measurements at both location indicates that moderate spatial differences on the order of 20 W m^{-2} (10-20%) can be expected for the sensible and latent heat fluxes under conditions of high radiative forcing ($Q_{\text{net}} > 200$ W m^{-2}) (Fig. 3.7), which occur only sporadically during the summer period (Fig. 3.7). During the fall period, when the radiation balance is further reduced, almost no spatial differences in sensible and latent heat fluxes are measured along the transect.

3.6 Discussion

3.6.1 Data quality

The quality of the energy balance measurements can be evaluated according to the energy balance ratio (Wilson et al. 2002)

$$\text{EBR} = \frac{Q_H + Q_E}{Q_{\text{net}} - Q_G}, \tag{3.8}$$

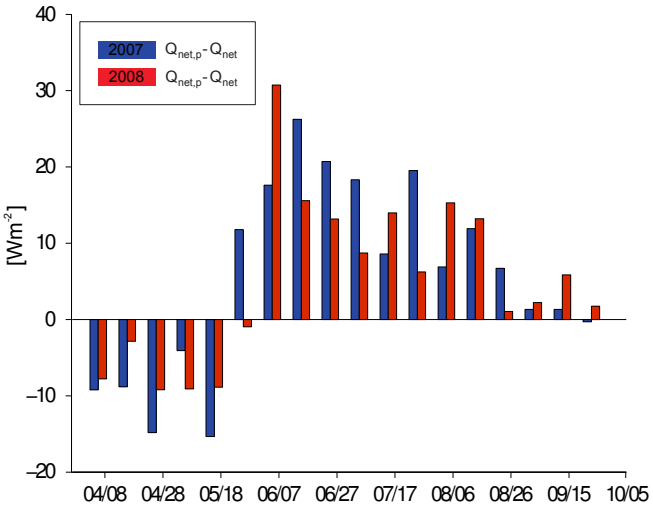

Figure 3.6: Differences in the net radiation budget between the pond and the tundra surface during both observation periods in 2007 and 2008.

which in the case of a closed energy balance (C=0) is unity. The EBR distribution contains information about the characteristics of the errors of the energy balance measurements, such as the presence of systematic and random errors. Since the EBR is highly sensitive to measurement errors during situations of low heat fluxes, we only consider measurements conducted during conditions of $Q_{\mathrm{net}} \leq -30$ W m^{-2} and $Q_{\mathrm{net}} \geq 30$ W m^{-2}. The normalized EBR distribution of the entire data set roughly resembles a normal distribution featuring a mean value of 0.86, a standard deviation of 0.34, and a slightly positive skewness of 0.47 (Fig. 3.8). If only random measurement errors would be involved, the expected EBR distribution should be more similar to the normal distribution displayed in Fig. 3.8. This distribution is calculated assuming a relative error of 15% for $Q_H + Q_E$ (see Sec. 3.4.2) and 20% for $Q_{\mathrm{net}} - Q_G$ (see Sec. 3.4.1), which results in a standard deviation of 0.25. The measured EBR distribution suggests that the energy balance is systematically not closed by about 15%, which is potentially caused by a negative bias of the turbulent heat fluxes or a positive bias of the term $Q_{\mathrm{net}} - Q_G$. The latter is not likely since the employed net radiation sensor (NR-Lite) slightly underestimates the radiation budget (compare Sec. 3.4.1), while the ground heat flux would have to be unrealistically small to cause a positive bias of $Q_{\mathrm{net}} - Q_G$. The shape and width of the measured EBR distribution is similar to the normal distribution, which suggests that the assumed error margins of the energy balance components are realistic.

3.6.2 Controlling factors in the energy balance

Three factors can be identified that essentially determine the energy balance characteristics at the investigated wet tundra landscape. The determining factors are (i) the snow cover, (ii) the presence or absence of a cloud cover and (iii) the thermal state of the permafrost.

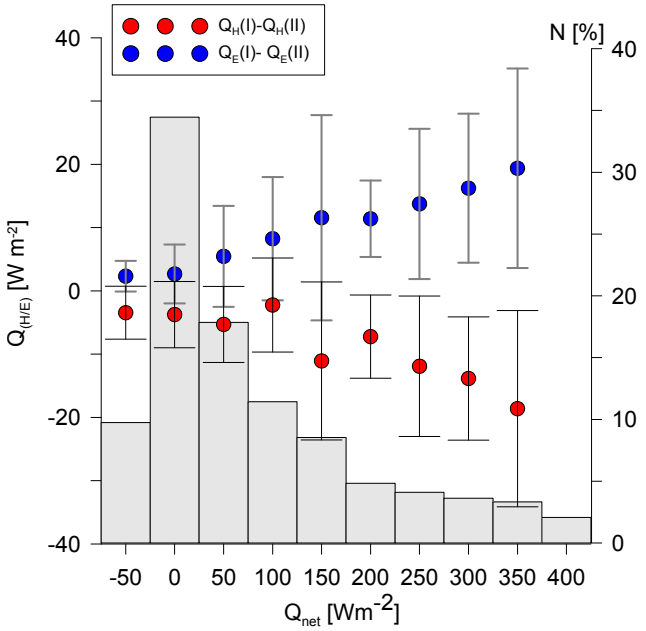

Figure 3.7: The differences of the turbulent heat fluxes between the reference station $Q_{\mathrm{H/E}}(\mathrm{I})$ and the mobile station $Q_{\mathrm{H/E}}(\mathrm{II})$ at the second location of the mobile eddy system. The flux source area of the second Eddy-Covariance system features a 20% higher fraction of dry surface area. The spatial heat flux differences are directly related to the net radiative forcing. The histogram depicts the distribution of net radiation values during the entire summer period.

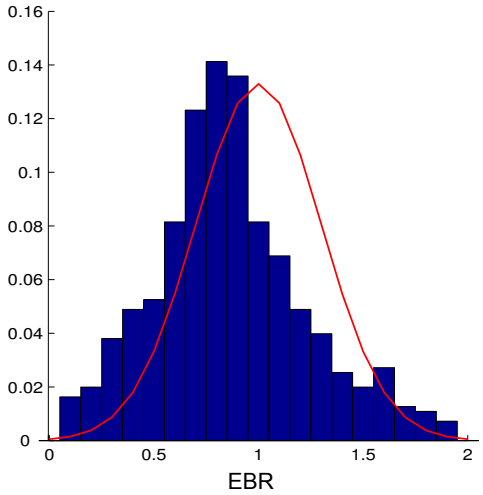

Figure 3.8: The energy balance ratio EBR $= (Q_H + Q_E)/(Q_{\mathrm{net}} - Q_G)$ measured during the summer period. The red line depicts the normal distribution, which would be expected for a closed surface energy balance with random errors.

(i) Although the snow cover is only shallow at the study site, it has strong implications for the surface energy balance. Firstly, the albedo of the snow cover is about a factor of four higher than the albedo of the snow-free tundra surface. Secondly, the thermal conductivity of snow is about a factor of two lower than the thermal conductivity of frozen peat. The second point is of particular importance during winter, when the low thermal conductivity of the snow cover impedes the release of energy from the ground and leads to a reduced ground heat flux (see Langer et al. 2010b). During spring, however, the soil has already cooled out, so that the lower thermal conductivity of the snow is of minor importance for the ground heat budget and the surface energy balance (Goodrich 1982). In contrast, the high albedo of the snow has a strong impact on the surface energy budget during the spring period, when the incoming short-wave radiation already features high values. At the study site, the snow cover effectively reduces the net short-wave radiation until the beginning of the polar day period. The melting of the snow cover with the associated change in surface albedo triggers a sudden change from a winter to a summer surface energy balance, so that the timing of snow melt is a critical point in the annual course of the surface energy balance. In both investigated years, the timing of the snow melt is almost identical. Iijima et al. (2007) point out that snow cover disappearance in eastern Siberia is strongly related to the attenuation of the Siberian-High with subsequent advection of warm and moist air masses from the west. According to the distinct contribution of sensible atmospheric heat flux to the snow melt, our measurements indicate the presence of warm air masses. However, we identify the short-wave radiation as the dominant factor in the snow melt process. We emphasize that the correct representation of the snow melt must be considered crucial in permafrost modeling. It is therefore highly desirable to gather a better understanding of the triggering processes of the snow melt and their representation in models.

(ii) The large-scale advection of warm air is usually related to increased cloudiness, which essentially alters the surface radiation budget and the prevailing surface and air temperature conditions. During the spring period, our results indicate that the observed inter-annual differences in the ground temperatures are caused by different air temperatures, which are presumably related to the general synoptic conditions. During the summer months, the net radiation is essentially reduced for cloud-covered skies, which leads to an effective surface cooling. During the summer months, the cloud cover has an impact on the turbulent heat fluxes, while the ground heat budget is only marginally affected. Since the average surface temperature is not drastically reduced by the increased cloud cover the active layer thawing is only slightly affected. During the fall period, the contrary effect of a cloud cover is observed, as clouds reduce the long-wave radiative losses, which in turn leads to increased surface temperatures. The impact of clouds on the ground heat budget is observed to be largest during the fall season, when increased cloudiness significantly delays the refreezing process in 2007, while the average air temperatures are similar. This ambiguous influence of the cloud cover on the surface radiation budget in the Arctic is confirmed in several studies

(Curry et al. 1996, Intrieri et al. 2002, Shupe and Intrieri 2004).

(iii) During the entire observation period, the ground heat flux is an essential component in the surface energy balance. About 20% of the net radiation is stored as latent and sensible heat in the ground, which is in the upper range of typical values reported for other arctic permafrost regions (Boike et al. 1998, Lynch et al. 1999, Eugster et al. 2000, Westermann et al. 2009). The high contribution of the ground heat flux to the surface energy balance is clearly caused by the cold permafrost temperatures, the shallow active layer depth and the large annual surface temperature amplitude, which is related to the continental climate conditions. Due to the low permafrost temperatures, the sensible heat storage makes up about 50% of the entire ground heat flux. This clearly limits the value of the widely used Stefan equation, that evaluates the active layer dynamics by assuming the ground heat flux to be entirely used for thawing. As the contribution of the ground heat flux to the surface energy balance is significant even in the summer months, an adequate representation of the soil domain in global climate models seems mandatory, if the land-atmosphere exchange processes in permafrost regions are to be modeled correctly. This issue is of particular importance, as permafrost areas with continental climate, where a significant contribution of the ground heat flux can be expected, occupy vast areas in the Arctic. The improvement of modeling results by employing more realistic parameterizations of the soil processes has been outlined in a number of studies (e.g Peters-Lidard et al. 1998, Cox et al. 1999, Viterbo et al. 1999, Pitman 2003). In the second part of this study (Langer et al. 2010b), the representation of the soil and particularly of soil freezing processes in models is discussed in more detail.

3.6.3 Spatial differences of the surface energy balance

In this study, spatial differences in the surface energy balance are observed for (i) the radiation budget and (ii) the turbulent fluxes.

(i) With albedo differences between wet and dry areas on the order of 0.05, the net shortwave radiation can be on average by up to 7 W m^{-2} higher at wet compared to dry areas, while the differences can exceed 25 W m^{-2} for high radiative forcing during midday. This difference is further contrasted by the higher surface temperatures of dry surfaces, which can be about 5 K warmer than wet surfaces during conditions of high radiative forcing. It is therefore conceivable, that the net radiation balance at wet and dry locations can deviate up to 50 W m^{-2} from each other. This difference is partly attenuated during the night, when the wet surfaces are warmer and the shortwave forcing is nonexistent or negligible. Moreover, due to the rare occurrence of high values of net radiation we assume that the average differences in net radiation between wet and dry areas does not exceed 10 W m^{-2}.
More pronounced spatial differences in the radiation balance are measured between the tundra and water bodies. The net radiation of the investigated pond is slightly lower in frozen conditions during spring, but significantly higher during the summer months.

Albedo differences during spring are not likely, since all surfaces are covered by snow, so that the measured differences in the radiation budget are most likely explained by an increased surface temperatures at the frozen pond during spring (see Langer et al. 2010b). During the summer period, almost similar surface temperatures are observed for the water body and the tundra surface. Hence, the differences in net radiation are most likely explained by a lower albedo of the water body. The pond investigated in this study indicates that small shallow water bodies can have a significant influence on the radiation budget in polygonal tundra landscapes, as they are frequent landscape elements. While the impact of larger water bodies on the arctic climate conditions has been investigated (Krinner 2003, Rouse et al. 2005, Krinner and Boike 2010), such small water bodies have not received similar attention. It is thus highly desirable to evaluate the impact of small water bodies on the larger-scale surface energy balance, particularly since such micro-scale landscape structures usually remain undetected in remote sensing applications and are neglected in model approaches. In the second part of this study (Langer et al. 2010b), the winter aspect of the surface energy balance of small ponds is addressed in more detail.

(ii) Micro-scale differences of the turbulent fluxes are verified by the mobile eddy covariance system. The measurements reveal differences in sensible and latent heat fluxes according to variations in the fractions of dry and wet surfaces in the footprint areas (Fig. 3.4). The observed spatial variations are caused by the small scale surface temperature differences between wet and dry areas. As the temperature difference between wet and dry surfaces depends on the net radiation budget, significant differences in the turbulent fluxes are limited to clear-sky situations, which only occur occasionally during the summer period. Since the long-term averages of the turbulent heat fluxes are almost equal for the stationary and the mobile eddy covariance system, we conclude that the presented sensible and latent heat fluxes are representative on the landscape scale.

3.7 Conclusions

In this study we present a comprehensive surface energy balance study of at wet polygonal tundra landscape from April to September (2007-2008) considering seasonal and spatial variations. This comprehensive study improves the understanding of the energy exchange processes at soil-atmosphere interface of a typical permafrost landscape. The obtained results can be of great value for the improvement and development of permafrost model schemes, as they are intended to be incorporated in climate models. In particular the following conclusions can be drawn from the obtained results:

- The spring, summer and fall energy balance is dominated by the net radiation. Critical factors for the surface radiation budget are in particular the snow cover and clouds. The timing of snow melt in spring essentially controls the amount of short-wave radiation that is available for energy partitioning. The relevance of the snow cover for

the surface radiation budget is further intensified by the presence of almost polar day conditions. The cloud cover has its greatest impact on the ground heat budget during fall, when radiative losses are largely reduced and the refreezing of the tundra is significantly delayed.

- The surface energy balance is essentially affected by the ground heat flux, which is of similar magnitude as the sensible heat flux. The significant ground heat flux is induced by strong temperature gradients in the shallow active layer and in the permafrost body, which are the result of both continental climate and high soil water and ice content.

- The larger scale surface energy balance is significantly affected by the occurrence of small water bodies, which essentially affects the surface radiation budget and the ground heat storage of the tundra landscape.

3.8 Appendix

Definitions and constants

Q_{net}: net radiation
$Q_{S\downarrow}$: incoming short-wave radiation
$Q_{S\uparrow}$: outgoing short-wave radiation
ΔQ_S : net short-wave radiation
$Q_{L\downarrow}$: incoming long-wave radiation
$Q_{L\uparrow}$: outgoing long-wave radiation
ΔQ_L: net long-wave radiation
Q_{HB}: buoyancy flux
Q_H: sensible heat flux
Q_E: latent heat flux
Q_G: ground or snow heat flux
E_{melt}: latent heat content of the snow pack
Q_{melt}: energy flux through melting of the snow pack
C: residual of the energy balance
u: horizontal wind speed
w: vertical wind speed
T_{air}: air temperature
T_s: sonic air temperature
T_v: virtual temperature
q: specific humidity
u_*: friction velocity
z_0: aerodynamic roughness length
$\zeta = z/L_*$: stability parameter (z: measurement height, L_*: Obukhov length)
$\kappa = 0.4$: von Kármán constant
R_H: relative humidity

T_{surf}: surface temperature
α: surface albedo
ϵ: surface emissivity
σ: Stefan-Boltzmann constant
c_p: specific heat capacity of air at constant pressure
ρ_{air}: density of air
$\rho_w = 1.0\,\mathrm{g\,cm^{-3}}$: density of water
$\rho_{\mathrm{ice}} = 0.91\,\mathrm{g\,cm^{-3}}$: density of ice
$L_{sl} = 0.33\,\mathrm{MJ\,kg^{-1}}$: specific latent heat of fusion of water
$L_{lg} = 2.5\,\mathrm{MJ\,kg^{-1}}$: specific latent heat of vaporization of water
$L_{sg} = 2.8\,\mathrm{MJ\,kg^{-1}}$: specific latent heat of sublimation of ice
D_h: thermal diffusivity
K_h: thermal conductivity
C_h: volumetric heat capacity
$C_{h,w} = 4.2\,\mathrm{MJ\,m^{-3}K^{-1}}$: volumetric heat capacity of water
$C_{h,i} = 1.9\,\mathrm{MJ\,m^{-3}K^{-1}}$: volumetric heat capacity of ice
$C_{h,a} \approx 0.001\,\mathrm{MJ\,m^{-3}K^{-1}}$: volumetric heat capacity of air
$C_{h,s} \approx 2.3\,\mathrm{MJ\,m^{-3}K^{-1}}$: volumetric heat capacity of the solid soil matrix
A bulk heat capacity $C_{h,s}$ is used for the solid matrix, since typical values of organic and mineral soils do not differ more than 20% from each other (compare Sect. 3.4.3)

3.8.1 The calorimetric method

The change of the sensible heat content of a soil volume with area A and depth z with uniform temperature and a constant heat capacity is given by

$$E(t_2) - E(t_1) \;=\; A\,z\,C_h\,(T(t_2) - T(t_1)), \tag{3.9}$$

where $T(t_1)$ and $T(t_2)$ are the temperatures at times t_1 and t_2. In the case of a temperature dependence of the heat capacity and non-uniform temperature distribution in depth $C_h(T(t,z))$, Eq. 3.9 must be rewritten to

$$E(t_2) - E(t_1) \;=\; A \int_0^z \int_{T(t_1,z')}^{T(t_2,z')} C_h(T')\,dT'\,dz'. \tag{3.10}$$

The temperature dependence of C_h is caused by the phase change of water and is calculated as

$$\begin{aligned} C_h(T) \;&=\; \theta(T)\,C_{h,w} + (\theta_{\max} - \theta(T))C_{h,i} \\ &+\; (1 - P_{\mathrm{dry}})C_{h,s}, \end{aligned} \tag{3.11}$$

where P_{dry} is the porosity of the soil, $\theta_{\max}$ is the maximum unfrozen water content, and $\theta(T)$ is the temperature-dependent liquid water content, which is referred to as 'freeze characteristic'. The volumetric fraction of the solid matrix and thus the porosity is determined

from soil samples and the volumetric water and ice content is obtained from in situ TDR-measurements (see Boike et al. 2003; for details). To account for the release or consumption of energy through freezing and thawing, Eq. 3.10 is extended to

$$\begin{aligned} E(t_2) - E(t_1) &= A \int_0^z \rho_w L_{sl} [\theta(T(t_2, z')) - \theta(T(t_1, z'))] \, dz' \\ &+ A \int_0^z \int_{T(t_1,z')}^{T(t_2,z')} C_h(T') \, dT' \, dz'. \end{aligned} \tag{3.12}$$

This method of ground heat flux determination requires knowledge about the soil-specific freeze characteristics or direct measurements of the soil water content. The employed soil temperature measurements must extend to a depth of constant temperatures during the considered measurement period. If such a deep temperature profile is not available, the heat flux below the measurement depth can be obtained by solving the heat transfer equation at the lower boundary (Eq. 3.15, see below).

3.8.2 The conductive method

The conductive method makes use of the heat transfer equation to determine the ground heat flux. Firstly, the thermal conductivity of the soil or snow must be evaluated. This procedure requires a time series of soil temperatures measured in a profile at three depths, $T_m(z_1, t)$, $T_m(z_2, t)$ and $T_m(z_3, t)$ with $z_1 < z_2 < z_3$. The one-dimensional heat transfer equation is written as

$$C_h(t, z) \frac{\partial T(t, z)}{\partial t} = \frac{\partial}{\partial z} K_h(t, z) \frac{\partial T(t, z)}{\partial z} \tag{3.13}$$

where $T(t, z)$ denotes the soil or snow temperature at time t and depth z. Assuming constant heat capacities and thermal conductivities $K_h(t, z)$ in space and time, the one-dimensional heat transfer equation is simplified to

$$\frac{\partial T(z, t)}{\partial t} = D_h \frac{\partial^2 T(z, t)}{\partial z^2} \tag{3.14}$$

where $D_h = K_h / C_h$ denotes the thermal diffusivity. The solution of Eq. 3.14) is obtained by the partial differential equation solver incorporated in MATLAB. The required boundary conditions are given by the outer sensors of the temperature profile, $T_m(z_1, t)$ and $T_m(z_3, t)$. The initial conditions are inferred from linear interpolation between all the three sensors at $t = 0$, which is not critical to the solution, since it becomes independent of the initial temperature state after a few time steps in the shallow soil layer. The numerical solver delivers the temperature distribution of the considered spatial domain, including $T(t, z_2)$, so that the thermal diffusivity D_h can be evaluated by minimizing the least mean square error to the measured temperatures at depth z_2, $T_m(t, z_2)$. We use time series of several days for the determination of the thermal diffusivity of different surface substrates (see Tab. 3.1). Note that this procedure assumes homogeneous substrate composition in the

considered soil or snow layer, which may not be the case in nature. The heat flux through the upper boundary can be evaluated by

$$Q_G(t) \;=\; D_h C_h \left.\frac{\partial T(z,t)}{\partial z}\right|_{z=z_1} . \tag{3.15}$$

The conductive methods has been applied by Westermann et al. (2009), while similar concepts are explored by Nicolsky et al. (2009).

3.8.3 Modeling of latent heat fluxes

This model approach is used when eddy covariance measurements of the latent heat flux are not available. The model is based on eddy-covariance measurements of wind speed and sonic temperature and uses ancillary measurements of relative humidity and surface temperature. The model is based on commonly used parameterizations of the atmospheric transport mechanisms (Foken 2008), which we shortly describe in the following. According to Monin-Obukhov similarity theory, the latent heat flux can be related to the difference between specific humidity at measurement height $\overline{q}(z_m)$ and roughness length $\overline{q}(z_0)$ by

$$\overline{q'w'} \;=\; \left(\overline{q}(z_m) - \overline{q}(z_0)\right) \kappa u_* \left[\ln\frac{z_m}{z_0} - \Psi_W\left(\frac{z_m}{L_*}, \frac{z_0}{L_*}\right)\right]^{-1} \tag{3.16}$$

with

$$\Psi_W\left(\frac{z_m}{L_*}, \frac{z_0}{L_*}\right) \;=\; \int_{z_0}^{z_m} \frac{1-\varphi_W(z'/L_*)}{z'} dz', \tag{3.17}$$

where κ denotes the von Kármán constant (0.4), u_* the friction velocity and $\varphi(z/L_*)$ is a universal function (see below). The quotient z/L_* denotes the stability parameter ζ, where L_* is the Obukhov length L_* defined in Eq. 3.21. Using Eq. 3.16 and rewriting the turbulent transport terms as atmospheric resistance r_a, the latent heat flux Q_E can be evaluated by

$$Q_E \;=\; -\frac{\rho_{\text{air}} L_{lg}}{r_a + r_s} \left(\overline{q}(z_m) - \overline{q}(z_0)\right), \tag{3.18}$$

with

$$r_a \;:=\; (\kappa u_*)^{-1} \left[\ln\frac{z_m}{z_0} - \Psi_W\left(\frac{z_m}{L_*}, \frac{z_0}{L_*}\right)\right], \tag{3.19}$$

where ρ_{air} is the density of air, L_{lg} the latent heat of vaporization of water and r_s the surface resistance to evapotranspiration (Garratt 1994). For calculation over the snow surface L_{lg} must be replaced by the latent heat of sublimation L_{sg}. The specific humidity at the surface $q(z_0)$ is inferred from to the surface temperature T_{surf} using the Magnus formula that delivers the water vapor pressure over a water surface or an ice surface, respectively. During the summer month, the surface is not entirely saturated, and a surface resistance is required to account for the reduced availability of water. We use measured time series of the latent heat flux to fit the surface resistance of summer and fall. We assume the surface resistance to be constant in time. The roughness length z_0 can be inferred from measurements of u_*^2

under neutral atmospheric conditions (Foken 2008). Note that we assume the aerodynamic roughness length to be the roughness length of water vapor. The fitting procedure yields a surface resistance of about $50\,\mathrm{sm}^{-1}$ with a roughness length determined to be $10^{-3}\,\mathrm{m}$ during the summer period. When the ground is snow-covered, the surface resistance is set to zero, while the roughness is determined to $5{\times}10^{-4}\,\mathrm{m}$ The universal universal function Ψ_W is chosen according to Høgstrøm (1988) as

$$\varphi_W(\zeta) = \begin{cases} 0.95\,(1 - 11.6\,\zeta)^{-1/4} & \text{for } \zeta \leq 0 \\ 0.95 + 7.8\,\zeta & \text{for } \zeta > 0 \end{cases} \tag{3.20}$$

The Obukhov length L_*, which is required for the stability parameter ζ is directly obtained from eddy-covariance measurements using

$$L_* = -\frac{u_*^3 \overline{T}_v}{\kappa g(\overline{T_v' w'})}, \tag{3.21}$$

where g is the gravitational acceleration and T_v the virtual temperature. Note that the virtual temperature T_v is substituted by the sonic temperature T_s (Foken 2008).

3.9 Acknowledgements

We are thankful to the Department of Micro-Meteorology of the University of Bayreuth headed by Thomas Foken for providing the eddy-covariance post-processing software. We are also thankful to Claudia Fiencke and Tina Sanders from the Institute of Soil Science of the University of Hamburg for the soil component analyses. We gratefully acknowledge financial support by the Helmholtz Association through a grant (VH-NG 203) awarded to Julia Boike.

Chapter 4

Paper III
Permafrost and surface energy balance of a polygonal tundra site in northern Siberia - Part II: Winter

4.1 Introduction

Numerous studies based on climate models revealed that the large-scale atmospheric conditions are greatly impacted by the heat and moisture turnover at the surface-atmosphere interface (e.g. Viterbo et al. 1999, Delire et al. 2002, Pitman 2003, Rinke et al. 2008). Recent studies also showed that the most pronounced arctic warming occurs during the winter and early spring period (Moritz et al. 2002, Johannessen et al. 2004). According to model predictions, it is expected that the significant arctic warming during the last decades (e.g. Overpeck et al. 1997, Comiso 2003, Hinzman et al. 2005, Tape et al. 2006, Turner et al. 2007, Overland et al. 2008) is accelerated due to positive feedback mechanisms, such as a shrinking sea-ice cover and increased cloudiness (e.g. Holland and Bitz 2003, Kaplan et al. 2003, Vavrus 2004).
The winter time surface energy balance of the arctic constitutes an essential factor in the regional climate system, since it affects the atmospheric heat budget due to sensible, latent and radiative energy exchange with the surface over a long-lasting period. Hence, for the evaluation and the development of large-scale model parameterizations, energy balance studies are an indispensable tool. In the Arctic, only few comprehensive energy balance studies exist within this large geographical area, especially for the winter period. The importance of the winter surface energy balance on the thermal state of the permafrost has been most recently demonstrated by Westermann et al. (2009) for a site on Svalbard: here, the snow surface temperature is largely controlled by the long-wave radiation balance, which in conjunction with the evolution of the snow cover and more complex processes, such as wintertime rain events, determines the thermal regime of the ground. Osterkamp (2005) reported that the winter and spring warming essentially affects the heat budget of permafrost soils.
Energy balance studies give insight into the processes, which are relevant for both the permafrost and the atmospheric heat budget. This is especially important for the development of new model schemes, which aim to incorporate permafrost due to its high carbon stock

and its potential feedback to climate change. Recent effort in global permafrost modeling has already been initiated (e.g. Stendel and Christensen 2002, Lawrence and Slater 2005, Nicolsky et al. 2007, Lawrence et al. 2008). However, the accuracy of these models depend on the realistic representation of the ground-atmosphere energy exchange processes, which are determined by parameterizations of the local surface and subsurface properties (e.g. roughness length, soil heat conductivity, snow cover characteristics).
This study is the second part of a comprehensive investigation on the annual surface energy balance at a wet tundra site in northern Siberia. The results of the first part of this study (Langer et al. 2010a) revealed that the sensitivity of the permafrost heat budget towards variations in radiation balance and turbulent heat fluxes is highest at the beginning and end of the summer thaw cycle. Furthermore, the permafrost heat budget appears to be less sensitive to surface energy balance variations during the high summer period. In this second paper, we focus on the surface energy balance during the winter periods from October 1, 2007, until March 30, 2008, and October 1, 2008, until January 30, 2009. We aim to achieve (i) the identification of the controlling and limiting factors of the surface energy balance, (ii) the evaluation of the seasonal and inter-annual variability of the energy balance components and (iii) the detection and evaluation of spatial differences of the surface energy balance by spatially distributed measurements. The results are discussed with respect to larger-scale modeling of the arctic boundary layer and the permafrost.

4.2 Study site

The study site is located at the southern part of the Lena River Delta on Samoylov Island (72° 22' N; 126° 30' E) (Fig. 4.1). The regional climate is arctic-continental with a mean annual air temperature (MAAT) of about −13 °C, a pronounced annual temperature amplitude of about 60 °C and a total annual precipitation around 250 mm (Boike et al. 2008). Snow fall and soil refreezing begins towards the end of September. The winter period is characterized by the polar night, which lasts from mid of November until end of January. The climate and synoptic conditions during the winter are largely determined by the Siberian High, which causes air temperatures to fall frequently below −45 °C. The high pressure system is often disturbed by the influx of cyclones with high intensity and short lifetime (Zhang et al. 2004). The continental climate conditions are also reflected in the thermal regime of the soil, which is characterized by continuous permafrost reaching depths of 500 to 600 m (Grigoriev 1960). At the depth of the zero annual amplitude ($\approx$ 15 m) the soil temperature is about −10 °C. During the summer months, the maximum thaw depth ranges from 0.4 to 0.5 m. The tundra surface is highly fractionated due to polygonal structures, which are typically 50 to 100 m^2 large. The rims of these polygons are elevated by about 0.2 to 0.5 m compared to the centers, which consist of water-saturated peat soils or constitute shallow ponds. The vegetation at the polygonal centers is dominated by hydrophilic sedges and mosses, while the elevated rims are dominated by mesophytic dwarf shrubs, forbs and mosses. During the winter period, the tundra surface is covered by a shallow snow layer, which typically features depths of less than 0.5 m at the depressed centers

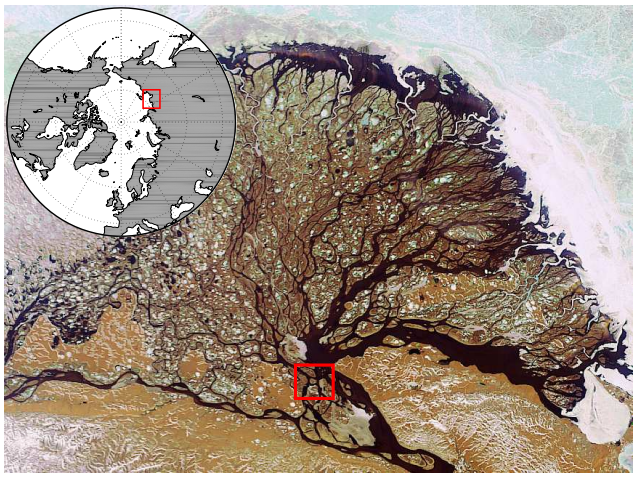

Figure 4.1: The location of the study site in the Lena River Delta on a Envisat (MERIS) image acquired on 15 June 2006 (ESA 2006). The Lena Delta covers an area of approximately $30,000$ km^2.

and only a few centimeters at the elevated rims.

4.3 Methods

For the evaluation of the surface energy balance and the quantification of spatial variabilities at the study site we distinguish between two basic landscape features during the winter period: the snow covered tundra soils and freezing or frozen water bodies. The surface energy balance of the snow covered tundra soils (referred to as tundra site) is measured as a spatial average including polygonal centers and rims (compare Sec. 4.2). Whereas components of the energy balance (net radiation, subsurface heat flux) of water bodies are exemplified at a polygonal pond (referred to as pond site). The energy balance equation for the tundra site is written as

$$Q_{\mathrm{net}} = Q_H + Q_E + Q_G + C, \tag{4.1}$$

where Q_{net} is the net radiation, Q_H the turbulent sensible heat flux, Q_E the turbulent latent heat flux, Q_G the subsurface (ground or snow) heat flux and C is the residual of the energy balance, which accounts for inaccuracies of measurement. The pond, at which the net radiation $Q_{\mathrm{net,p}}$ and the subsurface heat flux $Q_{\mathrm{G,p}}$ are measured, features a depth of about 0.8 m and a water volume of about 70 m^3. The basic concepts of the measurements and the data analysis applied in the present study are already described in the first part of this study (Langer et al. 2010a). The applied methods are re-summarized briefly, while new methods and additional measurements are described in more detail in the following.

4.3.1 Radiation balance and turbulent heat fluxes

The net radiation at the tundra and pond sites are measured with a net radiations sensor (NR-Lite, Kipp & Zonen, Netherlands). The net radiation sensor at the tundra site is not available in the second winter period (2008-2009), but we apply a four-component radiation sensor (CNR1, Kipp & Zonen, Netherlands) to calculate the net radiation. The outgoing thermal radiation is measured by a long-wave radiation sensor in winter 2007-2008 (CG1, Kipp & Zonen, Netherlands) and calculated from infrared surface temperature sensors (IRTS-P, Apogee Instruments, USA) in winter 2008-2009 using Stefan-Boltzmann law (compare Langer et al. 2010a). For this calculation, we assume the surface emissivity of the snow cover to be 0.98 according to commonly used values (Rees 1993).
The eddy covariance setup is reduced to the 3D sonic anemometer (C-SAT, Campbell Scientific, USA) during winter, from which we infer the turbulent sensible heat flux Q_H. The reduced measurement setup only permits the detection of the momentum flux u_*^2 and the buoyancy flux Q_{HB}, which in principle must be corrected according to the flux of water vapor to obtain the true sensible heat flux Q_H (Schotanus et al. 1983). Due to the extremely cold air temperatures, we assume the flux of water vapor to be very small during winter, so that the difference between the buoyancy and sensible heat flux is small. Hence, we accept the buoyancy flux to be a good approximation of the real sensible heat flux during the winter period. According to a quality check and the exclusion of the lee wind sector (263°to 277°), about 18% of the flux measurements must be discarded. From the stability parameter ζ, the atmospheric stratification can be inferred, with $\zeta \approx 0$ for a well mixed or neutrally stratified atmosphere, $\zeta > 0$ for stable and $\zeta < 0$ for unstable atmospheric stratifications.
The latent heat flux is modeled by an approach similar to the one used in the first part of this study (Langer et al. 2010a). The model uses the often applied parametrization introduced by Høgstrøm (1988) and is based on available eddy-covariance measurements of the momentum flux u_*^2 and the buoyancy flux Q_{HB}, from which a turbulent transport coefficient can be inferred (compare Langer et al. 2010a). In addition, the model requires measurements of relative humidity R_H and surface temperature T_{surf} for calculating the near-surface gradient of the specific humidity. During winter 2007-2008, we rely on measurements of relative humidity from the standard climate station in the vicinity of the eddy covariance system. During winter 2008-2009, the relative humidity is estimated to be in the range of (70±5)% according to the measurements of the previous year.

4.3.2 Subsurface heat fluxes

Subsurfaces heat fluxes are calculated for a tundra site (Q_G) and a thermokarst pond ($Q_{\mathrm{G,p}}$). The ground heat flux Q_G is the heat flux across the surface, which can be either the soil or the snow surface. For the heat flux calculations, we apply the calorimetric and the conductive method, which both are described in detail in the first part of this study (Langer et al. 2010a).
The calorimetric method calculates the ground heat flux based on changes in the internal energy of a soil column using measurements of the soil temperature and liquid water content

θ_w. This method is used for evaluating averages of the ground heat flux over periods longer than a few days, since the impact of measurement errors of the soil temperature and the water content decreases for longer periods. Moreover, due to the measurements of temperature and liquid water content, it is possible to distinguish sensible and latent heat storage, which we express as energy fluxes $Q_{G,\text{sensible}}$ and $Q_{G,\text{latent}}$. Note, that the heat storage in the shallow snow layer becomes negligible for long-term averages, so that temperature profiles in the snow pack are not required.
The conductive method is applied for both calculations of the ground heat flux at the tundra site and the thermokarst pond. For the tundra site, this method is only applied for calculating heat fluxes with hourly resolution, whereas it is used to calculate long-term averages at the pond. The conductive method calculates the heat flux through a layer by solving the differential equation of conductive heat transport (compare Langer et al. 2010a). For the conductive method, the thermal diffusivity of the snow or soil must be evaluated, which are presented in Tab. 4.1. The used measurement setups for the different methods and sites are described in the following.

The calorimetric method (tundra site)

During winter 2007-2008, soil temperatures are available from a 26 m borehole and a thermistor profile in the active layer. The liquid water content θ_w is measured in the active layer by Time-Domain-Reflectometry (TDR) probes (compare Langer et al. 2010a). Since the deep borehole and the TDR probes are not available during winter 2008-2009, we rely on a shallow borehole of 4 m depth and a parametrization of the liquid water content in dependence of the soil temperature. This so-called freezing characteristic is inferred by fitting a polynomial function to measurements of water content and temperature of the previous year (Fig. 4.2). Since the calorimetric method requires measurements down to a depth of zero temperature change in the concerned averaging period, heat fluxes below 4 m are required. We therefore calculate the heat flux through the lower boundary of the temperature profile by using the conductive method (compare Langer et al. 2010a). Soil heat capacities, thermal diffusivity and heat conductivity of frozen tundra soils are evaluated similar to the summer time values (Tab. 4.1).

Conductive method (tundra site)

Two different sets of measurements are used to calculate the heat flux through the snow with the conductive method. Firstly, snow temperature measurements at three depths with known relative distance are employed. This method is similar to the conductive heat flux calculation used for the uppermost soil layer in the first part of this study (compare Langer et al. 2010a) and involves the determination of the thermal diffusivity of the snow cover. The required snow temperature profile measurements are available during winter 2008-2009. The used measurement setup consists of an array of temperature sensors (thermocouple) fixed on very thin (4 mm) carbon rods of different length, which are placed vertically about 3 cm apart from each other. The height difference between the temperature sensors is 5 cm. Secondly, the snow heat flux is calculated using the surface temperature of the snow cover,

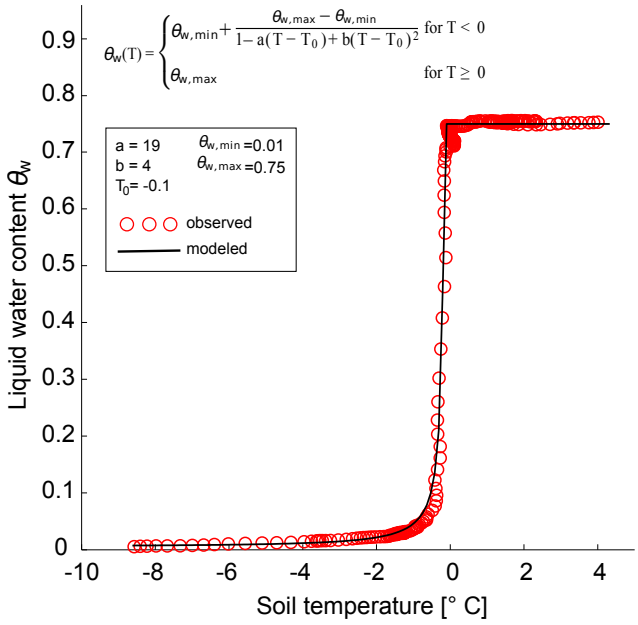

Figure 4.2: The freezing characteristic of the soil at the study site, which parameterizes the soil water content θ_w in dependence to the soil temperature. The used polynomial function and the fitted parameters are depicted in the figure. $\theta_{\mathrm{w,max}}$ denotes the maximum liquid water content in unfrozen condition and $\theta_{\mathrm{w,min}}$ the minimum liquid water content in completely frozen condition.

Table 4.1: Used soil parameters for ground heat flux calculations during the winter period. Values of porosity P_{dry} and volumetric ice content θ_i are estimated based on soil sample analysis and in situ soil water content measurements during summer. The heat capacities are calculated by weighting $C_{h,i}$ and $C_{h,s}$ according to the assumed ice content and porosity. The thermal diffusivities D_h are determined by using the conductive method described in the first part of this study, from which we evaluate the thermal conductivity values K_h with the estimated heat capacity. Errors are calculated using Gaussian error propagation.

Substrate	P_{dry}	θ_i	C_h [$\mathrm{MJ\,m^{-3}K^{-1}}$]	D_h [$\mathrm{m^2\,s^{-1}}$]	K_h [$\mathrm{W\,m^{-1}\,K^{-1}}$]
frozen dry peat	0.8 ± 0.1	0.1 ± 0.1	0.7 ± 0.3	0.68 ± 0.19	0.46 ± 0.25
frozen wet peat	0.8 ± 0.1	0.7 ± 0.1	1.8 ± 0.3	0.54 ± 0.09	0.95 ± 0.23
frozen saturated peat	0.8 ± 0.1	0.8 ± 0.1	2.0 ± 0.05	0.96 ± 0.09	1.92 ± 0.19
snow	$\rho_{\mathrm{snow}} = 190 \pm 10$ [$\mathrm{kg\,m^{-3}}$]		0.40 ± 0.04	0.54 ± 0.04	0.22 ± 0.03
ice	$\rho_{\mathrm{ice}} = 920$ [$\mathrm{kg\,m^{-3}}$]		1.9	1.2	2.3

the temperature at the snow-soil interface, the snow depth and the thermal diffusivity and conductivity of the snow cover. This method is applied during the winter 2007-2008, when the snow temperature profile is not available. The snow surface temperature is measured by an infrared sensor, the temperature at the snow-soil interface is measured by a thermistor close to the surface and the required snow depth is obtained by an ultrasonic ranging sensor. We further assume a similar thermal diffusivity of the snow cover, as calculated from the temperature profile measurements of the following year. The obtained snow heat fluxes must be considered a rough approximation, since the assumption of constant thermal snow properties may be violated in reality (e.g. Sturm et al. 1997, Zhang 2005).

Conductive method (pond site)

In addition, the heat flux through the ice layer of the instrumented polygonal pond, $Q_{G,p}$, is determined. The employed temperature profile consists of four temperature sensors which are fixed on a mast located in the middle of the water body, where the water depth is approximately 0.8 m. In the course of the winter, the temperature sensors freeze in the ice of the pond. From the temperature profile, we can calculate the heat flux through the ice layer, as soon as it approaches a thickness of 24 cm, which then contains the two uppermost temperature sensors of the profile. We use the conductive method described in Langer et al. (2010a) to evaluate the heat flux through the ice cover surface with the known thermal diffusivity and conductivity of ice. The employed values are depicted in Tab. 4.1.

4.3.3 Snow cover measurements

A shallow snow cover characterizes the surface at the study site during winter. We use different methods for the detection of the snow depth. The snow depth is measured with an ultrasonic ranging sensors (SR50, Campbell Scientific, USA) located at the tundra site and at the pond site. During winter 2008-2009, the ultrasonic sensor is not available at the

tundra site. Therefore, we infer the snow depth from the snow temperature profile described in Sec. 4.3.2 using the method of Lewkowicz (2008), who determines the snow depth from a significant temperature decoupling between buried and unburied sensors. The temperature profile provides a vertical resolution of 5 cm. In addition, we use the AMSR-E 5-Day L3 snow water equivalent (SWE) product (Kelly et al. 2004) to obtain a complementary snow cover information to the available point measurements. The satellite product is based on passive microwave detection and features a spatial resolution of 25 km. A detailed technical description of the product and the retrieval algorithm is given by Pulliainen and Hallikainen (2001). For tundra surfaces, the accuracy of the SWE product is expected to be in the range of 10% , since the shallow vegetation only marginally affects the snow cover signal (Foster et al. 2005). We selected the closest pixel to the study site, which must be understood as an average value over a large variety of surface structures.
Moreover, SWE field measurements are conducted during April 2008 and 2009. From these measurements, we calculate the snow heat capacity, which is used for the heat flux calculations. The obtained values are presented in Tab. 4.1. The field measurements of the snow density ρ_{snow} are further used for the conversion of the AMSR-E dataset from SWE to snow depths.

4.4 Results

In the following, we describe the winter surface energy balance. We divide the observation period into three sections, according to the availability of sunlight. During the first and the last winter sections short wave radiation is still or again present, whereas the middle period is characterized by the absence of sunlight due to polar night conditions.

4.4.1 Early winter (October 1 – November 30)

The first winter period lasts from the beginning of October until the end of November, immediately before the beginning of the polar night. The surface energy balance is characterized by a strongly negative radiation budget on the order of -20 W m^{-2}, which is about 25 W m^{-2} less compared to the preceding fall season (compare Langer et al. 2010a). The short-wave radiation budget is very small (≈ 2 W m^{-2}) due to the high albedo of the snow cover. The negative radiation budget is largely balanced by the ground heat flux Q_G (-10 to -20 W m^{-2}), whereas the sensible heat flux Q_H shows only a marginal contribution of about -5 W m^{-2}, which is only slightly more negative than during the fall season. The modeled latent heat flux Q_E is still significantly positive (≈ 10 W m^{-2}), which agrees with the high values measured in the previous fall period. Similar to the fall period, the energy balance residual C is considerable, which indicates that some heat flux is not detected.
The general weather conditions are characterized by rapidly declining air temperatures, decreasing sun angles, snow accumulation and the freezing of soil and water bodies. In both years, the air temperatures rapidly fall from about 0 °C at the beginning to -20 °C at the end of the period. The build-up of a continuous snow cover starts in both winters at the beginning of October. However, we observe significant differences in the evolution of the

Table 4.2: Average heat fluxes and essential climate parameters. According to the available dataset, sub-periods are required during the late winter section. Values are in Wm^{-2} , if not indicated differently. Turbulent heat flux values marked in bold are affected by minor data gaps due to quality assessment or the exclusion of lee wind sectors. Radiation values measured with the NR-Lite sensor are marked with $^{\ominus}$, and values obtained with the four component sensor (CNR1) are indicated with $^{\oplus}$. Modeled values of latent heat flux are indicated with ‡

.

	Early winter		Polar winter		Late winter	
	2007	2008	2007-2008	2008-2009	2008	2009
	10/01-11/30	10/01-11/30	12/01-01/30	12/01-01/30	02/27-03/30	02/01-03/30
Q_{net}	-17$^{\ominus}$	-21$^{\oplus}$	-21$^{\ominus}$	-25$^{\oplus}$	-14.7$^{\ominus}$	-
ΔQ_{S}	-	1.5	0	0	-	-
ΔQ_{L}	-	-22	-21	-25	-	-
Q_{H}	**-6**	**-5**	**-9**	-	**-10,3**	-
Q_{E}	**9**‡	**13**‡	**4**‡	-	**3**‡	-
Q_{G}	-11	-20	-17	-14	-5.4	-
$Q_{G,\mathrm{sensible}}$	3	-3	-14	-14	-5.4	-
$Q_{G,\mathrm{latent}}$	-14	-17	-3	0	0	-
C	-9	-9	-1	-	2	-
$Q_{\mathrm{net,p}}$	-18	-23	-22	-25	-20	
$Q_{\mathrm{G,p}}$	-12†	-34†	-32	-28	-12.6	
T_{surf} [°C]	-16	-15	-29.9	-29.7	-25.9	
T_{air} [°C]	-16.1	-14.8	-29.7	-29.5	-24.8	
R_{H} [%]	81	-	70	-	75	
Snow depth [m]	0.09	0.05	0.11	0.15	0.18	

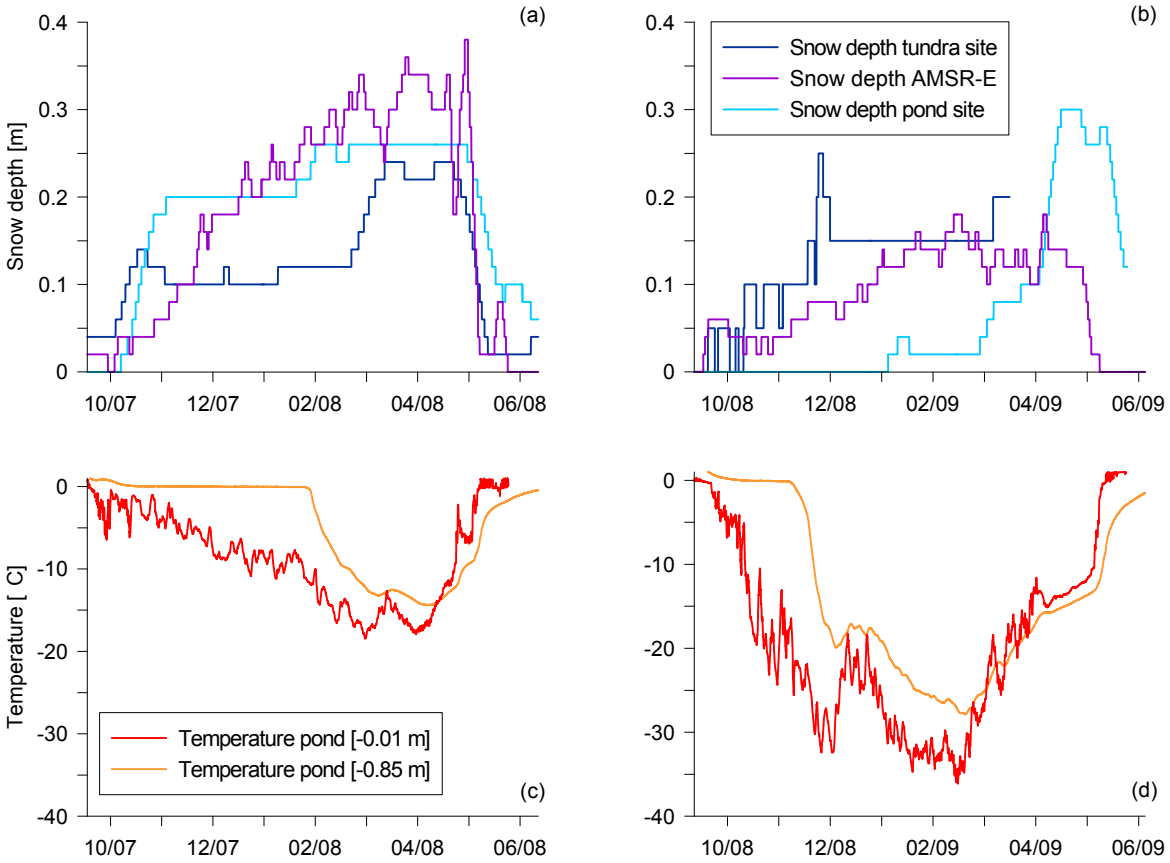

Figure 4.3: The diagrams at the top show the evolution of the snow depth measured at the tundra site (polygonal center) and the pond site during the winter periods of (a) 2007 and (b) 2008. Moreover, we depict the snow depth inferred from the AMSR-E snow-water equivalent product using a snow density of 190 $\mathrm{kg\,m^{-3}}$ for both periods. The diagrams at the bottom depict the temperatures observed at the surface and the ground of the investigated polygonal pond for the winter periods of (c) 2007 and (d) 2008.

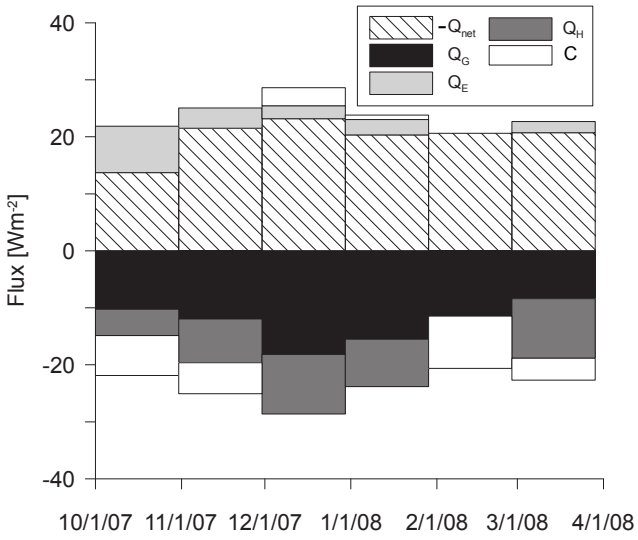

Figure 4.4: Monthly averages of energy balance components for the winter 2007/2008. Note that the net radiation Q_{net} is depicted with opposite sign.

snow cover. In 2007, the snow cover reaches a depth of about 0.15 m shortly after the first snow fall and remains almost constant until the end of the period. In 2008, the snow cover accumulation is much slower and ends up with a snow depth of about 0.1 m (Fig. 4.3). An even greater inter-annual variability the snow depth is observed at the polygonal pond, which in 2007 is covered by about 0.2 m of snow shortly after the first snow fall, whereas in 2008 almost no snow cover is measured until the end of this winter period (Fig. 4.3). On average, the observed differences in snow cover accumulation agree with the satellite observations (AMSR-E) (Fig. 4.3).

The net radiation budget of the first winter period is dominated by the long-wave radiation ΔQ_L, which in 2008 is about fifteen times larger than the net short-wave radiation (Tab. 4.2, Fig. 4.4). The incoming long-wave radiation steadily decreases from about 300 W m^{-2} to 180 W m^{-2}. This general trend is overlain by rapid variations in the range of 60 to 70 W m^{-2}, which are most likely associated with changes in cloudiness. In frequent situations, the outgoing and the incoming long-wave radiation are in quasi-balance ($Q_{net} \approx 0$), which is most likely caused by a dense cloud cover. The outgoing long-wave radiation follows the general trend of its incoming counterpart and decreases from about 315 W m^{-2} to 200 W m^{-2}, which corresponds to a surface temperature cooling from 0 to -24 °C. The surface temperature of 2008 appears to be slightly increased compared to 2007 (Tab. 4.2), which on average amounts to an increased radiative loss on the order of 5 W m^{-2} in 2008. The surface temperature follows to a large extent the short-term fluctuations of the incoming long-wave radiation. The observed fluctuations are on the order of 10 °C. The negative net radiation is partly balanced by the sensible heat flux Q_H, which is negative in both years. In both years, the average values of the sensible heat fluxes are small compared

to the ground heat fluxes, but show strong short-term variations on the order of 30 W m^{-2}. The observed fluctuations in the sensible heat fluxes largely follow the stepwise variations of the net radiation. Slightly positive sensible heat fluxes, that drag heat from the surface to the atmosphere, are observed occasionally. These events are strictly correlated to high values of down-welling thermal radiation and positive temperature gradients between the surface and the near-surface air temperature. High absolute values of the sensible heat flux are almost always associated with high wind speeds and strong turbulent exchange. The atmospheric stratification is mostly neutral ($\zeta \approx 0$), while stable stratification ($\zeta > 0$) only occur occasionally under clear-sky and calm conditions. Such stable stratifications are characterized by a very high snow heat flux, which compensates for the reduced sensible heat flux under stable conditions. The largest fraction of the negative radiation budget is balanced by the ground heat flux Q_G, which is predominately supplied by latent heat of freezing (Tab. 4.2). In the inter-annual comparison, the ground heat flux of 2008 is significantly larger than in 2007. This difference corresponds to the lower surface temperatures, the faster snow cover build-up and the slightly increased sensible heat flux of 2007 (Tab. 4.2). The observed inter-annual differences in the soil heat fluxes agree with the fact, that the active layer is completely frozen by the end of the early winter period in 2008, but not in 2007 (Fig. 4.3).
The most pronounced inter-annual differences in the ground heat budget are observed at the polygonal pond. According to the temperature profile measurements, we can estimate the ice cover thickness to be about 30 cm at the end of the early winter period in 2007. In 2008, the temperature measurements indicate that the water body is completely frozen down to a depth of 85 cm. Assuming an ice density of about 920 kg m^{-3}, this amount of ice corresponds to an average heat flux $Q_{G,p}$ of about -12 W m^{-2} in 2007 and about -34 W m^{-2} in 2008. Note, that these heat fluxes are only estimated according to the amount of frozen water, which does not contain the temperature change of the water body and the ground underneath. Hence, the true ground heat flux at the pond must be even larger. However, in the 2007, the estimated heat flux value at the freezing pond is in a good agreement with the net radiation $Q_{\mathrm{net,p}}$, which we measure directly at the surface of the water body (Tab. 4.2). It is evident, that such an energy balance agreement is not given in 2008, were the pond heat flux releases about 10 W m^{-2} more than is lost by radiation. Hence, additional heat transport, such as a positive sensible heat flux, may be involved at the pond surface.

4.4.2 Polar winter (December 01 - January 30)

The polar winter section features a highly negative net radiation budget in the range of -20 to -25 W m^{-2}. Due to polar night conditions, the radiation balance is only determined by thermal radiation. The largest fraction of the radiative loss is balanced by the ground heat flux Q_G, which is on the order of about -15 W m^{-2}. Compared to early winter, the sensible heat flux Q_H decreases and is now on the order of -10 W m^{-2}. The latent heat flux Q_E is significantly lowered and features a value of only 4 W m^{-2}.
The polar winter section is characterized by the absence of solar radiation during which the air temperatures reach their annual minimum of about -44 °C in winter 2007-2008

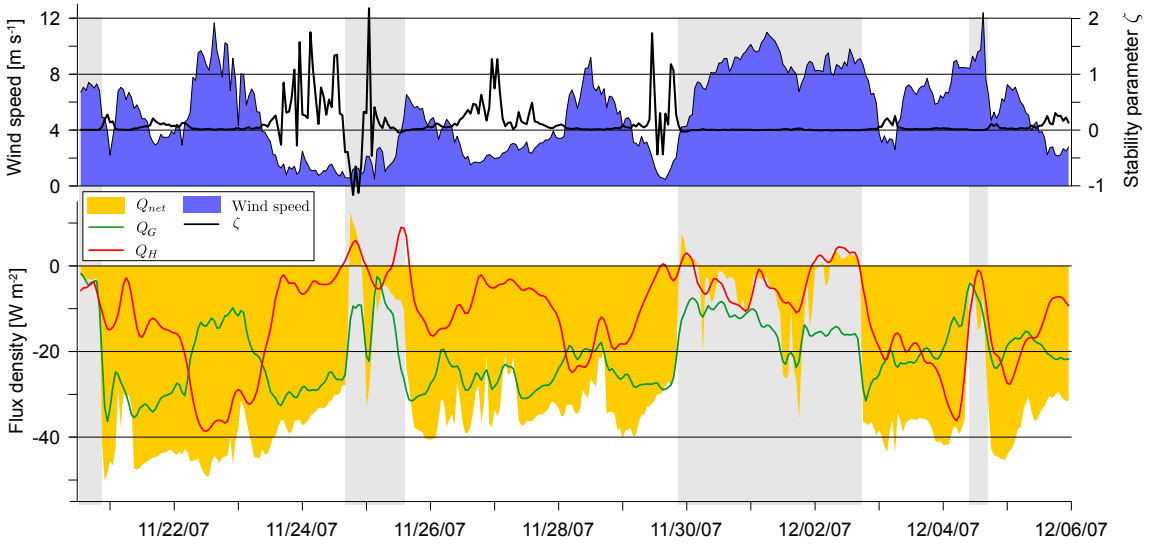

Figure 4.5: Exemplary measurements of Q_{net}, Q_H and Q_G during the transition from early to polar winter in 2007 (lower graph). Presumably overcast conditions are shaded. Measurements of the wind speed and the stability parameter ζ are depicted in the upper graph.

and −42 °C in winter 2008-2009. During winter 2007-2008, the snow cover remains almost constant featuring a depth of about 15 cm at the tundra surface and about 20 cm at the polygonal pond. A slightly different evolution of the snow cover is found for 2008-2009, when the snow depth remains between 10 and 15 cm at the tundra surface, whereas almost no snow cover is detected on the pond. For the winter 2007-2008, freezing continues from early winter into the polar night period. While the remaining unfrozen soil layer is already frozen after a few days, the pond remains partially unfrozen until the end of this section (Fig. 4.3). This delayed freezing process in 2007-2008 significantly influences the temperature at the bottom of the water body, which is about 15 °C warmer compared to the following year (Fig. 4.3).

The energy balance of the polar winter section is entirely governed by the long-wave budget ΔQ_L, which is significantly negative (Tab. 4.2). In both years, the incoming long-wave radiation shows frequent fluctuations according to changes between overcast and clear-sky conditions. The measured radiation values vary between 140 and 240 W m^{-2}. Conditions of constant incoming radiation typically last between two and three days. The surface temperatures and thus the outgoing thermal radiation show a strong variability in the range of −15 °C to −45 °C in both years, which corresponds to emitted radiative fluxes of about -150 and −250 W m^{-2}. The negative radiation budget is partly balanced by a slightly increased sensible heat flux compared to early winter (Tab. 4.2, Fig. 4.4). The largest fraction of the net radiation is balanced by the ground heat flux Q_G, which is mainly supplied by the release of sensible heat $Q_{G,\text{sensible}}$ (Tab. 4.2) that originates to about 85% from the first four meters of the soil column. Recalling the inter-annual difference in the

ground heat fluxes during the early winter section, the differences are now reversed. The ground heat flux of 2007 is now higher compared to 2008, which corresponds to a warmer soil in 2007 and therefore to a steeper soil temperature gradient.
An exemplary situation during the transition from the early winter to the polar night in 2007-2008 is depicted in Fig. 4.5. The example shows the typical stepwise pattern of the long-wave radiation budget, most likely caused by the influence of clouds. These large-scale variations are followed by the course of the sensible heat flux and the ground heat flux, which usually balances the largest fraction of the radiative losses. The turbulent heat flux becomes large ($Q_H \approx -30 W m^{-2}$) under clear-sky and windy conditions (wind speed $\approx 8 m s^{-1}$), as they occur around November 23 and December 4. The negative radiation budget is then primarily balanced by the sensible heat flux, which leads to a subsequent surface warming that essentially reduces the snow temperature gradient and thus the ground heat flux (compare Fig. 4.5). On rare occasions, the net radiation is found to be positive, which can only be associated with the influx of warm air masses that are warmer than the surface and lead to slightly positive sensible heat fluxes (Fig. 4.5). During one of these situations, we can observe the development of a slightly unstable stratification ($\zeta < 0$) around November 25 (Fig. 4.5). This situation is due to a precedent long-lasting period of calm conditions featuring stable stratifications and high radiative losses, which most likely cool the atmosphere. The sudden influx of warm air, which is indicated by the rapidly increasing net radiation to positive values heats up the surface. This consequently leads to a positive near-surface temperature gradient and the short-time development of unstable conditions. The unstable stratification breaks down as the net radiation falls back to negative values (Fig. 4.5).
The largest inter-annual differences in the ground heat budget are again observed at the investigated pond (Tab. 4.2), which in 2007-2008 is finally frozen by the end of the polar winter. Similar to the ground heat flux Q_G, the pond heat flux $Q_{G,p}$ is now higher in 2007-2008 than in 2008-2009. We also observe that in both years the released energy at the pond $Q_{G,p}$ is larger than the radiative losses $Q_{\mathrm{net,p}}$, which indicates that amplified turbulent sensible heat fluxes might occur at the surface of the frozen water body similar to the early winter period. Compared to the ground heat flux at the tundra surface Q_G, the pond heat flux is higher by a factor of about two.

4.4.3 Late winter (February 01 - March 30)

The energy balance of the late winter section is still characterized by negative net radiation Q_{net} of about -15 W m^{-2}, which is still significantly lower compared to the following spring period, described in the first part of this study. This is due to the fact that the net radiation budget steeply increases during this and the following period. The ground heat flux Q_G features about -5 W m^{-2} and loses its dominant role in balancing the radiation budget. The largest fraction of radiative losses is now balanced by a further increased sensible heat flux Q_H, which is on the order of -10 W m^{-2}. The modeled latent heat flux Q_E remains small at about 3 W m^{-2}.
The synoptic conditions are determined by the end of the polar night and increasing air

temperatures from about -35 to −5 °C. The snow depth in 2008 slightly increases of about 5 to 10 cm and reaches its annual maximum of 25 to 30 cm.
The average net radiation budget is still negative and reaches values as low as −40 W m^{-2}, while positive fluxes can exceed 20 W m^{-2} (Fig. 4.6). Positive net radiation values frequently occur within a pronounced diurnal cycle towards the end of this period. The upwelling long wave radiation ranges from 160 and 300 W m^{-2}, which corresponds to surface temperatures of -40 and −3 °C. The sensible heat flux is significantly more negative compared to the polar winter period and balances about 70% of the negative radiation budget, while the ground heat flux loses its dominant role. This corresponds to the evolution of a strong temperature gradient in the atmospheric boundary layer, which frequently exceeds values of −3 °C with an average gradient of about −1 °C (Tab. 4.2). The sensible heat flux features a diurnal cycle towards the end of the later winter period and ranges from -40 W m^{-2} to 5 W m^{-2} (Fig. 4.6). Positive sensible heat fluxes are usually observed during local noon, when the net radiation is positive due to high values of incoming solar radiation. The atmospheric stratification is essentially neutral during the first half of the late winter section, which corresponds to high wind speeds (Fig. 4.6). Within the course of the late winter period, the stability parameter ζ indicates frequent changes between stable and unstable stratifications (Fig. 4.6). The ground heat flux is essentially supplied by sensible heat from the deep soil layers. About 85% of the released heat originates from soil cooling down to a depth of 7 m. A more detailed look at the ground heat flux reveals more frequent positive heat fluxes towards the end of the period, which are usually associated with strongly negative sensible heat fluxes (Fig. 4.6). This indicates that at the end of the entire winter period the initial warming of the ground is mainly supplied by sensible heat fluxes from the atmosphere. These observations are in good agreement with heat fluxes measured in the following spring period, which are described in the first part of this study.
Significant spatial differences of the energy balance are still observed between the polygonal pond and the tundra site. The ground heat flux at the polygonal pond $Q_{G,p}$ is significantly increased compared to the tundra ground heat flux Q_G, which corresponds to the more negative radiation budget at the pond $Q_{net,p}$ (Tab. 4.2). This indicates that the polygonal pond most likely features slightly higher surface temperatures. If we assume the surface albedo at the snow covered tundra to be similar to the snow-covered pond, the surface at the pond would be about 1 °C warmer, according to the increased ground heat flux.

4.4.4 Controlling factors of surface temperature

The surface temperature T_{surf} is a direct result of the surface energy balance. It is therefore worthwhile to give an insight into its determining factors. We can see in Fig. 4.7, that the surface temperature variations are primarily determined by the incoming thermal radiation, while other factors, such as wind speed only have a secondary impact. Fig. 4.7 also shows that the impact of wind on the surface temperature is highest during low values of incoming long-wave radiation. This relation is explained by the fact, that the surface cools down strongest under clear-sky conditions when the turbulent heat transport from the atmosphere

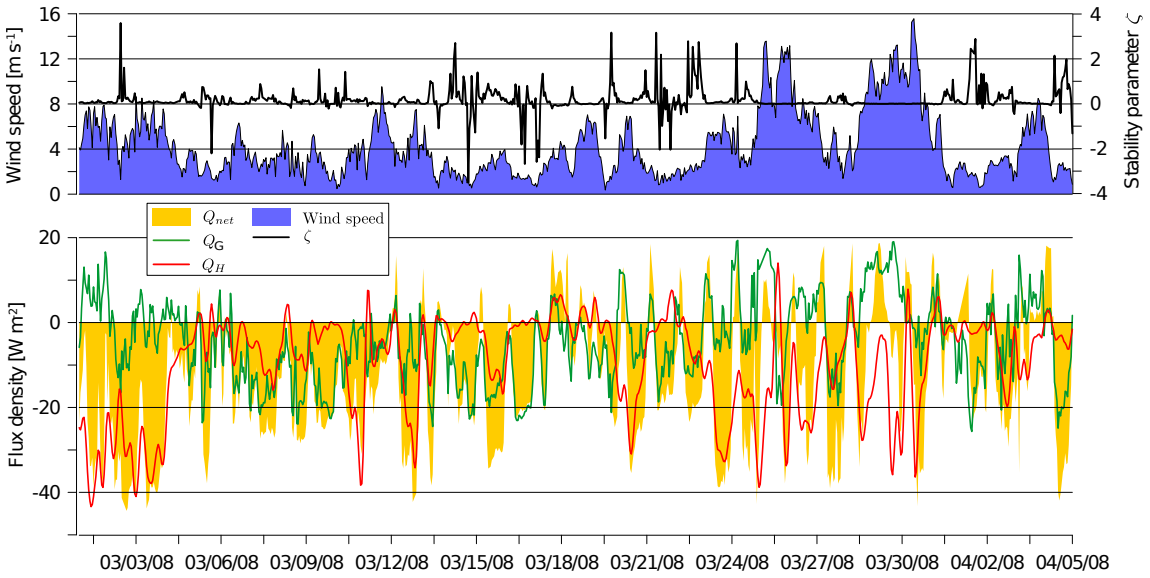

Figure 4.6: Measurements of Q_{net}, Q_H and Q_G during the late winter in 2008 (lower graph). The wind speed and the stability parameter ζ are depicted in the upper graph.

to the surface is limited by the absence of wind. This describes the typical situation of a near-surface temperature inversion under a stable atmospheric stratification ($\zeta > 0$), which leads to pronounced surface cooling. However, such conditions are observed only occasionally, since wind-induced turbulent mixing dominates during the polar night (Fig. 4.7), so that the formation of stable stratifications ($\zeta > 0$) is essentially limited.

4.5 Discussion

4.5.1 The winter time energy balance characteristics

According to our measurements, the surface energy balance during winter is predominately characterized by (i) the long-wave radiation budget, (ii) the ground heat flux and (iii) to a minor extent by the atmospheric sensible heat flux. The latent heat flux is found to be almost negligible.

(i) The radiation budget of the considered winter period is largely determined by the long-wave radiation, as it mostly falls within the polar night, while the high albedo of the snow cover limits the role of the short-wave radiation at the beginning and the end of the period (Tab. 4.2). The net long-wave radiation fluctuates strongly between almost zero and highly negative values of up to -50 W m^{-2}. The fluctuations are largely caused by fast changes of the incoming long-wave radiation, which most likely can be attributed to the presence or absence of a cloud cover (Shupe and Intrieri 2004). The incoming long-wave radiation is the determining factor for the surface

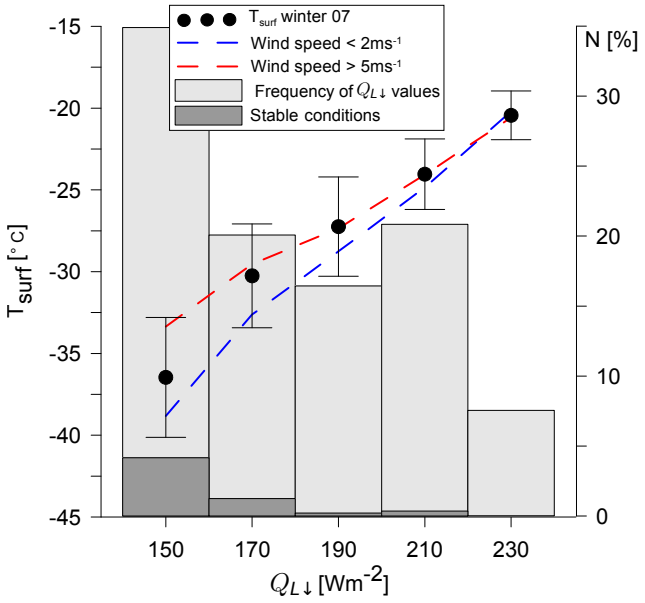

Figure 4.7: The surface temperature T_{surf} in dependence to the incoming long-wave radiation $Q_{L\downarrow}$ and different wind speeds. The first histogram (light grey) indicates the frequency of observations that feature the displayed classes of incoming long-wave radiation. The second histogram (dark grey) shows the occurrence of stable atmospheric stratification under the different $Q_{L\downarrow}$ conditions.

temperature, as it sets the general range within which the surface temperature can adjust depending on the other components of the energy balance (Fig. 4.7).

(ii) The ground heat flux is of outstanding importance for the surface energy balance during the winter periods, since it is the main balancing factor of the radiative losses. It originates from both the refreezing of the active layer and the cooling of the soil, with both contributing about 50% to the entire flux. Hereby the refreezing of the active layer strongly dominates until about the beginning of December. Afterwards the ground heat flux is entirely supplied by soil cooling up to a depth of 12 m. Strong inter-annual differences in the ground heat flux are observed particularly during the early winter section (Tab. 4.2), with reduced heat fluxes and a delayed refreezing in 2007. This is most likely due to an approximately doubled snow depth in this year (Fig. 4.3). For similar surface temperatures and a soil-snow interface temperature close to 0 °C due to refreezing processes, this would exactly correspond to a reduced heat flux by a factor of two, which has been observed in measurements (Tab. 4.2). When the active layer is refrozen, the snow still limits the release of heat from the soil due to the difference in the thermal conductivity compared to the soil. Hereby, the thermal conductivity of snow is by a factor of four to eight lower than the thermal conductivity of frozen peat (Tab. 4.1). However, the delayed refreezing recorded in

2007 induces higher soil temperatures at the beginning of the polar winter period, which leads to slightly higher ground heat fluxes despite of the higher snow cover in 2007. Therefore, the release of heat occurs over a longer period in 2007, while it is more concentrated at the beginning of the winter in 2008. Nevertheless, almost similar soil temperatures are reached at the end of the winter period in both years. Towards the end of the winter period, the ground heat flux stagnates as the upper soil layers already begin to warm up, which cancels out the still negative heat flux of deep soil layers.

(iii) While the interplay between the net radiation, the ground heat flux and the sensible heat flux can be complex (Fig. 4.5), the magnitude of the average sensible heat flux is significantly smaller than the ground heat flux. The highest values of sensible heat fluxes are observed at the end of the winter season. During the entire winter period the observed average sensible heat flux of about -8 W m^{-2} amounts to a cooling of an air column of 1000 m height by about 30 °C over a period of 6 months. This matches the order of magnitude of the observed near-surface temperature cooling, which is also on the order of 30 °C (compare Tab. 4.2). In addition, the well mixed boundary layer with predominantely neutral stratifications suggests a prominent role of the sensible heat flux for the cooling of the near surface atmosphere. It must be emphasized, that the contribution of the wintertime sensible heat flux to the surface energy balance is by a factor of two smaller than values reported for arctic-oceanic conditions on Svalbard (Westermann et al. 2009), but of similar magnitude as values reported from measurements on sea-ice at the Arctic Ocean (Persson et al. 2002).

4.5.2 Implications for large–scale modeling

Three major implications of this study for permafrost modeling can be identified. In particular, these implications are given by (I) the relevance of the ground heat flux in the surface energy budget and its impact on the atmospheric conditions near the surface, (II) the importance of parameters such as snow cover, cloud cover and soil properties for the thermal permafrost conditions and (III) the spatial and temporal variability of the surface energy balance with respect to the freeze and thaw dynamics.

(I) Due to the magnitude of the ground heat flux, it must be considered a critical factor for the formation of the surface temperature, which affects both the radiation budget and the turbulent land-atmosphere exchange. Thus, an adequate representation of the ground heat flux is crucial to correctly model the energy turnover at the surface during the long-lasting winter period in the Arctic. This is especially true in permafrost regions, where the refreezing active layer represents a sustained energy supply. Nevertheless, strongly simplified representations of the soil developed for non-arctic regions are commonplace in GCMs. An example is the “European Centre/Hamburg” model (ECHAM 5) in which freezing of soil water is not accounted for (Bartsch et al. 2007). A realistic representation of the ground heat flux and thus the winter surface energy budget in permafrost regions seems unconceivable in such a model. It has

been demonstrated in several model experiments that large-scale changes in the soil parameterization essentially affect the performance of climate models (Pitman 2003). For a regional climate model, Rinke et al. (2008) revealed that introducing an additional organic layer at the top of arctic tundra soils significantly impacts the surface energy balance, as well as the larger-scale atmospheric circulation. Similar is reported for global climate models by Lawrence and Slater (2008), who found that near-surface air temperatures at high latitudes significantly increased after the incorporation of an organic soil layer. Peters-Lidard et al. (1998) outlined the importance of the soil parametrization for the surface energy balance in soil-vegetation-atmosphere-transfer schemes (SVATS), as they are implemented in global climate models. An essential improvement in the boundary layer representation in weather forecast models has been achieved by the incorporation of soil freezing (Viterbo et al. 1999), which has also been demonstrated by Cox et al. (1999) to affect the performance of GCMs. Energy balance measurements during the polar winter over sea-ice revealed a significant difference between near surface temperature observations and values retrieved from the "European Centre for Medium Range Weather Forecasts" ECMWF model, which were found to be related to a wrong representation of the thermal (ground) ice conditions (Beesley et al. 2000). According to the reported sensitivity of climate models, there is evidence that the performance of climate models in arctic regions is essentially affected by the representation of the ground heat flux and hence by permafrost itself.

(II) The winter time ground heat flux is of essential importance for the thermal state of permafrost. The crucial factors determining the wintertime surface temperatures and thus the ground heat flux are the radiation budget and the snow cover. The radiation budget is largely affected by the presence of clouds and to a minor extent by the characteristics of the atmospheric turbulence (sensible heat flux). Moreover, the ground heat flux is essentially limited by the isolating snow layer, as mentioned above. The impact of the low thermal conductivity of snow on the ground heat flux is largest for steep temperature gradients across the snow cover as they occur during clear-sky conditions. The impact of the snow cover on the thermal conditions of the permafrost has been demonstrated by Goodrich (1982), who found significantly higher average soil temperatures compared to the average surface temperature, depending on snow depth and the build-up dynamics of the snow cover. This positive temperature shift between soil and surface temperatures is observed to be on the order of 4 °C at the study site. Towards the beginning of spring, the increasing temperatures at the uppermost snow and soil layers are observed in conjunction with pronounced sensible heat fluxes. This suggests that warm air masses rather trigger initial snow and soil warming than the short-wave radiation does, which is largely reflected due to the high albedo of the snow cover. The winter soil temperatures are therefore essentially affected by larger-scale atmospheric circulation processes, such as the influx of cyclones or the annual dynamics of the Siberian High. Predictions on the future state of permafrost must necessarily aim for appropriate incorporation of

these determining factors of the ground thermal regime.

(III) The freeze and thaw dynamics are of outstanding importance, if large-scale model schemes are intended to account for complex biochemical processes, such as microbial decomposition of organic material in permafrost soils (Davidson and Janssens 2006). During the refreezing process, the soil and water temperatures are sustained at 0 °C and liquid water is available until the soil or water body is completely frozen. Hence, the time span favorable for biological activity is determined by the duration of the refreezing process. Our results clearly reveal a high spatial and temporal variability of the refreezing characteristics and the permafrost temperatures. In 2007, the soil refreezing is about half a month delayed compared to 2008, whereas the investigated pond requires three months longer for being completely frozen (Fig. 4.3). This indicates that the production time of greenhouse gases especially at shallow water bodies features a significant inter-annual variability. This in turn may induce high inter-annual variabilities in the spring-time methane emission, when the ice cover at the ponds begins to thaw. The importance of such high-arctic water bodies for the atmospheric methane budget has been demonstrated by Walter et al. (2006) and Walter et al. (2007). Furthermore, Wagner et al. (2007) showed that even under frozen conditions microbial methane production can occur and already slight warming of the permafrost temperatures can lead to a significant increases in the microbial activity. Owing to these reports and our observations, it is intriguing that already small variations in the snow cover build-up essentially affect the time of potential methane production. These findings have strong implications for model schemes as introduced by Khvorostyanov et al. (2008), who aim to include biochemical processes in permafrost regions on larger scales. In this regard, it might be important to account for micro-scale variabilities, such as the distribution and depth of small water bodies, in the parametrization of such models. Moreover, the heat budget of such shallow water bodies responds intensively to temporal variabilities of the surface energy balance. It is therefore desirable to further investigate permafrost regions characterized by shallow water bodies. The correct representation of such sensitive processes in climate models requires the realistic reproduction of the control parameters, such as snow fall and cloudiness, which is maybe the largest challenge in the current model development.

4.6 Conclusions

Based on the results of the first and the second part of this study, we conclude with an overview of the main characteristics of the surface energy balance in the context of the annual cycle. In the following, we summarize the role of the different energy balance components for the annual heat budget and their main controlling factors.

- During the entire annual cycle, the surface energy budget is determined by the radiation balance. The net radiation essentially depends on the seasonality of the shortwave radiation budget, the presence or absence of the snow cover and the the cloudiness. The snow cover has its greatest impact over 4 months from the end of the polar night until snow melt, when the high snow albedo significantly reduces the net shortwave radiation. Clouds are generally found to reduce the net radiation by about 50% during the snow-free season, while they almost prevent radiative losses during winter.

- The turbulent heat fluxes have their largest impact on the surface energy budget during the snow-free period, when they balance about 70% of the net radiation. The latent heat flux is a factor of two higher than the sensible heat flux, so that the average Bowen ratio yields 0.5. It must be emphasized that the latent heat flux is largely in balance with the observed precipitation rates, which suggests a regionally closed water cycle between the atmosphere and the tundra surface during the summer months. During the winter period, the latent heat flux is almost negligible and so its sublimation at the snow cover. The sensible heat flux reaches its largest relative contribution to the surface energy balance during the late winter period, when it balances almost 70% of the radiative losses. This indicates that warming after the winter period is influenced by the influx of warm air. Furthermore, it is worthwhile to note that the lower atmosphere is well mixed during a major part of the winter season and stable stratifications are very rare.

- The ground heat flux always constitutes a significant component in the surface energy balance, with relative contributions of about 20% during summer and 60% during polar winter. During the summer months, the internal heat storage of the ground is characterized to about 60% by active layer thawing, whereas 40% are used for warming of the soil temperatures. The refreezing period, which can last from the end of September until the beginning of December, is mainly controlled by the radiation balance. At that time, clouds and the snow cover have their largest impact on the ground thermal regime as they significantly influence the duration of the refreezing period. It is important to recall that during most of the winter period the ground heat flux sustains the largest fraction of radiative losses, which helps to prevent the development of atmospheric inversions near the surface. As the ground heat flux during winter essentially determines the permafrost temperatures, it also strongly influences the soil temperature gradient in summer and thus the sensible ground heat storage. Hence, a considerable fraction of the surface energy balance during the summer months is directly affected by the magnitude of the ground heat flux of the previous winter. This again corroborates the importance of the heat storage capacities of the permafrost soils in the annual cycle. The heat storage capacity of the tundra can be further increased by the presence of water bodies, which can be remarkable even for small water bodies, such as ponds.

We conclude that the correct representation of the ground heat flux in climate models is not only an important issue for permafrost modeling, but also for the correct representation

of the surface energy balance of large areas in the Arctic itself. The development of soil parameterizations, that can account for permafrost, could therefore help to improve the representation of the lower boundary conditions of regional and global climate models.

Bibliography

M. Allard and J.N. Kasper. Temperature conditions for ice-wedge cracking: field measurements from Salluit, Northern Quebec. In *Permafrost, Proceedings, 7th International Conference, Yellowknife, Canada, Centre dâetudes nordiques, Universite Laval, Collection Nordicana*, volume 57, pages 5–11, 1998.

F. Are and E. Reimnitz. An overview of the Lena River Delta setting: geology, tectonics, geomorphology, and hydrology. *Journal of Coastal Research*, 16(4):1083–1093, 2000.

VI Astakhov, FA Kaplyanskaya, and VD Tarnogradsky. Pleistocene permafrost of West Siberia as a deformable glacier bed. *Permafrost and Periglacial Processes*, 7(2):165–191, 1996.

A. Bartsch, R.A. Kidd, W. Wagner, and Z. Bartalis. Temporal and spatial variability of the beginning and end of daily spring freeze/thaw cycles derived from scatterometer data. *Remote Sensing of Environment*, 106(3):360–374, 2007.

W.G.M. Bastiaanssen, M. Menenti, R.A. Feddes, and A.A.M. Holtslag. A remote sensing surface energy balance algorithm for land (SEBAL). 1. Formulation. *Journal of Hydrology*, 212:198–212, 1998.

F. Becker, P. Ramanantsizehena, and M.P. Stoll. Angular variation of the bidirectional reflectance of bare soils in the thermal infrared band. *Applied optics*, 24(3):365–375, 1985.

J. Beesley, CS Bretherton, C. Jakob, EL Andreas, JM Intrieri, and TA Uttal. A comparison of cloud and boundary layer variables in the ECMWF forecast model with observations at Surface Heat Budget of the Arctic Ocean(SHEBA) ice camp. *Journal of Geophysical Research*, 105(D10):12337–12349, 2000.

J. Boike and K. Roth. Time domain reflectometry as a field method for measuring water content and soil water electrical conductivity at a continuous permafrost site. *Permafrost and Periglacial Processes*, 8(4):359–370, 1998.

J. Boike, K. Roth, and P.P. Overduin. Thermal and hydrologic dynamics of the active layer at a continuous permafrost site (Taymyr Peninsula, Siberia). *Water Resources Research*, 34(3):355–363, 1998.

J. Boike, K. Roth, and O. Ippisch. Seasonal snow cover on frozen ground: Energy balance calculations of a permafrost site near Ny-Alesund, Spitsbergen. *Journal of Geophysical Research-Atmospheres*, 108(D2):8163–8173, 2003.

J. Boike, C. Wille, and A. Abnizova. Climatology and summer energy and water balance of polygonal tundra in the Lena River Delta, Siberia. *Journal of Geophysical Research-Biogeosciences*, 113(G3):G03025, 2008. doi: 10.1029/2007JG000540.

JA Brotzge and CE Duchon. A field comparison among a domeless net radiometer, two four-component net radiometers, and a domed net radiometer. *Journal of Atmospheric and Oceanic Technology*, 17:12, 2000.

J. Brown and V.E. Romanovsky. Report from the International Permafrost Association: state of permafrost in the first decade of the 21 st century. *Permafrost and Periglacial Processes*, 19(2), 2008.

J. Brown, OJ Ferrians Jr, JA Heginbottom, and ES Melnikov. Circum-Arctic map of permafrost and ground-ice conditions. *US Geological Survey Circum-Pacific Map*, 1997.

N.A. Brunsell and R.R. Gillies. Scale issues in land–atmosphere interactions: implications for remote sensing of the surface energy balance. *Agricultural and Forest Meteorology*, 117(3-4):203–221, 2003.

T.V. Callaghan, L.O. Björn, Y. Chernov, T. Chapin, T.R. Christensen, B. Huntley, R.A. Ims, M. Johansson, D. Jolly, S. Jonasson, et al. Effects of changes in climate on landscape and regional processes, and feedbacks to the climate system. *AMBIO: A Journal of the Human Environment*, 33(7):459–468, 2004.

TR Christensen and P. Cox. Response of methane emission from Arctic tundra to climatic change: Results from a model simulation. *Tellus. Series B: Chemical and Physical Meteorology*, 47(3):301–309, 1995.

T.R. Christensen, A. Ekberg, L. Ström, M. Mastepanov, N. Panikov, M. Öquist, B.H. Svensson, H. Nykänen, P.J. Martikainen, and H. Oskarsson. Factors controlling large scale variations in methane emissions from wetlands. *Geophys. Res. Lett*, 30(7):1414, 2003.

J.C. Comiso. A rapidly declining perennial sea ice cover in the Arctic. *Geophysical Research Letters*, 29(20):1956, 2002. doi: 10.1029/2002GL015650.

J.C. Comiso. Warming trends in the Arctic from clear sky satellite observations. *Journal of Climate*, 16(21):3498–3510, 2003.

J.C. Comiso. Arctic warming signals from satellite observations. *Weather*, 61(3), 2006.

PM Cox, RA Betts, CB Bunton, RLH Essery, PR Rowntree, and J. Smith. The impact of new land surface physics on the GCM simulation of climate and climate sensitivity. *Climate Dynamics*, 15(3):183–203, 1999.

J.A. Curry, W.B. Rossow, D. Randall, and J.L. Schramm. Overview of Arctic cloud and radiation characteristics. *Journal of Climate*, 9(8):1731–1764, 1996.

E.A. Davidson and I.A. Janssens. Temperature sensitivity of soil carbon decomposition and feedbacks to climate change. *Nature*, 440(7081):165–173, 2006.

C. Delire, S. Levis, G. Bonan, J. Foley, M. Coe, and S. Vavrus. Comparison of the climate simulated by the CCM3 coupled to two different land-surface models. *Climate Dynamics*, 19(8):657–669, 2002.

C.R. Duguay, T. Zhang, D.W. Leverington, and V.E. Romanovsky. Satellite remote sensing of permafrost and seasonally frozen ground. *Remote Sensing in Northern Hydrology: Measuring Environmental Change*, pages 91–118, 2005.

ESA. The lena river delta. (http://earth.eo.esa.int/cgi-bin/satimgsql.pl?show_url=1471&startframe=0), 2006.

W. Eugster, W.R. Rouse, R.A. Pielke Sr, J.P. McFadden, D.D. Baldocchi, T.G.F. Kittel, F.S. Chapin, G.E. Liston, P.L. Vidale, E. Vaganov, and S. Chambers. Land–atmosphere energy exchange in Arctic tundra and boreal forest: available data and feedbacks to climate. *Global Change Biology*, 6(1):84–115, 2000.

T. Foken. *Micrometeorology*. Springer, 2008.

T. Foken and B. Wichura. Tools for quality assessment of surface-based flux measurements. *Agricultural and Forest Meteorology*, 78(1-2):83–105, 1996.

T. Foken, M. Göckede, M. Mauder, L. Mahrt, B.D. Amiro, and J.W. Munger. *Post-field data quality control, in: Handbook of Micrometeorology: A Guide for Surface Flux Measurement and Analysis*. Kluwer, 2004.

D. Fortier and M. Allard. Frost-cracking conditions, Bylot Island, Eastern Canadian Arctic Archipelago. *Permafrost and Periglacial Processes*, 16(2):145–161, 2005.

J.L. Foster, C. Sun, J.P. Walker, R. Kelly, A. Chang, J. Dong, and H. Powell. Quantifying the uncertainty in passive microwave snow water equivalent observations. *Remote Sensing of environment*, 94(2):187–203, 2005.

H.M. French. *The periglacial environment, Third edition*. Wiley, 2007.

M. Friedl. Forward and inverse modeling of land surface energy balance using surface temperature measurements. *Remote Sensing of Environment*, 79(2):344–354, 2002.

MA. Friedl. Relationships among remotely sensed data, surface energy balance, and area-averaged fluxes over partially vegetated land surfaces. *Journal of Applied Meteorology*, 35(11):2091–2103, 1996.

JC Fyfe, GJ Boer, and GM Flato. Arctic and Antarctic oscillations and their projected changes under global warming. *Geophysical Research Letters*, 26(11):1601–1604, 1999.

JR Garratt. *The atmospheric boundary layer*. Cambridge Univ Pr, 1994.

LE Goodrich. The influence of snow cover on the ground thermal regime. *Canadian Geotechnical Journal*, 19(4):421–432, 1982.

N.F. Grigoriev. *The temperature of permafrost in the Lena delta basin – deposit conditions and properties of the permafrost in Yakutia*, chapter 2, pages 97–101. Yakutsk, 1960. in Russian.

G. Grosse, L. Schirrmeister, V.V. Kunitsky, and H.W. Hubberten. The use of CORONA images in remote sensing of periglacial geomorphology: an illustration from the NE Siberian coast. *Permafrost and periglacial processes*, 16(2):163–172, 2005.

Y. Guo and P.H. Schuepp. An Analysis of the Effect of Local Heat Advection on Evaporation over Wet and Dry Surface Strips. *Journal of Climate*, 7(5):641–652, 1994.

W.J. Gutowski Jr, H. Wei, C.J. Vörösmarty, and B.M. Fekete. Influence of Arctic wetlands on Arctic atmospheric circulation. *Journal of Climate*, 20(16):4243–4254, 2007.

S. Hachem, M. Allard, and C. Duguay. A new permafrost map of Quebec-Labrador derived from near-surface temperature data of the moderate resolution imaging spectroradiometer (MODIS). *Proceedings, NICOP (Vol. I)*, pages 591–596, 2008.

F.G. Hall, K.F. Huemmrich, S.J. Goetz, P.J. Sellers, and J.E. Nickeson. Satellite remote sensing of surface energy balance: success, failures, and unresolved issues in FIFE. *Journal of geophysical research*, 97(D17):19061–19089, 1992.

J. Hansen, R. Ruedy, M. Sato, M. Imhoff, W. Lawrence, D. Easterling, T. Peterson, and T. Karl. A closer look at United States and global surface temperature change. *Journal of Geophysical Research-Atmospheres*, 106(D20):23947–23963, 2001.

SA Harris, HM French, JA Heginbottom, GH Johnston, B. Ladanyi, DC Sego, and RO Van Everdingen. *Glossary of permafrost and related ground-ice terms*. NRCC, 1988.

K.M. Hinkel, W.R. Eisner, J.G. Bockheim, F.E. Nelson, K.M. Peterson, and X. Dai. Spatial extent, age, and carbon stocks in drained thaw lake basins on the Barrow Peninsula, Alaska. *Arctic, Antarctic, and Alpine Research*, 35(3):291–300, 2003.

L.D. Hinzman, N.D. Bettez, W.R. Bolton, F.S. Chapin, M.B. Dyurgerov, C.L. Fastie, B. Griffith, R.D. Hollister, A. Hope, H.P. Huntington, et al. Evidence and implications of recent climate change in northern Alaska and other arctic regions. *Climatic Change*, 72(3):251–298, 2005.

L.D. Hinzman, L.A. Viereck, P.C. Adams, V.E. Romanovsky, and K. Yoshikawa. Climate and permafrost dynamics of the Alaskan boreal forest. *Alaskas Changing Boreal Forest*, pages 39–61, 2006.

SE Hobbie, JP Schimel, SE Trumbore, and JR Randerson. Controls over carbon storage and turnover in high-latitude soils. *Global Change Biology*, 6(Supplement 1):196–210, 2000.

ULF Høgstrøm. Non-dimensional wind and temperature profiles in the atmospheric surface layer: A re-evaluation. *Boundary-Layer Meteorology*, 42(1):55–78, 1988.

MM Holland and CM Bitz. Polar amplification of climate change in coupled models. *Climate Dynamics*, 21(3):221–232, 2003.

N.D.S Huband and J.L. Monteith. Radiative surface temperature and energy balance of a wheat canopy. *Boundary-Layer Meteorology*, 36(1):1–17, 1986.

K.S. Humes, W.P. Kustas, M.S. Moran, W.D. Nichols, and M.A. Weltz. Variability of emissivity and surface temperature over a sparsely vegetated surface. *Water Resources Research*, 30(5):1299–1310, 1994.

Y. Iijima, K. Masuda, and T. Ohata. Snow disappearance in Eastern Siberia and its relationship to atmospheric influences. *International Journal of Climatology*, 27(2):169–178, 2007.

JM Intrieri, MD Shupe, T. Uttal, and BJ McCarty. An annual cycle of Arctic cloud characteristics observed by radar and lidar at SHEBA. *Journal of Geophysical Research-Oceans*, 107(C10):8030, 2002.

O.M. Johannessen, L. Bengtsson, M.W. Miles, S.I. Kuzmina, V.A. Semenov, G.V. Alekseev, A.P. Nagurnyi, V.F. Zakharov, L.P. Bobylev, L.H. Pettersson, et al. Arctic climate change: observed and modelled temperature and sea-ice variability. *Tellus A*, 56(4): 328–341, 2004.

J.O. Kaplan, NH Bigelow, I.C. Prentice, S.P. Harrison, P.J. Bartlein, TR Christensen, W. Cramer, NV Matveyeva, AD McGuire, DF Murray, et al. Climate change and Arctic ecosystems: 2. Modeling, paleodata-model comparisons, and future projections. *J. Geophys. Res*, 108(D19):8171, 2003.

R.E.J. Kelly, A.T.C. Chang, J.L. Foster, and M. Tedesco. Amsr-e/aqua 5-day 3 global snow water equivalent ease-grids v002. Boulder, Colorado USA: National Snow and Ice Data Center. Digital media, 2004. [data used from 2007-2009].

DV Khvorostyanov, G. Krinner, P. Ciais, M. Heimann, and SA Zimov. Vulnerability of permafrost carbon to global warming. Part I: model description and role of heat generated by organic matter decomposition. *Tellus B*, 60(2):250–264, 2008.

W. Kohsiek, C. Liebethal, T. Foken, R. Vogt, S.P. Oncley, C. Bernhofer, and H.A.R. Debruin. The Energy Balance Experiment EBEX-2000. Part III: Behaviour and quality of the radiation measurements. *Boundary-Layer Meteorology*, 123(1):55–75, 2007.

G. Krinner. Impact of lakes and wetlands on boreal climate. *Journal of Geophysical Research-Atmospheres*, 108(D16):4520, 2003.

G. Krinner and J. Boike. A study of the large-scale climatic effects of a possible disappearance of high-latitude inland water surfaces during the 21st century. *Boreal Environment Research*, 15:203–217, 2010.

L. Kutzbach, D. Wagner, and E.M. Pfeiffer. Effect of microrelief and vegetation on methane emission from wet polygonal tundra, Lena Delta, Northern Siberia. *Biogeochemistry*, 69 (3):341–362, 2004.

L. Kutzbach, C. Wille, and E.M. Pfeiffer. The exchange of carbon dioxide between wet arctic tundra and the atmosphere at the Lena River Delta, Northern Siberia. *Biogeosciences*, 4:869–890, 2007.

J. Labed and MP Stoll. Angular variation of land surface spectral emissivity in the thermal infrared: laboratory investigations on bare soils. *International Journal of Remote Sensing*, 12(11):2299–2310, 1991.

A.H. Lachenbruch. *Mechanics of thermal contraction cracks and ice-wedge polygons in permafrost*. Geological Society of America New York, 1962.

AH Lachenbruch. Contraction theory of ice-wedge polygons: A qualitative discussion. In *International Permafrost Conference, Proceedings*, pages 63–71, 1966.

T.E. Laing, K.M. Ruhland, and J.P. Smol. Past environmental and climatic changes related to tree-line shifts inferred from fossil diatoms from a lake near the Lena River Delta, Siberia. *The Holocene*, 9(5):547, 1999.

M. Langer, S. Westermann, S.Muster, K. Piel, and J. Boike. Permafrost and surface energy balance of a polygonal tundra site in northern Siberia - Part I: spring-fall. *submitted*, 2010a.

M. Langer, S. Westermann, S.Muster, K. Piel, and J. Boike. Permafrost and surface energy balance of a polygonal tundra site in northern Siberia - Part II: Winter. *in preparation*, 2010b.

Moritz Langer, Sebastian Westermann, and Julia Boike. Spatial and temporal variations of summer surface temperatures of wet polygonal tundra in siberia - implications for modis lst based permafrost monitoring. *Remote Sensing of Environment*, 114(9):2059–2069, 2010c.

D.M. Lawrence and A.G. Slater. A projection of severe near-surface permafrost degradation during the 21st century. *Geophys. Res. Lett*, 32:L24401, 2005.

D.M. Lawrence and A.G. Slater. Incorporating organic soil into a global climate model. *Climate Dynamics*, 30(2):145–160, 2008.

D.M. Lawrence, A.G. Slater, V.E. Romanovsky, and D.J. Nicolsky. Sensitivity of a model projection of near-surface permafrost degradation to soil column depth and representation of soil organic matter. *J. Geophys. Res*, 113:F02011, 2008.

D.W. Leverington and C.R. Duguay. A neural network method to determine the presence or absence of permafrost near Mayo, Yukon Territory, Canada. *Permafrost and Periglacial Processes*, 8(2):205–215, 1998.

A.G. Lewkowicz. Evaluation of miniature temperature-loggers to monitor snowpack evolution at mountain permafrost sites, northwestern Canada. *Permafrost and Periglacial Processes*, 19(3):323–331, 2008.

J. Lüers and J. Bareiss. Direct near surface measurements of sensible heat fluxes in the arctic tundra applying eddy-covariance and laser scintillometry - The Arctic Turbulence Experiment 2006 on Svalbard (ARCTEX-2006). *submitted to Theoretical and Applied Climatology*, 2009.

A.H. Lynch, F.S. Chapin, L.D. Hinzman, W. Wu, E. Lilly, G. Vourlitis, and E. Kim. Surface energy balance on the arctic tundra: Measurements and models. *Journal of Climate*, 12 (8):2585–2606, 1999.

J.R. Mackay. Air temperature, snow cover, creep of frozen ground, and the time of ice-wedge cracking, western Arctic coast. *Can. J. Earth Sci*, 30(8):1720–1729, 1993.

L. Mahrt, J.I. MacPherson, and R. Desjardins. Observations of fluxes over heterogeneous surfaces. *Boundary-Layer Meteorology*, 67(4):345–367, 1994.

S. Marchenko, S. Hachem, V. Romanovsky, and C. Duguay. Permafrost and Active Layer Modeling in the Northern Eurasia using MODIS Land Surface Temperature as an input data. *Geophysical Research Abstracts*, 11:EGU2009–11077, 2009.

S. Martin and E.A. Munoz. Properties of the Arctic 2-meter air temperature field for 1979 to the present derived from a new gridded dataset. *Journal of Climate*, 10(6):1428–1440, 1997.

M. Mastepanov, C. Sigsgaard, E.J. Dlugokencky, S. Houweling, L. Ström, M.P. Tamstorf, and T.R. Christensen. Large tundra methane burst during onset of freezing. *Nature*, 456 (7222):628–630, 2008.

M. Mauder and T. Foken. *Documentation and instruction manual of the eddy covariance software package TK2*. Univ. of Bayreuth, Dept. of Mikrometeorology, 2004.

M. Mauder, C. Liebethal, M. Göckede, J.P. Leps, F. Beyrich, and T. Foken. Processing and quality control of flux data during LITFASS-2003. *Boundary-Layer Meteorology*, 121(1): 67–88, 2006.

M. Mauder, T. Foken, R. Clement, JA Elbers, W. Eugster, T. Grunwald, B. Heusinkveld, and O. Kolle. Quality control of CarboEurope flux data–Part II: Inter-comparison of eddy-covariance software. *Biogeosciences Discussions*, 4(6):4067–4099, 2007.

B. Mayer and A. Kylling. Technical note: The libRadtran software package for radiative transfer calculations–description and examples of use. *Atmos. Chem. Phys*, 5:1855–1877, 2005.

A.D. McGuire, F.S. Chapin, J.E. Walsh, and C. Wirth. Integrated Regional Changes in Arctic Climate Feedbacks: Implications for the Global Climate System. *Annual Review of Environment and Resources*, 31:61–91, 2006.

M. Minke, N. Donner, N. Karpov, P. de Klerk, and H. Joosten. Patterns in vegetation composition, surface height and thaw depth in polygon mires in the Yakutian Arctic (NE Siberia): a microtopographical characterisation of the active layer. *Permafrost and Periglacial Processes*, 20(4):357–368, 2009.

R.E. Moritz, C.M. Bitz, and E.J. Steig. Dynamics of recent climate change in the Arctic. *Science*, 297(5586):1497, 2002.

K. Mueller. Oberflächenstrukturen und Eigenschaften von Permafrostböden im nordsibirischen Lena-Delta. *Zeitschrift für Pflanzenernährung und Bodenkunde*, 160(4):497–503, 2007.

N. Neumann and P. Marsh. Local advection of sensible heat in the snowmelt landscape of Arctic tundra. *Hydrological Processes*, 12(10):1547–1560, 1998.

DJ Nicolsky, VE Romanovsky, VA Alexeev, and DM Lawrence. Improved modeling of permafrost dynamics in a GCM land-surface scheme. *Geophysical Research Letters*, 34 (8):L08501, 2007.

D.J. Nicolsky, V.E. Romanovsky, and G.G. Panteleev. Estimation of soil thermal properties using in-situ temperature measurements in the active layer and permafrost. *Cold Regions Science and Technology*, 55(1):120–129, 2009.

M. Nishihama, R. Wolfe, D. Solomon, F. Patt, J. Blanchette, A. Fleig, and E. Masuoka. MODIS level 1A Earth location: Algorithm theoretical basis document version 3.0. *SDST-092, MODIS Science Data Support Team*, 1997.

J.M. Norman and F. Becker. Terminology in thermal infrared remote sensing of natural surfaces. *Agricultural and Forest Meteorology*, 77(3-4):153–166, 1995.

TR Oke. *Boundary layer climates*. Methuen, 1987.

TE Osterkamp. The recent warming of permafrost in Alaska. *Global and Planetary Change*, 49(3-4):187–202, 2005.

J.E. Overland, M. Wang, and S. Salo. The recent Arctic warm period. *Tellus A*, 60(4): 589–597, 2008.

J. Overpeck, K. Hughen, D. Hardy, R. Bradley, R. Case, M. Douglas, B. Finney, K. Gajewski, G. Jacoby, A. Jennings, et al. Arctic environmental change of the last four centuries. *Science*, 278(5341):1251, 1997.

P.O.G. Persson, C.W. Fairall, E.L. Andreas, P.S. Guest, and D.K. Perovich. Measurements near the Atmospheric Surface Flux Group tower at SHEBA: Near-surface conditions and surface energy budget. *Journal of Geophysical Research-Oceans*, 107(C10), 2002. doi: 10.1029/2000JC000705.

CD Peters-Lidard, E. Blackburn, X. Liang, and EF Wood. The effect of soil thermal conductivity parameterization on surface energy fluxes and temperatures. *Journal of the Atmospheric Sciences*, 55(7):1209–1224, 1998.

AJ Pitman. The evolution of, and revolution in, land surface schemes designed for climate models. *International Journal of Climatology*, 23(5):479–510, 2003.

J. Pulliainen and M. Hallikainen. Retrieval of regional snow water equivalent from spaceborne passive microwave observations. *Remote sensing of environment*, 75(1):76–85, 2001.

V. Rachold, A. Alabyan, H.W. Hubberten, VN Korotaev, and AA Zaitsev. Sediment transport to the Laptev Sea–hydrology and geochemistry of the Lena River. *Polar Research*, 15(2):183–196, 2007.

W.G. Rees. Infrared emissivity of Arctic winter snow. *International Journal of Remote Sensing*, 14(16):3069–3073, 1993.

I.G. Rigor, R.L. Colony, and S. Martin. Variations in surface air temperature observations in the Arctic, 1979–97. *Journal of Climate*, 13(5):896–914, 2000.

A. Rinke, P. Kuhry, and K. Dethloff. Importance of a soil organic layer for Arctic climate: A sensitivity study with an Arctic RCM. *Geophysical Research Letters*, 35(13):L13709, 2008.

D.A. Rothrock, Y. Yu, and G.A. Maykut. Thinning of the Arctic sea-ice cover. *Geophysical Research Letters*, 26(23):3469–3472, 1999.

W.R. Rouse, C.J. Oswald, J. Binyamin, C. Spence, W.M. Schertzer, P.D. Blanken, N. Bussières, and C.R. Duguay. The role of northern lakes in a regional energy balance. *Journal of Hydrometeorology*, 6(3):291–305, 2005.

T. Sachs, C. Wille, J. Boike, and L. Kutzbach. Environmental controls on ecosystem-scale CH 4 emission from polygonal tundra in the Lena River Delta, Siberia. *Journal of Geophysical Research. G. Biogeosciences*, 113:G00A03, 2008. doi: 10.1029/2007JG000505.

J.W. Salisbury and D.M. D'Aria. Emissivity of terrestrial materials in the 8-14 microns atmospheric window. *Remote Sensing of Environment*, 42(2):83–106, 1992.

M. Scheritz, R. Dietrich, S. Scheller, W. Schneider, and J. Boike. Digital Elevation Model of Polygonal Patterned Ground on Samoylov Island, Siberia, Using Small-Format Aerial Photography. *Proceedings, NICOP (Vol. II)*, pages 1589–1594, 2008.

HP Schmid. Source areas for scalars and scalar fluxes. *Boundary-Layer Meteorology*, 67(3): 293–318, 1994.

P. Schotanus, FTM Nieuwstadt, and HAR Bruin. Temperature measurement with a sonic anemometer and its application to heat and moisture fluxes. *Boundary-Layer Meteorology*, 26(1):81–93, 1983.

E.A.G. Schuur, J. Bockheim, J.G. Canadell, E. Euskirchen, C.B. Field, S.V. Goryachkin, S. Hagemann, P. Kuhry, P.M. Lafleur, H. Lee, et al. Vulnerability of permafrost carbon to climate change: Implications for the global carbon cycle. *BioScience*, 58(8):701–714, 2008.

G. Schwamborn, V. Rachold, and M.N. Grigoriev. Late Quaternary sedimentation history of the Lena Delta. *Quaternary international*, 89(1):119–134, 2002.

P. Sellers, F. Hall, K.J. Ranson, H. Margolis, B. Kelly, D. Baldocchi, G. den Hartog, J. Cihlar, M.G. Ryan, B. Goodison, et al. The Boreal Ecosystem–Atmosphere Study (BOREAS): an overview and early results from the 1994 field year. *Bulletin of the American Meteorological Society*, 76(9):1549–1577, 1995.

P.J. Sellers, F.G. Hall, G. Asrar, D.E. Strebel, and R.E. Murphy. An overview of the first international satellite land surface climatology project(ISLSCP) field experiment(FIFE). *Journal of geophysical research*, 97(D17):18345–18371, 1992.

M.C. Serreze, J.E. Walsh, F.S. Chapin, T. Osterkamp, M. Dyurgerov, V. Romanovsky, W.C. Oechel, J. Morison, T. Zhang, and R.G. Barry. Observational evidence of recent change in the northern high-latitude environment. *Climatic Change*, 46(1):159–207, 2000.

M.C. Serreze, J.A. Maslanik, T.A. Scambos, F. Fetterer, J. Stroeve, K. Knowles, C. Fowler, S. Drobot, R.G. Barry, and T.M. Haran. A record minimum arctic sea ice extent and area in 2002. *Geophys. Res. Lett*, 30(3):1110, 2003. doi: 10.1029/2002GL016406.

M.D. Shupe and J.M. Intrieri. Cloud radiative forcing of the Arctic surface: The influence of cloud properties, surface albedo, and solar zenith angle. *Journal of Climate*, 17(3), 2004.

C.C. Slama, C. Theurer, and S.W. Henriksen. *Manual of photogrammetry*. American Society of Photogrammetry Falls Church, Virginia, 1980.

W.C. Snyder and Z. Wan. BRDF models to predict spectral reflectance and emissivity in the thermal infrared. *IEEE Transactions on Geoscience and remote Sensing*, 36(1): 214–225, 1998.

W.C. Snyder, Z. Wan, Y. Zhang, and Y.Z. Feng. Thermal infrared(3-14 micron) bidirectional reflectance measurements of sands and soils. *Remote Sensing of Environment*, 60 (1):101–109, 1997.

W.C. Snyder, Z. Wan, Y. Zhang, and Y.Z. Feng. Classification-based emissivity for land surface temperature measurement from space. *International Journal of Remote Sensing*, 19(14):2753–2774, 1998.

M. Stendel and JH Christensen. Impact of global warming on permafrost conditions in a coupled GCM. *Geophysical Research Letters*, 29(13):1632, 2002.

D.A. Stow, A. Hope, D. McGuire, D. Verbyla, J. Gamon, F. Huemmrich, S. Houston, C. Racine, M. Sturm, K. Tape, et al. Remote sensing of vegetation and land-cover change in Arctic Tundra Ecosystems. *Remote Sensing of Environment*, 89(3):281–308, 2004.

J.C. Stroeve, M.C. Serreze, F. Fetterer, T. Arbetter, W. Meier, J. Maslanik, and K. Knowles. Tracking the Arctic's shrinking ice cover: another extreme minimum in 2004. *Geophys. Res. Lett*, 32(4):L04501, 2005. doi: 10.1029/2007GL029703.

M. Sturm, J. Holmgren, M. König, and K. Morris. The thermal conductivity of seasonal snow. *Journal of Glaciology*, 43(143):26–41, 1997.

K. Tape, M. Sturm, and C. Racine. The evidence for shrub expansion in Northern Alaska and the Pan-Arctic. *Global Change Biology*, 12(4):686–702, 2006.

D.W.J. Thompson and J.M. Wallace. The Arctic Oscillation signature in the wintertime geopotential height and temperature fields. *Geophysical Research Letters*, 25(9):1297–1300, 1998.

J. Turner, J.E. Overland, and J.E. Walsh. An Arctic and Antarctic perspective on recent climate change. *International Journal of Climatology*, 27(3):277–293, 2007.

UNEP/GRID-Arendal. Projected changes in the arctic climate, 2090. unep/grid-arendal maps and graphics library. (http://maps.grida.no/go/graphic/projected-changes-in-the-arctic-climate-2090), 2005a.

UNEP/GRID-Arendal. Permafrost distribution in the arctic. unep/grid-arendal maps and graphics library. (http://maps.grida.no/go/graphic/permafrost-distribution-in-the-arctic), 2005b.

USGS. The lena river delta. (http://eros.usgs.gov/imagegallery/), 2000.

S. Vavrus. The impact of cloud feedbacks on Arctic climate under greenhouse forcing. *Journal of Climate*, 17(3), 2004.

AA Velichko and VP Nechayev. Late Pleistocene Permafrost in European USSR. *Late Quaternary Environments of the Soviet Union*, pages 79–86, 1984.

R.C. Vining and B.L. Blad. Estimation of sensible heat flux from remotely sensed canopy temperatures. *Journal of Geophysical Research*, 97(D17):18951–18954, 1992.

P. Viterbo, A. Beljaars, J.F. Mahfouf, and J. Teixeira. The representation of soil moisture freezing and its impact on the stable boundary layer. *Quarterly Journal of the Royal Meteorological Society*, 125(559):2401–2426, 1999.

D. Wagner, A. Gattinger, A. Embacher, E.V.A.M. Pfeiffer, M. Schloter, and A. Lipski. Methanogenic activity and biomass in Holocene permafrost deposits of the Lena Delta, Siberian Arctic and its implication for the global methane budget. *Global Change Biology*, 13(5):1089–1099, 2007.

KM Walter, SA Zimov, JP Chanton, D. Verbyla, and FS Chapin. Methane bubbling from Siberian thaw lakes as a positive feedback to climate warming. *Nature*, 443(7107):71–75, 2006.

KM Walter, ME Edwards, G. Grosse, SA Zimov, and FS Chapin III. Thermokarst lakes as a source of atmospheric CH4 during the last deglaciation. *science*, 318(5850):633, 2007.

Z. Wan. New refinements and validation of the MODIS land-surface temperature/emissivity products. *Remote Sensing of Environment*, 112(1):59–74, 2008.

Z. Wan. MODIS land surface temperature products users' guide. (http://www.icess.ucsb.edu/modis/LstUsrGuide/usrguide.html), 2009.

Z. Wan and J. Dozier. A generalized split-window algorithm for retrieving land-surfacetemperature from space. *IEEE Transactions on geoscience and remote sensing*, 34(4):892–905, 1996.

Z. Wan and T. Zhang. MODIS UCSB Emissivity Library. (http://www.icess.ucsb.edu/modis/EMIS/html/em.html), 1999.

S. Westermann, J. Lüers, M., K. Piel, and J. Boike. The annual surface energy budget of a high-arctic permafrost site on Svalbard, Norway. *The Cryosphere*, 3:245–263, 2009.

K. Wilson, A. Goldstein, E. Falge, M. Aubinet, D. Baldocchi, P. Berbigier, C. Bernhofer, R. Ceulemans, H. Dolman, C. Field, et al. Energy balance closure at FLUXNET sites. *Agricultural and Forest Meteorology*, 113(1-4):223–243, 2002.

D. Yang, D.L. Kane, L.D. Hinzman, X. Zhang, T. Zhang, and H. Ye. Siberian Lena River hydrologic regime and recent change. *J. Geophys. Res*, 107(D23):4, 2002.

Ė.D. Yershov and P.J. Williams. *General geocryology*. Cambridge Univ Pr, 2004.

T. Zhang. Influence of the seasonal snow cover on the ground thermal regime: An overview. *Reviews of Geophysics*, 43(4), 2005.

T. Zhang, RG Barry, K. Knowles, JA Heginbottom, and J. Brown. Statistics and characteristics of permafrost and ground-ice distribution in the Northern Hemisphere. *Polar Geography*, 31(1):47–68, 2008.

X. Zhang, J.E. Walsh, J. Zhang, U.S. Bhatt, and M. Ikeda. Climatology and interannual variability of Arctic cyclone activity: 1948–2002. *Journal of Climate*, 17:12, 2004.

S.A. Zimov, E.A.G. Schuur, and F.S. Chapin III. Permafrost and the global carbon budget. *Science(Washington)*, 312(5780):1612–1613, 2006.

Eidesstattliche Erklärung
zur Anfertigung der Dissertation

Ich erkläre hiermit an Eides Statt, dass ich die vorliegende Arbeit mit dem Titel „The Spatial and Temporal Variability of the Energy Balance at an Arctic Polygonal Tundra Site“ selbständig sowie ohne unzulässige Hilfe Dritter und ohne Benutzung anderer als der angegebenen Hilfsmittel angefertigt habe. Die aus anderen Quellen direkt oder indirekt übernommenen Daten und Konzepte sind unter Angabe der Quelle gekennzeichnet.

Potsdam, 20.06.2010 _____

Moritz Langer